Naval Surface Warfare Center
Carderock Division
West Bethesda, MD 20817-5700

NSWCCD-61-TR-2023/19 **September 2023**

Platform Integrity Department

Technical Report

Temperature-Dependent Material Property Databases for Marine Steels – Part 5: HY-80

by

Jennifer K. Semple

Daniel H. Bechetti

Wei Zhang (The Ohio State University)

Justin E. Norkett

Charles R. Fisher

Naval Surface Warfare Center
Carderock Division
West Bethesda, MD 20817-5700

NSWCCD-61-TR-2023/19 **September 2023**

Platform Integrity Department
Technical Report

Temperature-Dependent Material Property Databases for Marine Steels – Part 5: HY-80

by
Jennifer K. Semple
Daniel H. Bechetti
Wei Zhang (The Ohio State University)
Justin E. Norkett
Charles R. Fisher

REPORT DOCUMENTATION PAGE

Form Approved
OMB No. 0704-0188

1. REPORT DATE *(DD-MM-YYYY)*	2. REPORT TYPE	3. DATES COVERED *(From - To)*
21-09-2023	Technical Report	JAN 2018 – JUN 2019

4. TITLE AND SUBTITLE

Temperature-Dependent Material Property Databases for Marine Steels – Part 5: HY-80

5a. CONTRACT NUMBER N/A

5b. GRANT NUMBER N/A

5c. PROGRAM ELEMENT NUMBER N/A

6. AUTHOR(S)
Jennifer K. Semple
Daniel H. Bechetti
Wei Zhang
Justin E. Norkett
Charles R. Fisher

5d. PROJECT NUMBER N/A

5e. TASK NUMBER

5f. WORK UNIT NUMBER

7. PERFORMING ORGANIZATION NAME(S) AND ADDRESS(ES) AND ADDRESS(ES)

Naval Surface Warfare Center,
Carderock Division, Code 611
9500 MacArthur Boulevard
West Bethesda, MD 20817-5700

Ohio State University, Department of
Materials Science & Engineering
Welding Engineering Program
1248 Arthur Adams Dr
Columbus, OH 43221

8. PERFORMING ORGANIZATION REPORT NUMBER

NSWCCD-61-TR-2023/19

9. SPONSORING / MONITORING AGENCY NAME(S) AND ADDRESS(ES)

William Mullins
Program Manager, 332
Office of Naval Research
Arlington, VA 22217

Lightweight Innovations for Tomorrow (LIFT)
Detroit, MI 48216

10. SPONSOR/MONITOR'S ACRONYM(S) ONR

11. SPONSOR/MONITOR'S REPORT NUMBER(S) N/A

12. DISTRIBUTION / AVAILABILITY STATEMENT

DISTRIBUTION A. Approved for public release: distribution unlimited.

13. SUPPLEMENTARY NOTES

14. ABSTRACT:

The Lightweight Innovations for Tomorrow (LIFT) project entitled, Robust Distortion Control Methods and Implementation for Construction of Lightweight Metallic Structures – ICME Extension to Advanced Alloys, sought to address distortion issues with thin-plate steel fabrication of U.S. Navy ships. Integrated Computational Materials Engineering (ICME)-based tools and techniques were identified as the best path forward for distortion mitigation through computational simulation of the welding process. ICME tools require temperature-dependent material properties to achieve accurate computational results for distortion and residual stress. Properties of note include specific heat, thermal conductivity, coefficient of thermal expansion (CTE), elastic modulus, yield strength, and flow stress of alloys from room temperature to near melting. In addition, the temperatures associated with on-heating and on-cooling phase transformations and their variation with heating rate, cooling rate, and peak temperature are also important for the prediction of stress and distortion evolution.

The integrated project team (IPT) made generating pedigreed, temperature-dependent material property databases of Navy-relevant steels a key task within the LIFT project. The testing plan included some of the most common marine steels used in the construction of U.S. Naval vessels; namely, DH36, HSLA-65, HSLA-80, HSLA-100, HY-80, and HY-100. Material testing for each of the six steel grades was performed jointly by the Welding Engineering Program within the Department of Materials Science and Engineering at the Ohio State University (OSU) and the Welding, Processing, and Nondestructive Evaluation Branch at the Naval Surface Warfare Center, Carderock Division (NSWCCD). The temperature-dependent material property data was then sent to ESI for adaptation for use in their welding-based, finite-element analysis (FEA) software colloquially known as SYSWELD. This report is part of a seven-part series detailing the pedigreed steel data. The first six reports will report and discuss the material properties for each of the individual steel grades, whereas the final report will compare and contrast the measured steel properties across all six steels, while also comparing them to the available literature data. This report will focus specifically on the data associated with HY-80 steel.

15. SUBJECT TERMS

ICME, CWM, SYSWELD, Computational Simulation, Steel, Welding, Material Database, HY-80

16. SECURITY CLASSIFICATION OF:			17. LIMITATION OF ABSTRACT	18. NUMBER OF PAGES	19a. RESPONSIBLE PERSON
a. REPORT	b. ABSTRACT	c. THIS PAGE			19b. TELEPHONE NUMBER
UNCLASSIFIED	UNCLASSIFIED	UNCLASSIFIED		98	Charles Fisher (301) 221-2259

CONTENTS

Page

FIGURES

Page

TABLES

Page

ADMINISTRATIVE INFORMATION

The work described in this report was performed by the Welding, Processing, and Nondestructive Evaluation Branch (Code 611) of the Platform Integrity Department at the Naval Surface Warfare Center, Carderock Division (NSWCCD) and by the Department of Materials Science and Engineering at the Ohio State University. The work was funded in FY18-19 by the Office of Naval Research (ONR), in support of the Lightweight Innovations for Tomorrow (LIFT) Institute's program entitled *Robust Distortion Control Methods and Implementation for Construction of Lightweight Metallic Structures – ICME Extension to Advanced Alloys*.

ACKNOWLEDGEMENTS

The authors would like to thank the other members of the LIFT Joining-R4-3 integrated project team, including other engineers at the Naval Surface Warfare Center, Carderock Division (Matthew Sinfield, Maria Posada, and Johnnie DeLoach), Huntington Ingalls Industries – Ingalls Shipbuilding (T.D. Huang, Randy Johnson, Yu-Ping Yang, Steve Scholler, Charlotte Merritt, Shannon Dolese, Anthony Copeland, Andrew Nicholson, Lance Carnahan, Stacey Merritt, Win Delancey, Dianna Genton, and John Walks), the University of Michigan (Pingsha Dong, Jack Hu, Theodor Freiheit), the Ohio State University (Colleen Hilla and Chris Cathis), ESI (Yogendra [San] Gooroochan and Mark Doroudian), and LIFT (Melvin Hawke, Alan Taub, and Hadrian Rori), for their technical assistance in the completion of this work.

This page intentionally left blank

EXECUTIVE SUMMARY

The Lightweight Innovations for Tomorrow (LIFT) project entitled, Robust Distortion Control Methods and Implementation for Construction of Lightweight Metallic Structures – ICME Extension to Advanced Alloys, sought to address distortion issues with thin-plate steel fabrication of U.S. Navy ships. Integrated Computational Materials Engineering (ICME)-based tools and techniques were identified as the best path forward for distortion mitigation through computational simulation of the welding process. ICME tools require temperature-dependent material properties to achieve accurate computational results for distortion and residual stress. Properties of note include specific heat, thermal conductivity, coefficient of thermal expansion (CTE), elastic modulus, yield strength, and flow stress of alloys from room temperature to near melting. In addition, the temperatures associated with on-heating and on-cooling phase transformations and their variation with heating rate, cooling rate, and peak temperature are also important for the prediction of stress and distortion evolution.

The integrated project team (IPT) made generating pedigreed, temperature-dependent material property databases of Navy-relevant steels a key task within the LIFT project. The testing plan included some of the most common marine steels used in the construction of U.S. Naval vessels; namely, DH36, HSLA-65, HSLA-80, HSLA-100, HY-80, and HY-100. Material testing for each of the six steel grades was performed jointly by the Welding Engineering Program within the Department of Materials Science and Engineering at the Ohio State University (OSU) and the Welding, Processing, and Nondestructive Evaluation Branch at the Naval Surface Warfare Center, Carderock Division (NSWCCD). The temperature-dependent material property data was then sent to ESI for adaptation for use in their welding-based, finite-element analysis (FEA) software colloquially known as SYSWELD.

This report is part of a seven-part series detailing the pedigreed steel data. The first six reports will report and discuss the material properties for each of the individual steel grades, whereas the final report will compare and contrast the measured steel properties across all six steels, while also comparing them to the available literature data. This report will focus specifically on the data associated with HY-80 steel.

BACKGROUND

The Lightweight Innovations for Tomorrow (LIFT) project entitled, *Robust Distortion Control Methods and Implementation for Construction of Lightweight Metallic Structures – ICME Extension to Advanced Alloys*, is a collaborative research project to address the complex fabrication problems that arise from the use of thin, high-strength steel panels for ship construction. The importance of lightweighting in the commercial and military shipbuilding sectors has gained attention in recent decades as a way to increase the performance capabilities of products while also reducing total ownership costs. Over the past decade, the production ratio of thin plate (10 mm [3/8-in.] or less) to thicker plate structures for steel construction at Huntington Ingalls Industries – Ingalls Shipbuilding has risen to over 80% in the Coast Guard's National Security Cutter (NSC) program. Modern naval vessel designs also make greater use of complex panels with inserts and cutouts, further increasing the fabrication complexity to achieve weight savings while meeting structural requirements.

European shipbuilding research suggests that 30% of hull fabrication costs can be attributed to re-work and fit-up issues due to distortion [1]. Integrated Computational Materials Engineering (ICME)-

based prediction tools can be used to quantify distortions associated with the fabrication process of complex stiffened panels or other lightweight structures. These tools, once validated on selected product forms, could be used to establish recommended fitting, fixturing, welding, and assembly sequencing for optimized distortion control in thin-plate steel construction.

These ICME tools require detailed, reliable databases of temperature-dependent material properties in order to increase the accuracy of calculated distortion and residual stresses in welded metallic structures. Of highest importance to the fidelity of such models are the thermo-physical and thermo-mechanical properties of the material(s) being joined. The properties of note include specific heat, thermal conductivity, coefficient of thermal expansion (CTE), elastic modulus, yield strength, and flow stress of the alloy, from room temperature to near melting. The temperatures associated with on-heating and on-cooling phase transformations and their variation with heating rate, cooling rate, and peak temperature are also important for the prediction of stress and distortion evolution.

While some of these data exist for the most common Navy steels, these are generally not suitable for use in high-fidelity welding-focused computational models for several reasons. First, the methods of data generation are inconsistent because the testing was completed over many decades by separate researchers and programs. Also, significant gaps exist in the data, especially at temperatures above approximately 400 °C (~750 °F). Additionally, some available data are restricted against public distribution. Finally, the data are, in general, subject to reliability issues because of changes in material fabrication and testing practices that have occurred in the decades since the data were generated. To combat this lack of comprehensive and consistent data, the integrated project team (IPT) made generating pedigreed, temperature-dependent material property databases of Navy-relevant steels a key task within the LIFT project. A major portion of the tasking involved analysis of heat-affected zone (HAZ) microstructures, as this region of rapidly changing microstructure results in significant changes in resultant mechanical properties. These varied HAZ region microstructures of Navy-relevant also do not have well-established mechanical property data, especially as a function of temperature and heating or cooling rate.

The testing plan included some of the most common marine steels used in the construction of U.S. Naval vessels; namely DH36, HSLA-65, HSLA-80, HSLA-100, HY-80, and HY-100. HSLA is short for “high-strength low-alloy,” whereas HY stands for “high yield.” The number designation behind HSLA and HY is the minimum yield strength of the plate material in units of ksi. Current (as of this writing) specifications for these alloys can be found in references [2] [3] [4]. Material testing for each of the six steel grades was performed jointly by the Welding Engineering Program within the Department of Materials Science and Engineering at the Ohio State University (OSU) and the Welding, Processing, and Nondestructive Evaluation Branch at the Naval Surface Warfare Center, Carderock Division (NSWCCD). The temperature-dependent material property data was then sent to ESI for adaptation for use in their welding-based, finite-element analysis (FEA) software colloquially known as *SYSWELD*.

This report is part of a seven-part series based on the pedigreed steel data. The first six reports will focus on establishing the material properties for each of the individual steel grades, whereas the final report will compare and contrast the measured steel properties across all six steels, while also comparing them to the available literature data. Follow-on reports detailing use of these temperature-dependent material databases within the LIFT-funded program are also expected. While this report focuses on HY-80 data, the citation for the previous report on DH36 is [5], HSLA-65 is [6], HSLA-80 is [7], and HSLA-100 is [8].

APPROACH

Material Testing Program

The material property assessment program was developed through inputs from welding engineers at NSWCCD, researchers at OSU, and modeling experts at ESI. The program focused on generating the types of data required to develop Navy-relevant material databases for use by ESI's commercial software, *SYSWELD*. The raw data could also be adapted for use by other FEA tools, such as MSC's *Simufact Welding* or the welding module for *Abaqus*. Specific data included thermo-physical and mechanical properties of the alloys of interest, from room temperature up to near-melting. Density, heat capacity, thermal conductivity, and coefficient of thermal expansion (CTE) were identified as the most important thermo-physical properties. Mechanical properties of interest included the elastic modulus, yield strength, and flow stress.

Material from a single HY-80 steel plate procured to NAVSEA Technical Publication T9074-BD-GIB-010/0300 (Tech Pub 300) [4] was analyzed for this project. The nominally 4.76 mm (3/16-in.) thick plate was acquired by Huntington Ingalls Industries – Ingalls Shipbuilding (HII – Ingalls). The room temperature yield strength and elongation requirements for the alloy are 552-758 MPa (80-110 ksi) and 14% in 50 mm (2-in.), respectively [4]. There are no ultimate tensile strength requirements for HY-80 plate procured to Tech Pub 300 [4]. The plate conformance certification sheet for the material investigated in this study is given in **Appendix A**. A portion of this plate was cut into 610 mm by 305 mm (24-in. by 12-in.) pieces and shipped to both NSWCCD and OSU for determination of temperature-dependent material properties.

Chemical Composition

The chemical composition of the base material was measured at OSU using optical emission spectroscopy on a SPECTROMAXx arc spark system. Additional chemical composition testing was performed at NSWCCD using glow discharge atomic emission spectroscopy (GD-AES) with a LECO GDS900 glow discharge spectrometer. All composition testing was performed in accordance with ASTM E415 [9]. Carbon and sulfur content was measured at NSWCCD with a LECO CS844 combustion analyzer according to ASTM E1019 [10].

Heat Affected Zone Phase Transformation Analysis

Phase transformations of HY-80 as a function of austenitization temperature and cooling rate were assessed via dilatometry. Continuous cooling transformation (CCT) diagrams were developed for four regions of the heat affected zone (HAZ) that are subject to microstructural transformation during welding: the intercritical region (ICHAZ); the low-temperature, fine-grained region (FGHAZ1); the high-temperature, fine-grained region (FGHAZ2); and the coarse-grained region (CGHAZ).

Heating and cooling rates for these regions in HY-80 were assumed to be the similar those for DH36 weldments [5]. As part of the DH36 effort [5], the heating and cooling rates were defined by combining typical heat inputs used in the fabrication of DH36 weldments, from 0.4 to 2.6 kJ/mm (10 to 65 kJ/in) as suggested by Ingalls engineers, with numerical simulation of the heat flow using the *SmartWeld* program from Sandia National Laboratories [11]. From these calculations, it was determined that peak temperatures (T_{peak}) between 785 and 1350 °C (1445 and 2462 °F), in combination with cooling rates between 1 and 200 °C/s (1.8 and 360 °F/s), would provide information covering a sufficiently broad range of phase transformation behavior relevant to both slowly-cooled welds (*e.g.*, high heat input welds on thin plate) and rapidly-cooled welds (*e.g.*, low heat input welds on thick plate). These CCT diagrams

informed the temperature-dependent mechanical property testing program as well, specifically for heating and cooling rates, peak temperatures, and various testing temperatures.

In addition to the on-cooling CCT diagram development, this portion of the testing program also involved a detailed assessment of the on-heating austenite transformation as a function of heating rate. Just as on-cooling transformation temperatures vary with cooling rate, so does on-heating austenitization temperature (A_{c1} and A_{c3}). Heating rates between 10 and 2000 °C/s (18 and 3632 °F/s) were used to study these variations. **Table 1** shows the full test matrix utilized for HAZ CCT diagram development.

Table 1. Test Matrix for HAZ CCT Diagram Development

Test Type	Region	Peak Temperature, °C (°F)	Heating Rate, °C/s (°F/s)	Soak Time, s	Cooling Rate, °C/s (°F/s)
A_{c1}/A_{c3} Determination	N/A	1200 (2192)	10 (18) 100 (180) 200 (360) 500 (900) 1000 (1800) 2000 (3600)	N/A	N/A
CCT Diagram Development	ICHAZ	785 (1445)	200 (360)	2	1 (1.8) 5 (9) 10 (18) 25 (45) 100 (180) 200 (360)
	FGHAZ1	1000 (1832)			
	FGHAZ2	1150 (2102)			
	CGHAZ	1350 (2462)			

Execution of this test matrix was performed at NSWCCD by employing a Gleeble 3500 thermo-mechanical simulation apparatus to apply the prescribed heating and cooling rates. The Gleeble operates on the principles of resistive heating, conductive cooling through water-cooled fixturing, and rapid (50 kHz) control system feedback to apply precise thermal cycles even at rapid heating and cooling rates that cannot be easily achieved by other apparatus. The Gleeble 3500 system, in combination with the apparatus's standard 'Pocket Jaw' setup, used full contact copper grips and 70 mm (2.76-in.) long specimens with 3 mm (0.118-in.) diameters. A linear variable differential transformer (LVDT)-type contact extensometer was used to measure diametric dilation of the specimens during heating and cooling. All dilatometry specimens were extracted perpendicular to the rolling direction of the plate, and all dilatometry tests were performed in an argon atmosphere. The typical experimental setup for the dilatometry testing is shown in **Figure 1.**

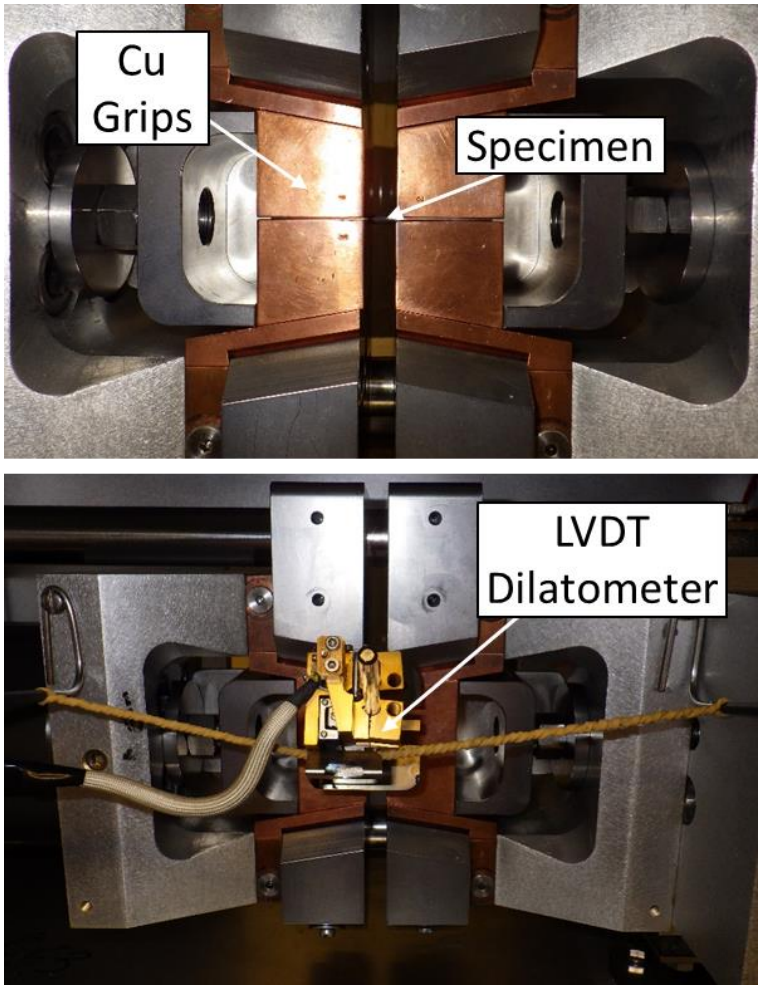

Figure 1. Photographs of the Gleeble-based dilatometry experimental set-up.

Thermo-Physical Property Analysis

Specimens were sent to the Thermophysical Properties Research Laboratory, Inc. (TPRL) in West Lafayette, IN for analysis of thermal diffusivity (α) and specific heat (C_p). Thermal diffusivity was measured using the laser flash method according to ASTM E1461 [11]. Specific heat was measured using differential scanning calorimetry (DSC) methods according to ASTM E1269 [12]. Coefficient of thermal expansion (CTE) was measured from the on-heating Gleeble dilatometry data in two regimes: 200 to 750 °C (392 to 1382 °F) for the base material microstructure, and 875 to 1100 °C (1607 to 2012 °F) for austenite. No attempt was made to determine CTE during the on-heating transformation between 750 °C (1382 °F) and 875 °C (1607 °F). CTE calculations were performed by linear fitting of dilation data within each temperature range in conjunction with **Equation 1**. The material was assumed to be isotropic.

$$\alpha_T = \left(\frac{\Delta d}{d_0}\right)\left(\frac{1}{\Delta T}\right) \qquad \textbf{(1)}$$

where $\alpha_T \equiv$ Linear coefficient of thermal expansion [°C^{-1}]
$\Delta d \equiv$ Change in specimen diameter over the chosen temperature range [cm]
$d_0 \equiv$ Initial specimen diameter [cm]
$\Delta T \equiv$ Temperature range [°C]

The temperature-dependent density (ρ) was calculated using a theoretical cubic volume element under the assumption of isotropic thermal expansion:

$$\rho(T) = \frac{\rho_0 V_0}{V(T)} \quad \textbf{(2)}$$

where $\rho(T)$ ≡ Density at temperature T [g/cm^3]
ρ_0 ≡ Room temperature density provided by TPRL [g/cm^3]
V_0 ≡ Room temperature volume of the theoretical cubic element [cm^3]
$V(T)$ ≡ Volume of the theoretical cubic element at temperature T [cm^3]

V_0 was calculated assuming a side length equal to the room temperature width of the dilatometry specimens. This value was chosen because, as shown in **Figure 1**, it corresponds to the starting gauge length for the dilatometer used to measure thermal expansion. A theoretical cubic volume element was chosen instead of the actual specimen dimensions to subvert potential complications with measuring dimensions that were not directly measured by the dilatometer (*e.g.*, the effect of thermal gradients on measurement of the specimen's longitudinal expansion). V_T was simply calculated by:

$$V(T) = [w(T)]^3 \quad \textbf{(3)}$$

where $w(T)$ ≡ Dilatometer-measured specimen width at temperature T [cm]

This method allowed calculation of the density through the austenite transformation. Finally, thermal conductivity (λ) as a function of temperature was then calculated by using **Equation 4**:

$$\lambda = \rho \cdot c_p \cdot \alpha \quad \textbf{(4)}$$

where λ ≡ Thermal conductivity [W/cm-°C]
c_p ≡ Specific heat capacity [J/g-°C]
ρ_0 ≡ Room temperature density [g/cm^3]
α ≡ Thermal diffusivity [cm^2/s]

Thermo-Mechanical Property Analysis

Tensile specimens were machined from the HY-80 plates according to the dimensions shown in **Figure 2a**. All specimens were extracted with their length perpendicular to the rolling direction of the plate. Elastic modulus, yield strength, and flow stress were identified as the required mechanical properties from room temperature up to near-melting. On-heating tension testing of the HY-80 base material at temperatures between 22 and 1100 °C (72 and 2012 °F) was performed by the Ohio State University using their Gleeble 3800. Specimens were spray painted with an yttrium oxide (Y_2O_3) solvent-based paint to provide contrast between the black and white speckle pattern sprayed onto the face of specimens, as shown in **Figure 2b**. Tensile testing was carried out using digital image correlation in lieu of a contact extensometer. Room temperature testing was performed in accordance with ASTM A370 [13], and elevated temperature testing was performed in accordance with ASTM E21 [14].

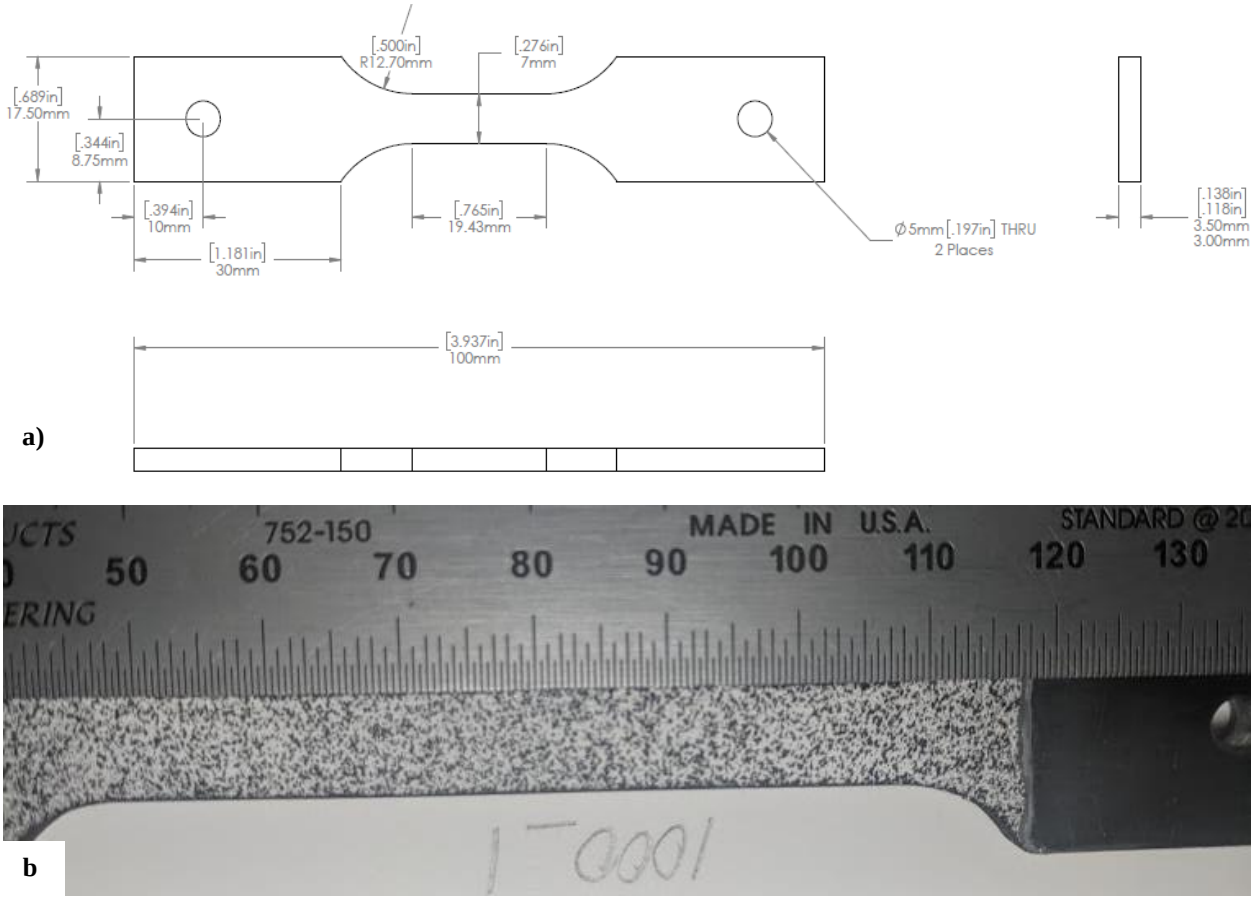

Figure 2. Tensile specimens for Gleeble-based mechanical testing of HY-80 steel: **a)** dimensions for single-reduced gauge section, **b)** sample speckle pattern for DIC testing (dimensions in mm).

On-cooling mechanical properties were measured using the Gleeble 3500 at NSWCCD. Prior to mechanical testing, the specimens were thermally cycled to generate different initial microstructures based on the results of the CCT diagram development described above. For HY-80, microstructural analysis indicated that substantially different microstructures formed when the material was cooled at 1, 10, 25, and 100 °C/s (1.8, 18, 45, and 180 °F/s). Because of programmatic time constraints, only a peak temperature of 1350 °C (2462 °F) was applied to the tensile specimens. All specimens were heated in an argon atmosphere, and forced air was used to meet cooling rates of 10 °C/s (18 °F/s) and above. All specimens were cooled to room temperature, and thereafter a contact longitudinal extensometer was affixed. The specimens were then reheated to the test temperature at a rate of 10 °C/s (18 °F/s) and soaked for 10 sec. before being pulled to failure in crosshead control mode at strain rates targeting those prescribed in ASTM E21 [14]. The crosshead displacement rate used was 0.30 mm/min (0.012 in/min). It is acknowledged that this is not the most representative method of testing for welding-related applications because the stresses that develop during welding do so rapidly and while the material is cooling and undergoing phase transformations. However, given the programmatic intent of establishing the mechanical behavior of specific microstructures and the need to avoid exposing the strain measurement device to exceedingly high temperatures, the method of cooling to room temperature and tension testing after reheating was determined to be an acceptable compromise. In cases where the induced

microstructure was stronger than the base material, a second reduced gauge section was machined in the specimen prior to testing to ensure specimen fracture in the region of interest. This revised specimen geometry is shown in **Figure 3**.

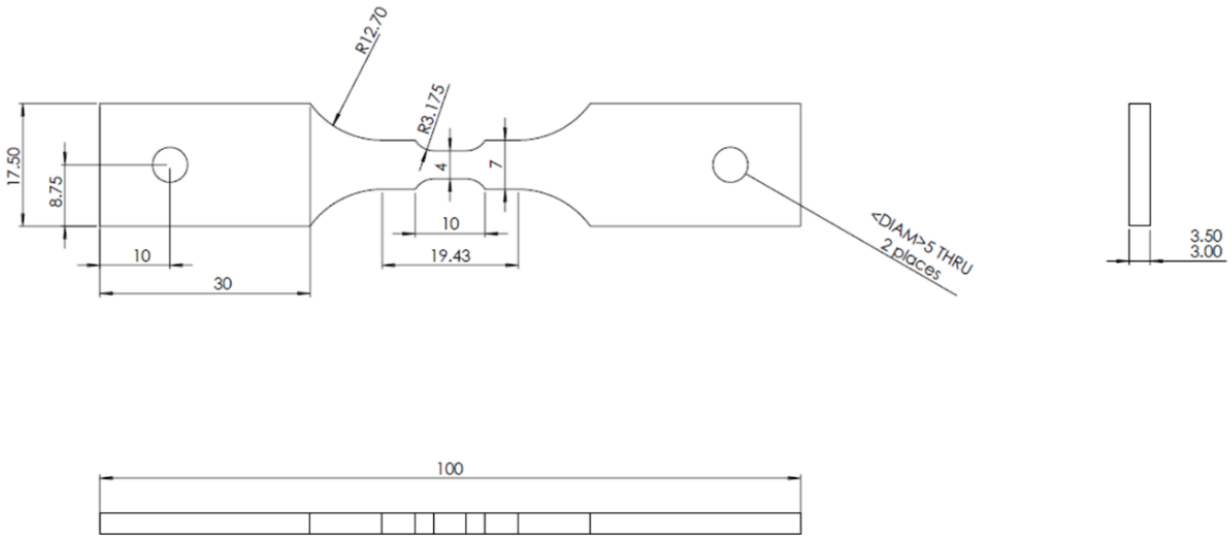

Figure 3. Specimen dimensions for Gleeble-based mechanical testing of HY-80 steel for a double-reduced gauge section (dimensions in mm).

Thermal cycling and subsequent tensile testing were performed using the Gleeble apparatus's "Pocket Jaw" setup with minimal contact stainless steel grips used to fixture the specimen. These grips were selected to minimize the longitudinal thermal gradient in the gauge length of the specimens during testing. Graphite foil was inserted between the specimen and the grips to further minimize the thermal gradient. Strain in the specimens was measured using a contact longitudinal extensometer, and the initial gauge length for the tests varied between 8 and 10 mm (0.31 and 0.39 in.). Elevated temperature tension tests were performed in an argon atmosphere. Preliminary testing as part of the DH36 test program [5] indicated that for this setup, the temperature variation across the initial gauge length was 10 to 30 °C (18 to 54 °F). The typical experimental setup for the dilatometry testing is shown in **Figure 4**.

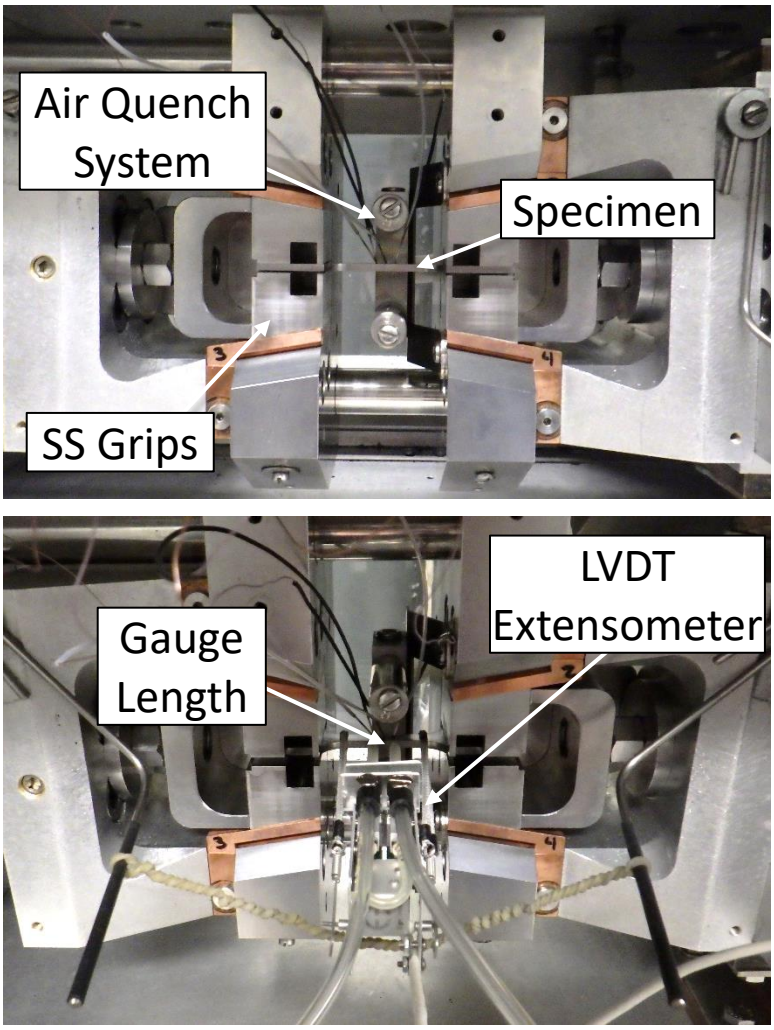

Figure 4. Photographs of the Gleeble-based mechanical testing experimental set-up.

Fabrication of Welded Specimens

Additionally, two sets of HY-80 plates were welded together at Ingalls and sent to OSU to investigate the plate, weld, and heat-affected zone (HAZ) microstructures. The first set of plates were welded using submerged arc welding (SAW) in a two-sided butt joint configuration, as shown in **Figure 5a**. The second set of plates were welded using flux cored arc welding (FCAW) in a two-sided tee-joint configuration, as shown in **Figure 5b**. Welding parameters for both scenarios are given in **Table 2**. These weldments enabled correlation of the microstructures generated through thermal simulations for the CCT curves with those produced from arc welding. Each weldment is representative of two primary types of joints used at Ingalls for structural welds: seaming butt joints and fillet joint stiffener welds. These joint types were also the focus of larger fabrication efforts described in other tasks within the greater LIFT project as described in [15].

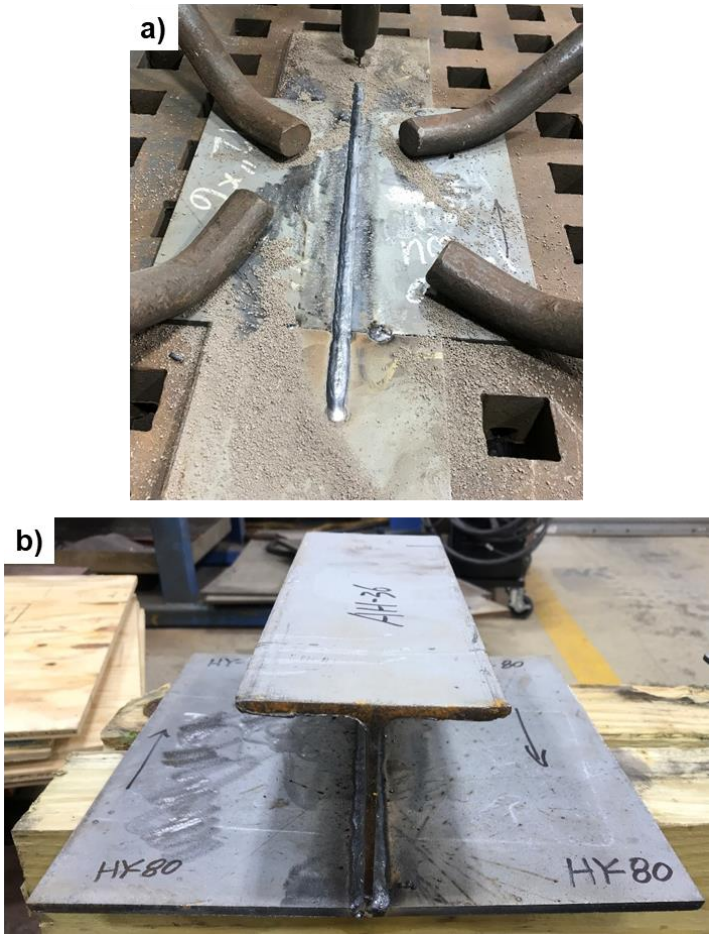

Figure 5. Representative **a)** butt and **b)** tee joint weldments of HY-80 material investigated for plate, weld, and HAZ microstructures.

Table 2. Nominal Welding Parameters used to Fabricate HY-80 Butt and Tee Joints

	Butt Joint	**Tee Joint**
Welding Process	Submerged arc (SAW)	Flux cored arc (FCAW)
Current (A)	325 / 350 (1st / 2nd Pass)	160-165
Voltage (V)	30	27
Travel Speed (mm/s [in/min])	10.6 (25)	6.35 (15)
Heat Input (kJ/mm [kJ/in])	0.92 / 0.99 (23.4 / 25.2)	0.68-0.70 (17.3-17.8)
Consumable Designation	MIL-E-23765/2E: MIL-100S-1	AWS A5.20 E71T-1
Filler Wire Diameter (mm [in])	3.175 (0.125)	1.32 (0.052)
Interpass Temperature, Max. (°C [°F])	38 (100)	60 (140)

Microstructural Analysis

To quantify and characterize the HY-80 weldment microstructures, a cross-section of each of the weldments represented in **Figure 5** was analyzed. Each specimen was metallographically prepared to a final polish of 0.05 μm using standard techniques and etched by immersion in 4% Picral (4 g picric acid

dissolved in 100 mL ethanol) for approximately 10 seconds followed by immersion in 2% Nital (2 mL nitric acid in 98 mL of ethanol) for 5 seconds. Metallographic preparation was followed by light optical microscopy (LOM) and scanning electron microscopy (SEM) analysis. Vickers microhardness values measured using a load of 200 g (7.05 oz.) were taken from the fusion zone through the HAZ to the base material for both weldments.

Thermally cycled specimens from the HAZ CCT diagram development were metallographically prepared using the same procedure. Identification and phase fraction measurement of the microstructural constituents in each specimen were evaluated using image analysis through LOM and SEM. Vickers microhardness testing was also used to determine the hardness of the constituent(s) in each CCT specimen. This analysis facilitated proper CCT analysis, provided phase fraction input for the HY-80 material property database, and helped determine which thermal cycles were the most appropriate for application in the mechanical testing portion of the program described above.

RESULTS AND DISCUSSION

Chemical Composition

Table 3 shows the averaged results of three base material chemistry measurements for the HY-80 plate, plus manufacturer's plate certification values (shown in **Appendix A**), the NAVSEA Tech Pub 300 HY-80 specifications [4], and results from two studies conducted at the Applied Research Laboratory of the United States Steel company as part of U.S. Navy projects over 50 years ago. This data is labeled "U.S. Steel" in subsequent charts and testing was conducted on a plate of either 12.7 mm (0.5 in.) [16] or 25.4 mm (1.0 in.) [17] nominal thickness. As expected, the measured chemical composition values generally agreed with the manufacturer's plate certification and were well within the NAVSEA specifications. The carbon equivalency number (CEN) was calculated according to Yurioka *et al.* [18]. The individual measurements made by OSU and NSWCCD to obtain the average composition values are located in **Appendix A**.

Solidus and Liquidus Analysis

Solidus and liquidus temperatures were not experimentally measured for HY-80 base material as part of this project. A report by Honeywell as part of a previous U.S. Navy project gave a stated melting point of 1520 °C (2768 °F) for HY-80 material [19].

Base Metal Microstructure

The microstructure of the HY-80 base metal is shown in the light optical micrograph in **Figure 6**. The microstructure is tempered martensite. The manufacturer subjected base material to a hardening heat treatment at a nominal temperature of 904 °C (1660 °F) for 14 minutes followed by quenching, then tempered it at 693 °C (1280 °F) for 26 minutes followed by air cooling to room temperature. The average Vickers microhardness of the base metal was 242 ± 7.7 HV_{200}.

Observing the HY-80 base metal in both the longitudinal and transverse planes revealed no evidence of anisotropy. The heat treat effectively erased evidence of prior austenite grains and no attempt to quantify prior austenite grain size was made. LOM techniques revealed fine precipitates but no attempt was made to positively identify them. The relatively high carbon content of this alloy and the typical behavior of tempered steel both suggest that these are carbides.

Table 3. Chemical Composition of HY-80 Material (wt.%)

Type	C	Mn	P	S	Si	Ni	Cr	Mo
Measured Avg. (OSU)	0.10	0.26	0.003	0.0005	0.33	2.56	1.19	0.23
Measured Avg. (NSWCCD)	0.1374	0.25	0.004	0.00375	0.32	2.07	1.20	0.20
Plate Certificate	0.12	0.27	0.005	0.002	0.33	2.05	1.17	0.22
Tech Pub 300 [4]	0.08-0.18	0.10 – 0.40	<0.015	<0.004	0.15-0.38	2.00-3.25	1.00-1.80	0.20-0.60
U.S. Steel [16]	0.14	0.27	0.007	0.009	0.26	2.96	1.58	0.50
U.S. Steel [17]	0.14	0.30	0.010	0.018	0.20	2.94	1.62	0.48

Type	Cu	V	Ti	Al	Nb	Sb	As	Sn	Fe	CEN [18]
Measured Avg. (OSU)	0.14	0.004	0.002	0.023	0.001	---	---	0.011	Bal	0.427
Measured Avg. (NSWCCD)	0.14	0.0002	<0.001	0.025	<0.003	---	---	<0.005	Bal	0.488
Plate Certificate	0.14	0.002	0.001	0.019	0.001	0.0010	0.0030	0.010	Bal	0.457
Tech Pub 300 [4]	<0.25	<0.03	<0.02	---	---	<0.025	<0.025	<0.03	Bal	---
U.S. Steel [16]	---	0.038	---	0.072	---	---	---	---	Bal	0.670
U.S. Steel [17]	---	---	---	0.038	---	---	---	---	Bal	0.668

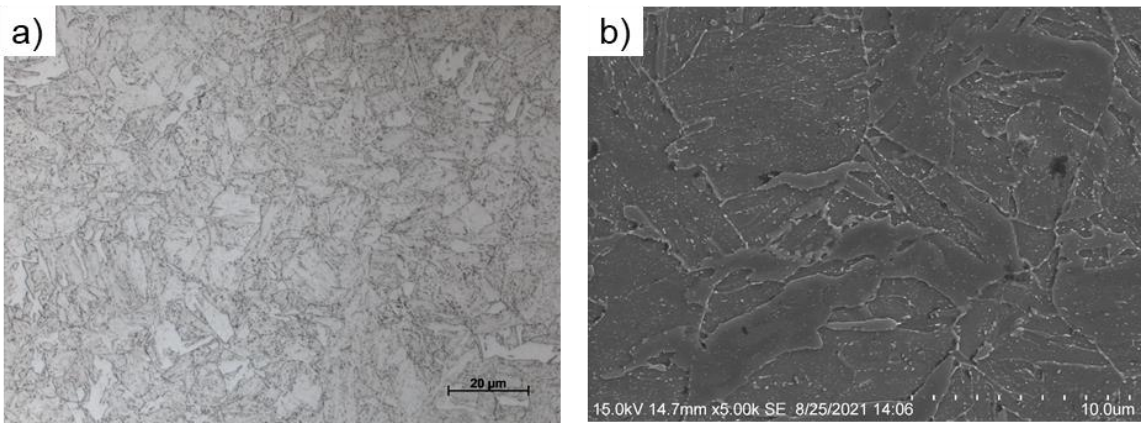

Figure 6. Representative micrograph of HY-80 steel plate base metal microstructure etched with 4% Picral and 2% Nital, shown at **a)** 1000x magnification using LOM and **b)** 5000x magnification using SEM.

Heat Affected Zone Phase Transformation Analysis

Dilation Curve Analysis Method

Figure 7 shows a representative on-heating portion of a Gleeble-produced dilatometry curve generated by NSWCCD. The black curve (left axis) represents the change in sample diameter (*i.e.*, dilation) with temperature, with non-linearity in the black dilation curve corresponding to a phase transformation. Instances at which non-linearity occurs can be highlighted by graphing the derivative of the dilation curve with respect to temperature, shown by the red curve (right axis). Simple linear extrapolations of the black dilation curve are shown by the blue lines as a secondary method for pinpointing the temperatures at which nonlinearity occurs. In this case, the transformation of interest is that of the HY-80 base metal microstructure to austenite.

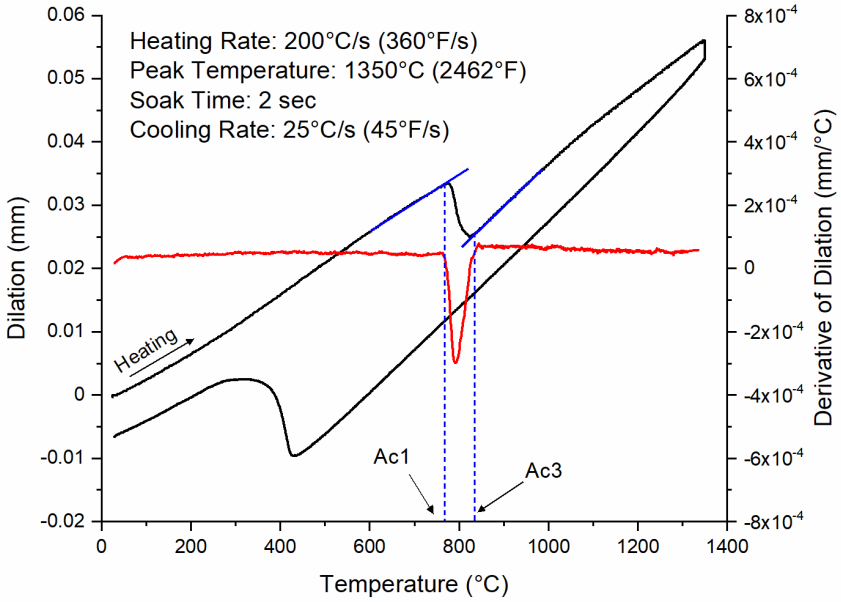

Figure 7. Representative on-heating dilatometry curve for HY-80 steel, showing the linear extrapolation and derivative curve methods for evaluating the ferrite to austenite reaction. Black curve, left axis: dilation data. Red curve, right axis: derivative of dilation data. Blue lines: extrapolation lines for determining transformation start (A_{c1}) and finish (A_{c3}) temperatures.

Two methods for extracting start and finish temperatures for phase transformations from Gleeble dilatometry data are commonly used. The first method involves superimposing a straight line of matching slope along the low temperature portion of the dilation curve and extrapolating it past the transformation. The point at which the experimental data begins to deviate from the straight line is then taken as the transformation start temperature. The same technique is then used to find the transformation finish temperature, with the straight line being extrapolated from the high-temperature portion of the curve after the transformation. The second method involves calculating and plotting the derivative of the dilation curve. Then the points at which the derivative begins to deviate from a constant value are taken as the transformation start and finish temperatures. Both methods for determining phase transformation temperatures are inherently somewhat subjective, and both also have advantages and disadvantages. The linear extrapolation method is faster and easier to interpret but is difficult to use when multiple transformations occur. The derivative method is more quantitative and can more easily distinguish

multiple transformations but can be difficult to interpret when the dilation data is noisy. For this work, the linear extrapolation method was chosen as the primary method of data analysis, and the derivative method was used as a complementary technique for distinguishing concurrent phase transformations. Both methods are shown in **Figure 7**, where the derivative curve is displayed in red and the linear extrapolations are displayed in blue.

Austenite Transformation Temperature Measurement

Figure 8 presents the variation in austenite transformation behavior as a function of heating rate for HY-80 base material. As shown, the austenite transformation start temperature (A_{c1}) is relatively insensitive to heating rate. This is expected, as the tempered state of the base material leaves very little inhomogeneity and requires minimal mass diffusion to take place prior to austenite transformation. The sample heated at 500 °C/s (932 °F/s) appears to be an outlier in this dataset as a result of experimental error, likely showing artificially high values because of misalignment of the dilatometer with the thermocouple. Recall that the sample is heated via resistive heating, which produces a thermal gradient across the length of the specimen. In this case, the dilatometer corresponded to an adjacent, cooler region of the dilatometry sample. The heating here lagged slightly, such that by the time A_{c1} was reached at the dilatometer, the thermocouples were reporting a higher temperature in the hotter adjacent region. This may be an explanation for why the present data is consistently higher than those reported by US Steel [17]. The austenite transformation finish temperature (A_{c3}) shows a significant decrease as the heating rate increased to 200 °C/s (360 °F/s) before a relatively stable value at higher heating rates, though again the 500 °C/s (932 °F/s) data point appears to be an outlier.

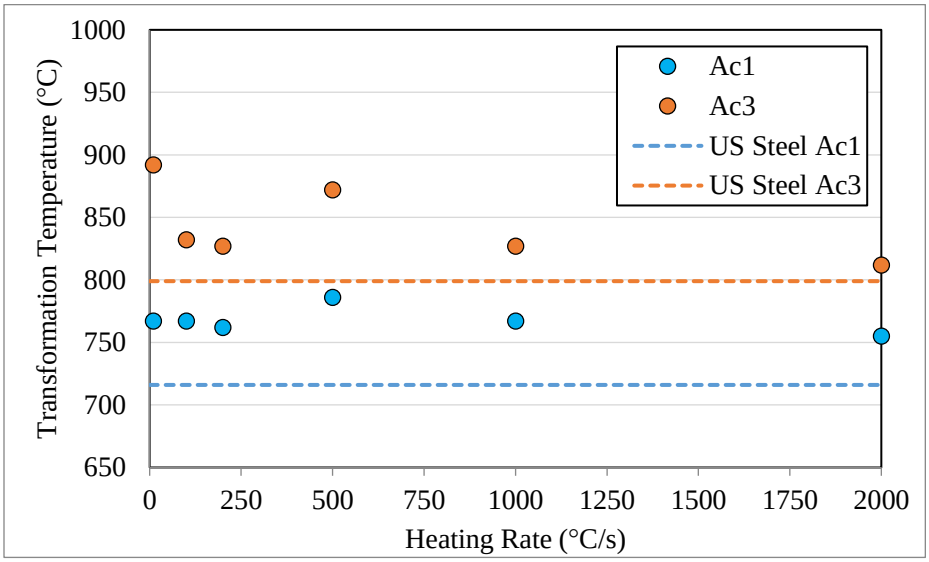

Figure 8. Variation in austenite transformation start and finish temperatures with heating rate for HY-80 material. Horizontal dashed lines represent the US Steel reported transformation temperatures [17].

On-heating transformation data are important for the refinement of welding simulation results because different regions of a weldment and its HAZ are subject to significantly different heating rates during the welding process. The on-heating transformation behavior must be incorporated in order to accurately predict which areas around the weld will transform to austenite and will therefore be subject to re-transformation (and associated changes in mechanical properties and residual stresses) during cooling. The raw data points for **Figure 8** can be found in **Table 10** within **Appendix B**.

Continuous Cooling Transformation Diagrams

CCT diagrams assembled from dilatometry of HY-80 thermally cycled to peak temperatures representative of the four selected HAZ regions are given in **Figures 9-12**. The austenite transformation temperatures described above resulted in selection of an ICHAZ simulation temperature of 785 °C (1445 °F) for HY-80, which was 5 °C (9 °F) lower than that used for HSLA-100 [8], 40 °C (72 °F) lower than that used for HSLA-65 [6] and HSLA-80 [7], and 90 °C (162 °F) lower than the temperature used for DH36 [5]. The A_{c1} and A_{c3} temperatures labeled on the CCT diagrams are averages calculated from the individual A_{c1} and A_{c3} values for all of the CCT specimens. The black curves are the actual specimen cooling curves. The target cooling rates for all specimens except those cooled at 100 and 200 °C/s (180 and 360 °F/s) were maintained through the on-cooling phase transformations. The latent heat released during low temperature transformation slowed the cooling rates of both the 100 °C/s (180 °F/s) and the 200 °C/s (360 °F/s) tests for all peak temperatures. As a result, the target cooling rate was maintained until the start of the transformation, but was slowed as the transformations occurred for 100 and 200 °C/s (180 and 360 °F/s) tests. The raw data for these figures are given in **Tables11-14** of **Appendix B**, and the individual dilation curves are given in **Figures 38-61** of **Appendix B**.

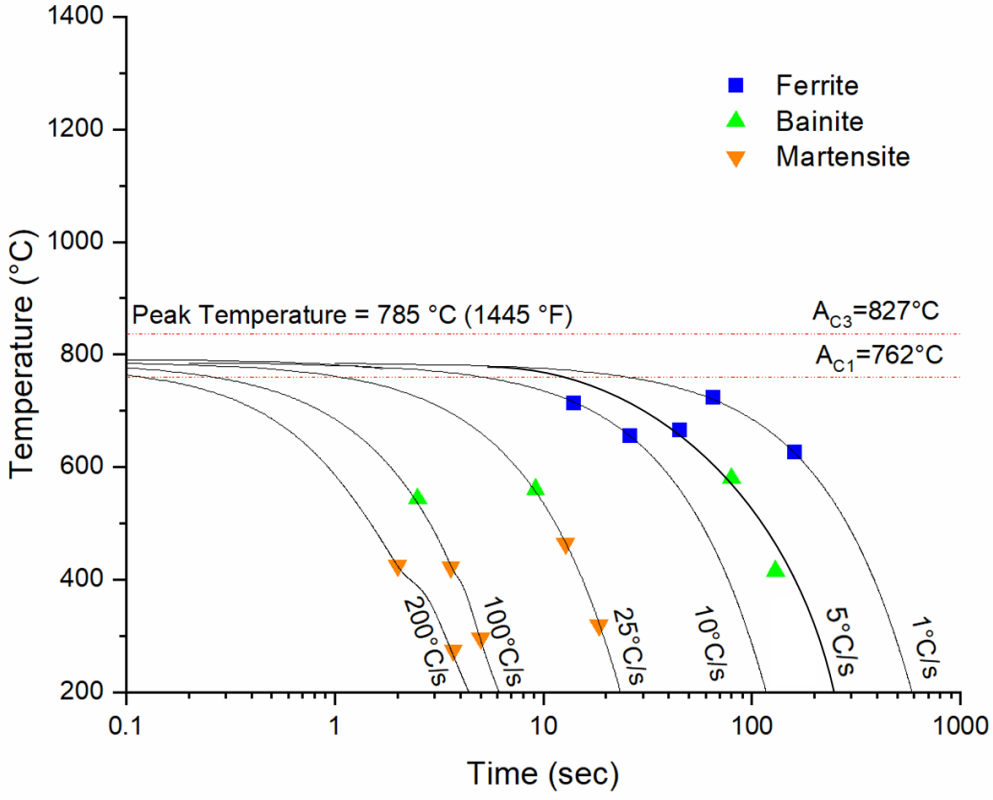

Figure 9. CCT diagram for HY-80 heated to peak temperature of 785 °C (1445 °F).

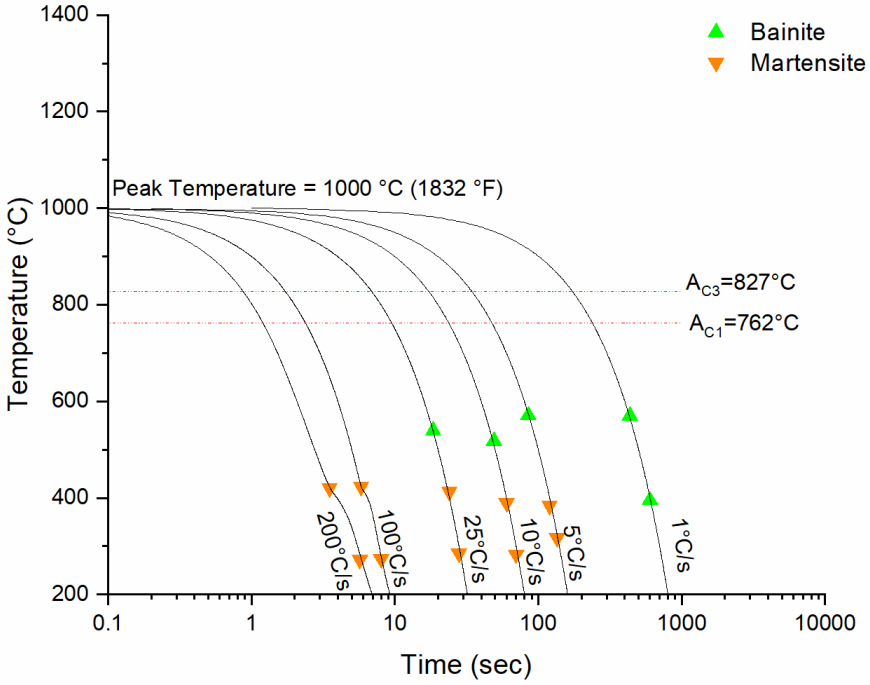

Figure 10. CCT diagram for HY-80 heated to peak temperature of 1000 °C (1832 °F).

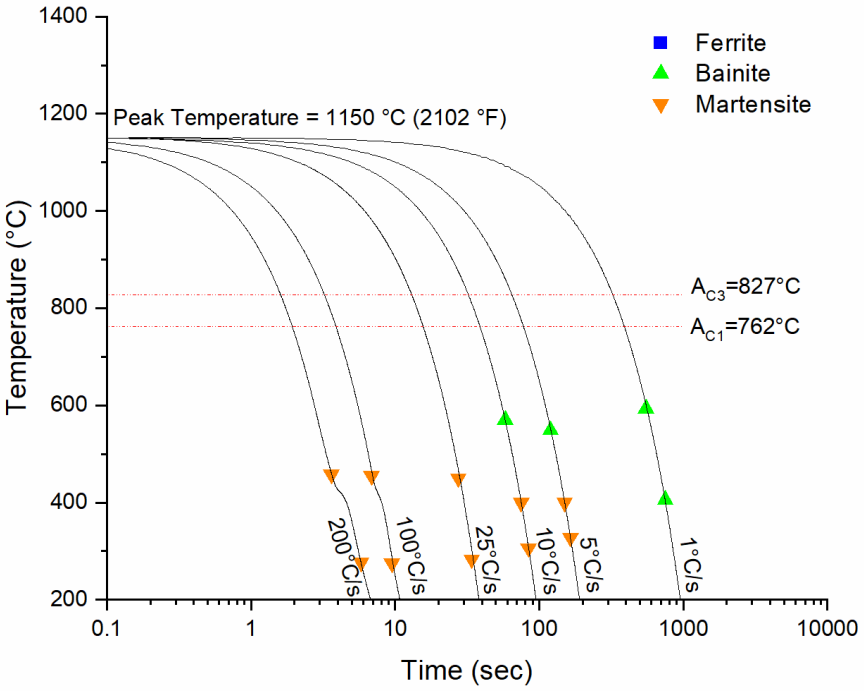

Figure 11. CCT diagram for HY-80 heated to peak temperature of 1150 °C (2102 °F).

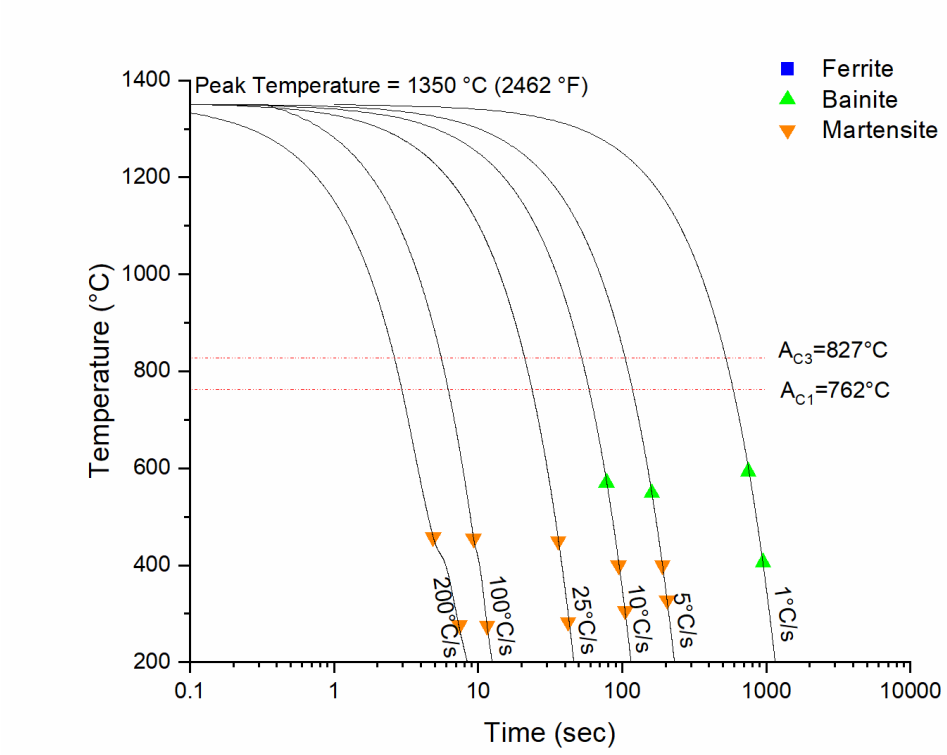

Figure 12. CCT diagram for HY-80 heated to peak temperature of 1350 °C (2462 °F).

The colored symbols in **Figures 9-12** correspond to the start and finish temperatures for the various on-cooling phase transformations. Simulated HAZ regions were subject to up to three regimes of on-cooling transformation start temperatures across the cooling rate range assessed in this work as shown in **Figure 13-Figure 15**. The first transformation occurred at high temperatures and was associated with ferrite formation, which was only observed for slow cooling conditions (1-10 °C/s [1.8-18 °F/s]) in the ICHAZ sample, as illustrated below in **Figure 13**. In general, ferrite start transformation temperature is expected to be suppressed as cooling rate increased, due to the diffusion-based nature of ferritic transformations. No pattern was discernible for the three cases in which ferrite appeared, likely due to the sensitivity of ICHAZ transformations to experimental conditions (*e.g.*, peak temperature, cooling rate) that are difficult to perfectly reproduce for a partial transformation. This is exacerbated by the extremely narrow region of the physical sample that reaches peak temperature. In this case, even a minor offset between the dilatometer and the thermocouples attached to the specimen may have a drastic effect on recorded phase transformations. At the time of testing a laser dilatometer was not available to mitigate such measurement errors.

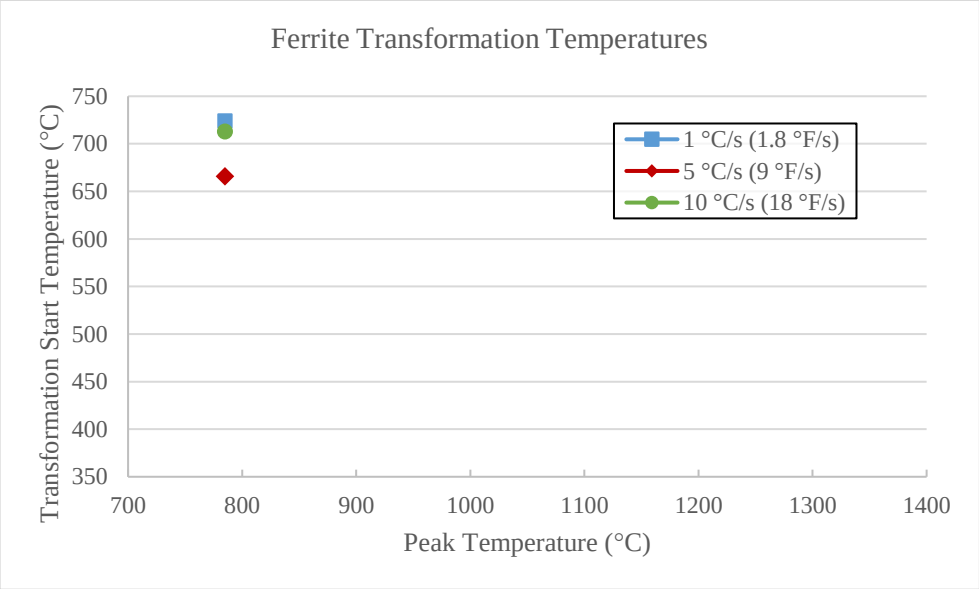

Figure 13. Variation of start temperature for the ferrite transformation shown in **Figures 9-12**.

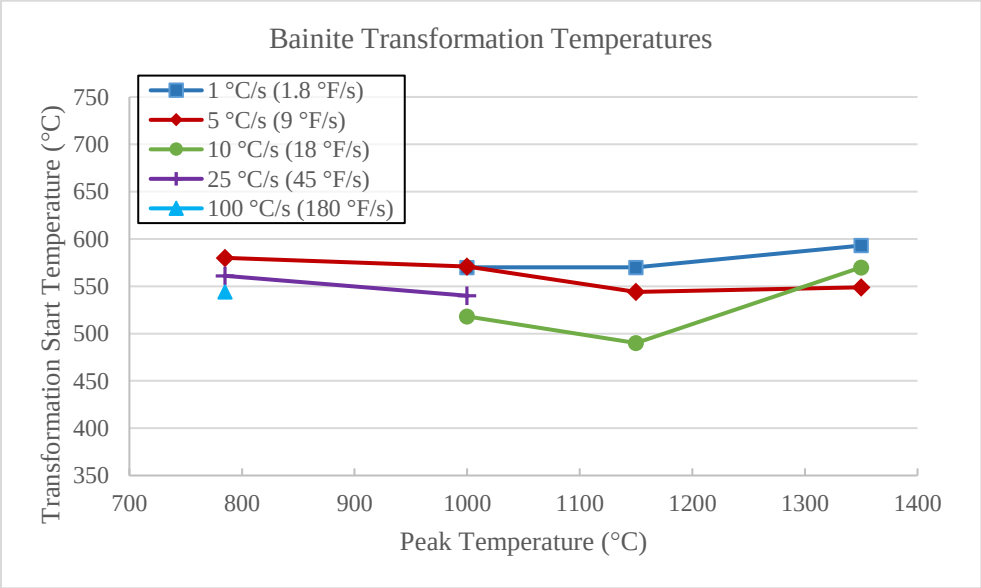

Figure 14. Variation of start temperature for the bainite transformation shown in **Figures 9-12**.

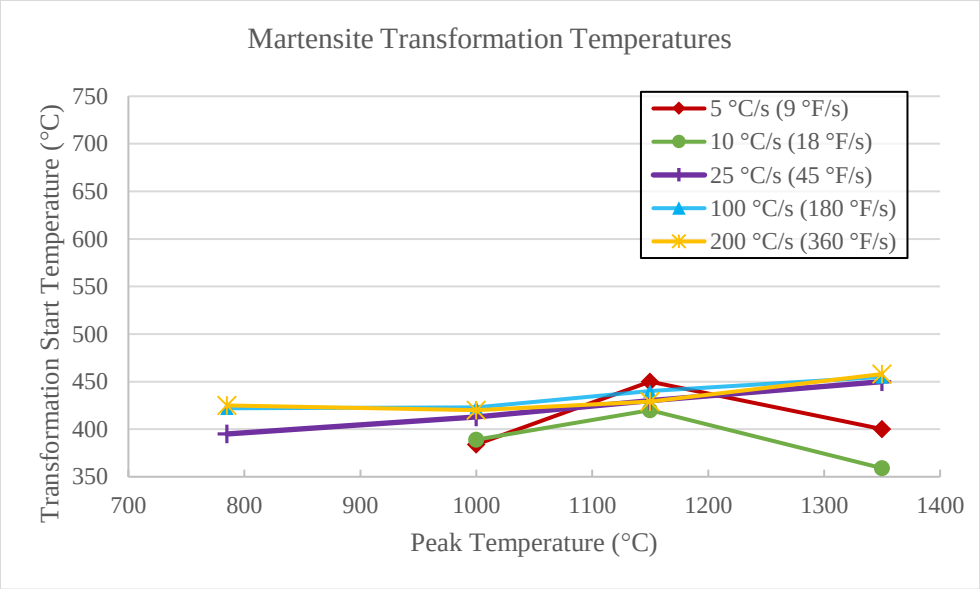

Figure 15. Variation of start temperature for the martensite transformation shown in **Figures 9-12**.

Bainite was present in all samples cooled at rates below 25 °C/s (45 °F/s), with additional presence in samples heated to ICHAZ and FGHAZ1 peak temperatures, as shown in **Figure 14**. Martensite was a more common transformation product in the low temperature regime and was detected in samples cooled at rates of 25 °C/s (45 °F/s) and higher for the ICHAZ specimens and in samples cooled at rates of 5 °C/s (9 °F/s) and higher for FGHAZ and CGHAZ specimens. There is no clear relationship shown in this data between M_s and either peak temperature or cooling rate. These transformation start temperatures are illustrated in **Figure 15**. This is not unexpected, as thermal cycles represented here affect microsegregation in a complex manner, and this local chemistry drives the martensitic transformation.

In order to establish the identities of the on-cooling phase transformations, LOM was performed on all dilatometry specimens and select specimens were analyzed via SEM. Micrographs collected from the dilatometry specimens are given in **Figures 62-67** of **Appendix C.** Additionally, the measured microhardness for each specimen is shown in **Figure 16** (raw data is found in **Table 15** of **Appendix D**). For this discussion, the following definitions for the morphology of microstructural constituents are adopted based on references [21] [22] [23] [24] [25]. The typical definitions for crystal structure and composition of the constituents are also assumed.

Primary ferrite (F_P) – Carbide-free grain boundary or intragranular allotriomorphic or idiomorphic ferrite

Acicular ferrite (AF) – Fine, interlocking structure formed by impingement of multiple Widmanstätten plates growing from intragranular inclusions

Martensite-austenite constituent (M/A) – Structure represented by a combination of martensite and residual austenite

Bainite (B) – General term for fine aggregates of ferrite laths or plates and cementite particles

Lath martensite (M_L) – Martensite laths with highly dislocated substructure which are grouped into larger packets

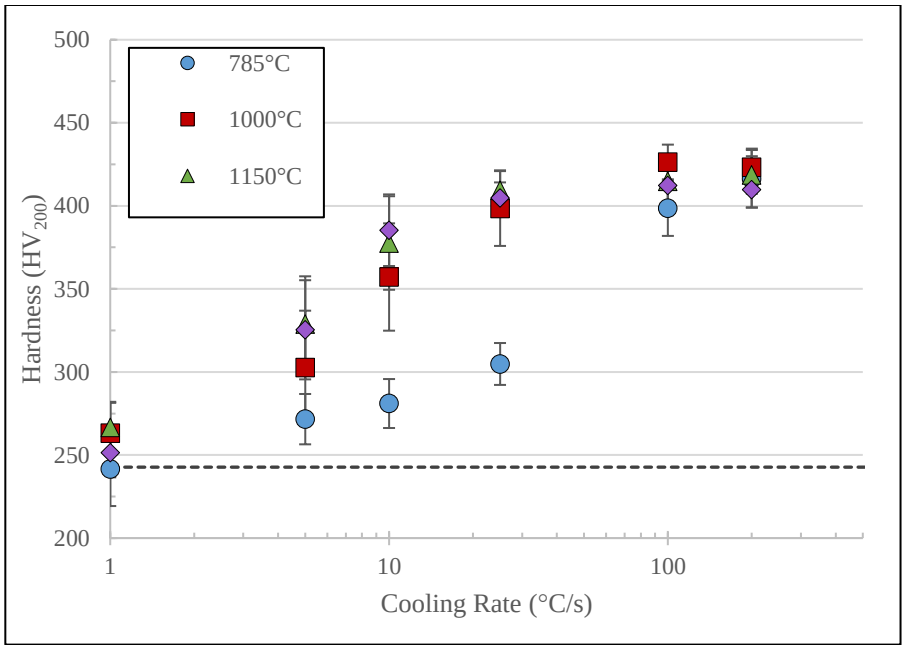

Figure 16. Measured Vickers microhardness for HY-80 dilatometry specimens as a function of peak temperature and cooling rate. Error bars are one standard deviation. Values are the average of 11-52 indents. Data is tabulated in **Table 15** of **Appendix D**.

Representative micrographs of all CCT specimens heated to 785 °C (1445 °F) are shown in **Figure 62** of **Appendix C**, with measured phase fractions reported in **Table 4**. This temperature falls between A_{c1} and A_{c3} (762 and 827 °C [1404 and 1521 °F], respectively) and was chosen in order to achieve partial transformation to austenite prior to cooling. While the progression of phases shown in micrographs is readily explainable, the transformation temperatures captured by dilatometry were unreliable due to experimental error associated with contact dilatometry use on specimens with extremely steep thermal gradients. A best effort has been made identify transformation temperatures but it is recommended that additional investigations are undertaken for applications that are particularly sensitive to ICHAZ transformations.

Table 4. Measured Phase Fraction of HY-80 CCT Specimens Thermally Cycled to a Peak Temperature of 785 °C (1445 °F)

Cooling Rate		**Peak Temperature = 785 °C (1445 °F)**		
°C/s	**°F/s**	**F + M/A**	**B**	**M**
1	1.8	1	0	0
5	9	1	0	0
10	18	0.73	0.27	0
25	45	0.64	0.36	0
100	180	0	0.20	0.80
200	360	0	0	1

Though dilation curves showed little transformation above A_{c1}, very little of the original base metal microstructure was preserved in the slowly cooled intercritical samples. In samples cooled between 1-25 °C/s (1.8-45 °F/s), optical microscopy revealed the presence of classic, light-etched quasipolygonal

ferrite grains in addition to a tan-etching constituent. This constituent was present in the largest quantities in the sample cooled at 1 °C/s (1.8 °F/s) and appeared in bands that ran parallel to the top and bottom of the plate, with a particularly extensive region along the plate centerline. As cooling rates increased, this banding pattern disappeared, with the tan-etched constituent instead distributed randomly throughout the sample in increasingly small islands. This phase was not associated with an obvious volumetric change: the dilation curve for the sample cooled at 1 °C/s (1.8 °F/s) shows only the high-temperature transformation associated with ferrite, beginning at 724 °C (1081 °F) and completing at 626 °C (1159 °F).

While the tan-etched constituent bears a close resemblance to M/A constituent under optical microscopy, it comprised almost 30% of the microstructure in the sample cooled at 1 °C/s (1.8 °F/s), which is higher than volumetric fractions typically reported in literature [26]. M/A constituent is comprised of untempered martensite embedded within carbon-rich retained austenite. The compositional range associated with HY-80 does not support austenite near room temperature, with the exception of regions that have become preferentially enriched in austenite-stabilizing solute. Etching response shown in optical micrographs suggest that these regions are either M/A constituent or tempered martensite from the base material that had been further tempered by the CCT thermal cycle. SEM (**Figures 63** and **64**) revealed the particularly thick centerline band to be composed primarily of a fine, needle-like phase interspersed with non-aligned carbides. A thinner band located at approximately one quarter of the specimen thickness was a mix of this needle-like phase, relatively featureless ferrite grains, and ferrite grains with a loosely aligned secondary phase.

An effort was made to measure the microhardness local to banded regions in order to inform this evaluation. In the absence of nanoindentation equipment, microhardness indents were made with a relatively low load on etched surfaces in order to target distinct regions. It is noted that performing microhardness testing on an etched surface is not consistent with best practices, and that these values should be considered relative to one another rather than as absolute data. Two indents in the thick band of tan-etched constituent measured 462 and 433 HV_{100} under a 100 g load. A third indent with slightly less than half its area extending into the ferrite region was measured to be 270 HV_{100}. Two indents entirely within the ferritic region measured 177 and 206 HV_{100}, respectively. The smaller bands or islands of tan-etched constituent did not have adequate surface area to target with indents made by a 100 g load, thus additional test were made using a 50 gram load. With this load, two indents in the thick band of tan-etched constituent measured 512 and 410 HV_{50}. Thin bands measured 270 and 279 HV_{50}, while indents that overlapped both the thin bands and ferritic regions were measured to be 232 and 243 HV_{50}. Ferrite was measured to be 191 HV_{50}. In comparison, the base material was 241 HV_{50} with a standard deviation of 9.4.

Base metal measurements made with a load of 50 grams were almost 20 HV lower than those measured using a load of 300 grams, suggesting that the targeted measurements slightly underestimate microhardness values. From this, it becomes clear that the tan-etched constituent is associated with high hardness (greater than 400 HV_{50}). Smaller islands appeared to have substantially lower microhardness at approximately 275 HV_{50}, but this value is consistent with that of the indent straddling the boundary between the thick band and ferrite. It is likely that these small bands were not of sufficient size to measure without capturing effects from the underlying soft ferrite matrix. The comparative microhardness values between constituents were echoed in a study by Huda *et al.*, where it was found that in a pipeline steel, untempered M/A constituent microhardness values were approximately twice that of the surrounding ferrite matrix [27]. In SEM images, all regions of tan-etched constituent are a mixture of a fine, needle-like phase and regions that appear to be a ferrite-carbide aggregate. Given the high microhardness and the morphology, it is likely that tan-etched regions are untempered martensite in combination with a ferrite-carbide aggregate. Without transmission electron microscopy (TEM), it is difficult to ascertain whether retained austenite is present within these complex mixtures. For the purpose of this report, the tan-etched

phase will be labeled as M/A constituent with the understanding that martensite is the majority phase present, as reflected by high microhardness values.

The only other microstructural feature of note in the slowly cooled sample were clusters of coarse precipitates adjacent to many of the martensite packets. This is consistent with the phenomenon of cementite nucleation and spheroidization into coarse Fe_3C particles during tempering of martensite in the general temperature range of 300-700 °C (572-1292 °F) [22]. Carbides could also be seen to a lesser extent scattered throughout ferritic regions. As expected of a mixture with a high amount of polygonal ferrite, the average microhardness is relatively low at 242 HV_{200}. If any tempered martensite was retained from the original base metal microstructure, it was no longer recognizable via either optical or scanning electron microscopy following the slow cooling thermal cycle. The base metal microhardness was measured to be 243 ± 7.7 HV_{200}, suggesting that its retained presence in the slowly cooled sample would have done little to increase the microhardness above values typical of ferrite, particularly after being further tempered by the CCT thermal cycle.

The sample heated to 785 °C (1445 °F) and cooled at 5 °C/s (9 °F/s) also shows a high-temperature transformation associated with quasipolygonal ferrite. The increased cooling rate depressed the transformation start temperature to 666 °C (1231 °F) and the finish temperature to 580 °C (1076 °F). At this temperature a second transformation is evident in the dilation curve, completing near 415 °C (779 °F). As with the sample cooled at 1 °C/s (1.8 °F/s), SEM analysis showed regions that were rich with unidentified precipitates (shown in **Figure 64**). Ferrite grain size dropped compared to the more slowly cooled sample as the material spent less time in high temperature regimes that facilitate grain growth. Banding was no longer present, suggesting that the phenomenon observed in the slowly cooled sample was not the result of banding in the base material; rather, the time spent in high temperature regime allowed for elemental segregation. Tempered martensite retained from the base material was present in this sample, with dilation curve analysis indicating a lack of newly formed martensite. Microhardness increased to 272 HV_{200}, reflecting both the reduced grain size and ferrite phase fraction.

Samples heated to 785 °C (1445 °F) and cooled at the intermediate rate of 25 °C/s (45 °F/s) exhibited a high temperature transformation beginning at 561 °C (1042 °F), respectively. This matched with the low fraction of quasipolygonal ferrite identified in micrographs. There appeared to be some bainite formation identifiable only via SEM with secondary particles aligned in very small packets. A low temperature transformation beginning at 395 °C (743 °F) and finishing at 319 °C (606 °F) for the samples cooled at 25°C/s (45 °F/s) was too low to be associated with any phase other than martensite. The volumetric fraction was fairly low, and was impossible to distinguish between tempered martensite that may have been retained from the base material. Microhardness values increased to 305 HV_{200}, expected with the reduction in ferrite and introduction of the harder martensitic constituent. The formation of martensite in these samples suggests that austenite was stable to lower temperatures. It is presumed that carbon and other alloying additions had sufficient time to preferentially migrate into from the tempered martensite retained from the base material and into the austenite during the additional time spent cooling, which stabilized that austenite to a lower temperature than observed in other samples.

Various constitutive equations for predicting the start temperatures for bainite and martensite transformations based on alloy chemistry are available in the literature [28] [29]. Such models are generally oversimplifications and often are only accurate for alloys similar to those used to create them, but they can act as a guide for reasonable temperatures at which to expect formation of intermediate and low temperature phases. As such, the models developed by Capdevilla *et al.* [30] and Kirkaldy [31] were applied to the measured HY-80 composition given in **Table 3**:

$$M_s = 491.05 - 302.6w_C - 30.6w_{Mn} - 16.6w_{Ni} - 8.9w_{Cr} + 2.4w_{Mo} - 11.3w_{Cu} + 8.58w_{Co} + 7.4w_W - 14.5w_{Si} \quad \textbf{(5)}$$

$$B_s = 656 - 57.7w_C - 75w_{Si} - 35w_{Mn} - 15.3w_{Ni} - 32w_{Cr} - 41.2w_{Mo} \quad \textbf{(6)}$$

where $M_s \equiv$ martensite start temperature (°C)
$B_s \equiv$ bainite start temperature (°C)
$w_i \equiv$ concentration of element i (wt%)

From **Equations 5** and **6**, the M_s and B_s temperatures for HY-80 are predicted to be 393 °C (739 °F) and 530 °C (985 °F), respectively. The predicted B_s temperature is consistent with the second phase transformation temperature of the sample cooled at 5 °C/s (9 °F/s), despite the somewhat loose resemblance of that microstructure to that of classic bainite. A partially bainitic microstructure was observed in the specimen cooled at 10 °C/s (18 °F/s) though no definitive transformation temperature could be determined from the dilatometry measurements. Both the predicted M_s and B_s temperatures match well with the measured transformation temperatures identified in the samples cooled at 25 °C/s (45 °F/s) despite the high likelihood of local elemental segregation and compositional differences from the chemistry used for the constitutive equation calculations.

Samples heated to 785 °C (1445 °F) and cooled at 100 and 200 °C/s (180 and 360 °F/s) were primarily martensitic. The small prior austenite grain size made it difficult to visually distinguish between the small packets of freshly formed martensite and any untransformed base material microstructure. Nevertheless, high microhardness values of 399 and 416 HV_{200} suggest a majority presence of freshly-formed, untempered martensite. Dilation curve analysis showed an intermediate temperature transformation beginning at 544 °C (1042 °F) for the sample cooled at 100 °C/s (180 °F/s), but no corollary transformation was identified in the sample cooled at 200 °C/s (360 °F/s). Both specimens exhibited a low temperature transformation, starting at 422 and 425 °C (792 and 797 °F) and finishing at 296 and 274 °C (565 and 525 °F) for the specimens cooled at 100 and 200 °C/s (180 and 360 °F/s), respectively. These temperature ranges are consistent with martensitic transformation in samples heated to higher peak temperatures. Optical microscopy showed featureless grains with a visual resemblance to ferrite. No high temperature transformation consistent with ferrite was detected in the dilation data, and given the short amount of time available for such diffusion-dependent transformation, these are more readily explained as artifacts of the orientation-dependent Nital etchant that was used for sample preparation.

The next simulated HAZ region was the FGHAZ, with a peak temperature of 1000 °C (1832 °F). Representative micrographs are presented in **Figure 65** of **Appendix C**, with measured phase fractions reported in **Table 5**. These samples fully austenitized prior to cooling, eliminating the original base material microstructure. The sample cooled at 1 °C/s (1.8 °F/s) exhibited a mixture of quasipolygonal ferrite, coarse bainite, and packets of martensite/austenite (M/A) constituent. While evident via optical microscopy, the ferrite volume fraction was not high enough to detect on the dilation curve. The only transformation apparent on the curve is the bainitic transformation, starting at 570 °C (1058 °F) and finishing at 395 °C (743 °F). Increasing the cooling rate to 5 °C/s (9 °F/s) decreased the amount of ferrite that could be identified in optical micrographs, though small grains are still visible. Once again there was no discernible high-temperature transformation in the dilation curve that corresponded to the presence of ferrite. The bainite morphology was much finer than that in the sample cooled at 1 °C/s (1.8 °F/s), without the relatively coarse packets of M/A constituent. Bainite start temperature dropped slightly to 571 °C (1060 °F) thanks to the higher cooling rate. Martensite was introduced at this cooling rate, with transformation beginning at 384 °C (723 °F). The reduction of ferrite, refinement of bainite laths, and addition of martensite all led to an increase of microhardness from 263 to 303 HV_{200}. The same phases

were all present in the sample cooled at 10 °C/s (18 °F/s), with an increase in martensite phase fraction. This was accompanied by another increase in average microhardness, up to 357 HV_{200}.

Table 5. Measured Phase Fraction of HY-80 CCT Specimens Thermally Cycled to a Peak Temperature of 1000 °C (1832 °F)

Cooling Rate		Peak Temperature = 1000 °C (1832 °F)		
°C/s	°F/s	F + M/A	B	M
1	1.8	0.24	0.76	0
5	9	0.08	0.53	0.39
10	18	0.06	0.41	0.53
25	45	0	0.17	0.83
100	180	0	0	1
200	360	0	0	1

The sample cooled at 25 °C/s (45 °F/s) had an intermediate temperature transformation associated with bainite at 540 °C (1004 °F), followed immediately by a martensitic transformation across the temperature range of 413 to 285 °C (775 to 545 °F). The bainite was much more refined than that seen in the more slowly cooled samples for this peak temperature. The higher volumetric fraction of martensite coincided with an increase in microhardness to 398 HV_{200}. Samples rapidly cooled at 100 and 200 °C/s (180 and 360 °F/s) were entirely martensitic, with respective transformation start temperatures of 423 and 419 °C (793 and 786 °F) and finish temperatures of 271 and 273 (520 and 523 °F). Microhardness increased to 426 and 423 HV_{200}. It is notable that, as with the ICHAZ samples, the M_s temperatures increased slightly as cooling rate increased. This is likely due to the same phenomena discussed previously: as austenite transformed to ferrite, carbon was rejected back into the remaining austenite, locally increasing its alloying content and stabilizing it to lower temperatures. Therefore, the samples that cooled slowly enough to form ferrite experienced martensite formation at slightly lower temperatures than expected for the same bulk chemistry.

The third peak temperature investigated was also representative of the FGHAZ, but with a slightly higher peak temperature of 1150 °C (2102 °F). Representative micrographs are shown in **Figure 66** in **Appendix C**, with measured phase fractions reported in **Table 6**. There is a qualitative increase in packet size compared to samples heated to 1000 °C (1832 °F), indicating that the higher peak temperature allowed significant austenite grain growth. The microstructure of the sample cooled at 1 °C/s (1.8 °F/s) consisted entirely of coarse bainite with aligned M/A constituent along ferrite laths, which began transformation at 570 °C (1058 °F) and completed transformation at 406 °C (763 °F). Average microhardness was measured to be 267 HV_{200}.

Table 6. Measured Phase Fraction of HY-80 CCT Specimens Thermally Cycled to a Peak Temperature of 1150 °C (2102 °F)

Cooling Rate		Peak Temperature = 1150 °C (2102 °F)		
°C/s	°F/s	F + M/A	B	M
1	1.8	0	1	0
5	9	0	0.80	0.20
10	18	0	0.08	0.92
25	45	0	0	1
100	180	0	0	1
200	360	0	0	1

Increasing the cooling rate to 5 and 10 °C/s (9 and 18 °F/s) dropped the bainite start temperature to 544 and 490 °C (1011 and 914 °F), respectively, thanks to the increased undercooling associated with higher cooling rates. The bainite laths were finer than those in the slowly cooled samples, again attributed to cooling rate. Lath martensite was also introduced in these samples, as evident in micrographs and reflected in the increased microhardness values, rising to 329 and 378 HV_{200}, respectively. The bainite volume fraction in the sample cooled at 10 °C/s (18 °F/s) was so small that it was not detected in the dilation curve.

Samples cooled between 25-200 °C/s (45-360 °F/s) were all completely martensitic. Average microhardness values rose slightly with cooling rate, with measurements of 409, 415, and 419 HV_{200}. M_s temperatures associated with these samples were slightly higher than those associated with samples cooled at the same rate but heated to a lower peak temperature, likely due to increased homogenization at higher temperatures.

The final simulated region was the CGHAZ, with a peak temperature of 1350 °C (2462 °F). Representative micrographs are shown in **Figure 67** in **Appendix C**, with measured phase fractions reported in **Table 7**. Material response to cooling rates for this peak temperature was very similar to that described for a peak temperature of 1150 °C (2102 °F). In each case, the sample cooled at 1 °C/s (1.8 °F/s) was composed entirely of coarse bainite, with fine aligned M/A constituent within large ferrite laths. Average microhardness for the slowly-cooled CGHAZ sample was slightly lower, measuring 251 HV_{200} compared to the 267 HV_{200} recorded for the FGHAZ sample. It can be speculated that the peak temperature of 1350 °C (2462 °F) provided sufficient thermal energy to dissolve precipitates that persisted in the lower peak temperature sample, imparting additional hardness to the FGHAZ specimen despite no clear differences detected via optical microscopy.

Table 7. Measured Phase Fraction of HY-80 CCT Specimens Thermally Cycled to a Peak Temperature of 1350 °C (2462 °F)

Cooling Rate		**Peak Temperature = 1350 °C (2462 °F)**		
°C/s	**°F/s**	**F + M/A**	**B**	**M**
1	1.8	0	1	0
5	9	0	0.40	0.60
10	18	0	0.08	0.92
25	45	0	0	1
100	180	0	0	1
200	360	0	0	1

The samples heated to 1350 °C (2462 °F) and cooled at 5 and 10 °C/s (9 and 18 °F/s) were comprised of extremely fine bainite and martensite. Volumetric fraction martensite increased with cooling rate, as did microhardness, which rose from 325 to 385 HV_{200}. Samples cooled at 25-200 °C/s (45-360 °F/s) were each entirely martensitic. M_s temperatures were higher for these samples than any others, with transformation beginning at 450, 455, and 458 °C (842, 851, and 856 °F).

The phase transformation information developed here is critically important for ensuring that weld simulation software can draw on thermo-physical and thermo-mechanical property information from the appropriate phases at the appropriate times during calculations. The results in **Figures 9-15** highlight the importance of developing multiple HAZ-related CCT diagrams.

Weldment Microstructures

Metallographic specimens were removed from both weldments and analyzed in a manner similar to the Gleeble specimens. Discussion of the microstructures present correspond to the HAZ of the second pass for each weldment, as the reheating experienced by the first pass confounded the analysis and do not directly correlate with thermal cycles undergone by Gleeble CCT specimens, making them unsuitable for the intended purpose of experimental validation.

The fusion zone for each joint configuration was a mixture of coarse primary ferrite, acicular ferrite, and unidentified carbides. **Figure 17** presents representative micrographs for the butt joint and tee joint fusion zones. Microhardness values ranged from approximately 230-270 HV_{200}. It is noted that the microstructure is finer in the butt joint fusion zone, while the fusion zone of the tee joint has more coarse primary ferrite grains. This is reflective of the two different processes used to deposit the welds, with submerged arc welding (SAW) used for the butt joint and flux-cored arc welding (FCAW) used for the tee joint. Specific welding parameters are provided in **Table 2**. Heat input, filler wire diameter, and interpass temperature were different for each weldment and each likely contributed to differences in thermal histories that would drive variation in resulting microstructure. It is likely that the weld metal associated with the butt joint cooled more rapidly than the tee joint, allowing less time for nucleation and growth of primary ferrite grains and instead favoring acicular ferrite formation.

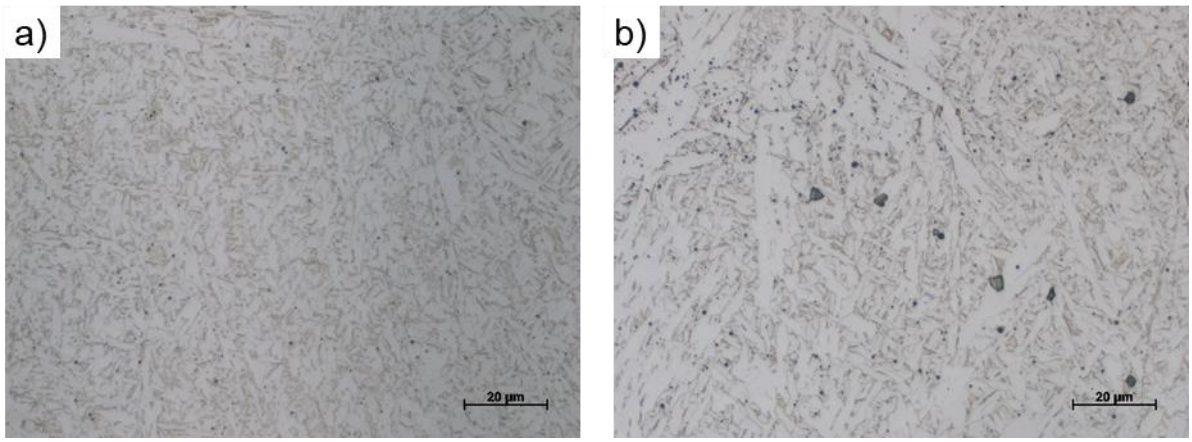

Figure 17. Representative microstructures of the second pass fusion zone for the **a)** butt joint and **b)** tee joint configuration.

Representative HAZ microstructures for the second pass of the HY-80 butt joint are presented in **Figure 18**. A microhardness map with truncated color scale is provided in **Figure 19**. As microhardness values for each joint were within the same range, the same color scale is used for both. The map shows measurements values for indents spaced at intervals of 500 µm in both the horizontal and vertical directions, with numerical values provided in **Table 16** in **Appendix D**. The CGHAZ directly adjacent to the fusion line was associated with the lowest microhardness in the HAZ, measuring at 234 $HV_{200.}$ **Figure 18a** reveals a bainitic microstructure with large prior austenite grain size. Two FGHAZ regions were evaluated at distances from the fusion line of 450 and 900 µm. Microhardness increased with distance from fusion line to 260 and 294 HV_{200}. Micrographs adjacent to those microhardness indents are shown in **Figure 18b** and **Figure 18c**, respectively. Prior austenite grain size is qualitatively smaller than that observed in the CGHAZ, with microstructures comprised of a mix of bainite and martensite. Some regions appear to be unetched, which is presumed to be an orientation effect wherein martensitic regions etched less readily. The increase in microhardness is attributed to a Hall-Petch effect from the decreasing

grain size. The ICHAZ is shown in **Figure 18d**, characterized by a microhardness value of 274 HV_{200}. Microhardness continued to fall as distance increased from the fusion line and into the unaffected base material. The microstructure in the ICHAZ resembled the mixture produced in the ICHAZ Gleeble simulation that was cooled at 5 °C/s (9 °F/s), with small grains of ferrite, clusters of precipitates, and what appears to be fine packets of fresh martensite.

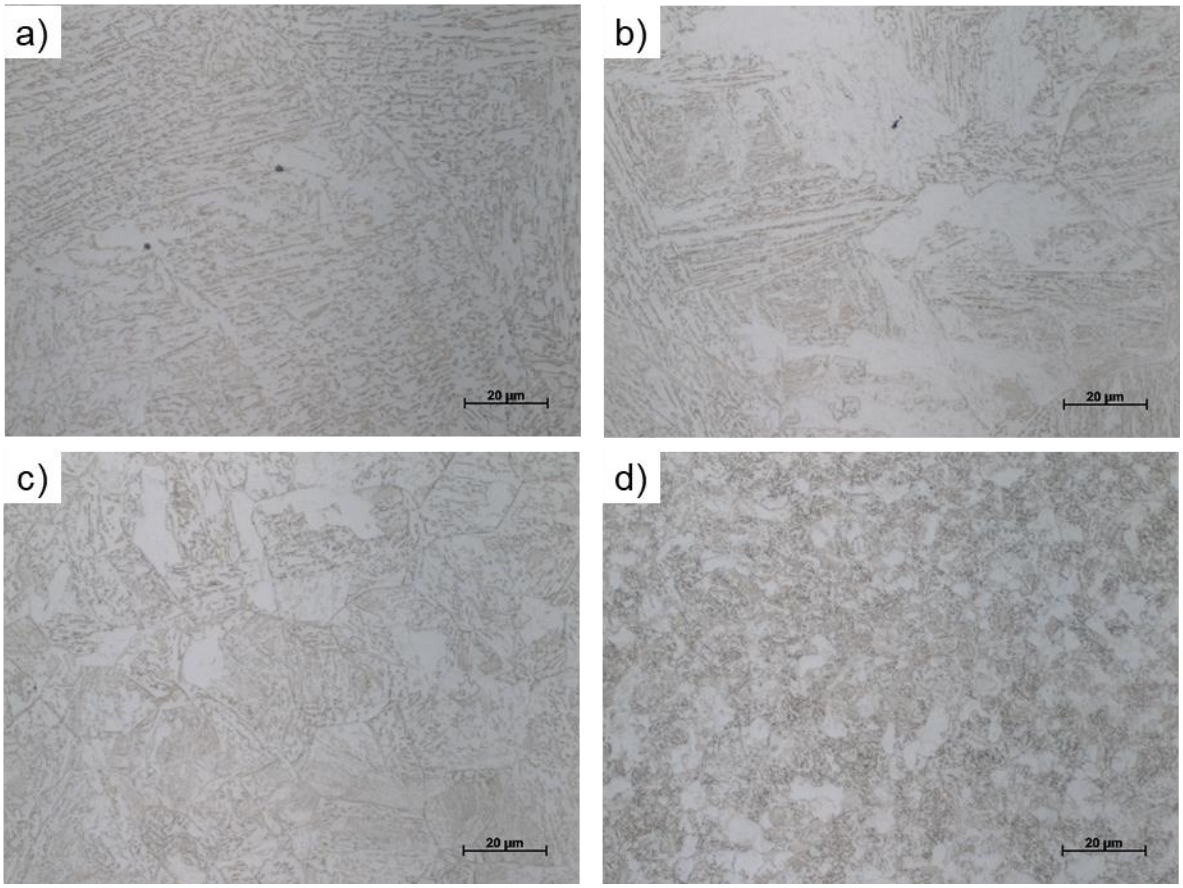

Figure 18. Representative light optical micrographs associated with the second pass of the HY-80 butt joint **a)** CGHAZ, **b)** FGHAZ close to the CGHAZ, **c)** FGHAZ close to the ICHAZ, and **d)** ICHAZ.

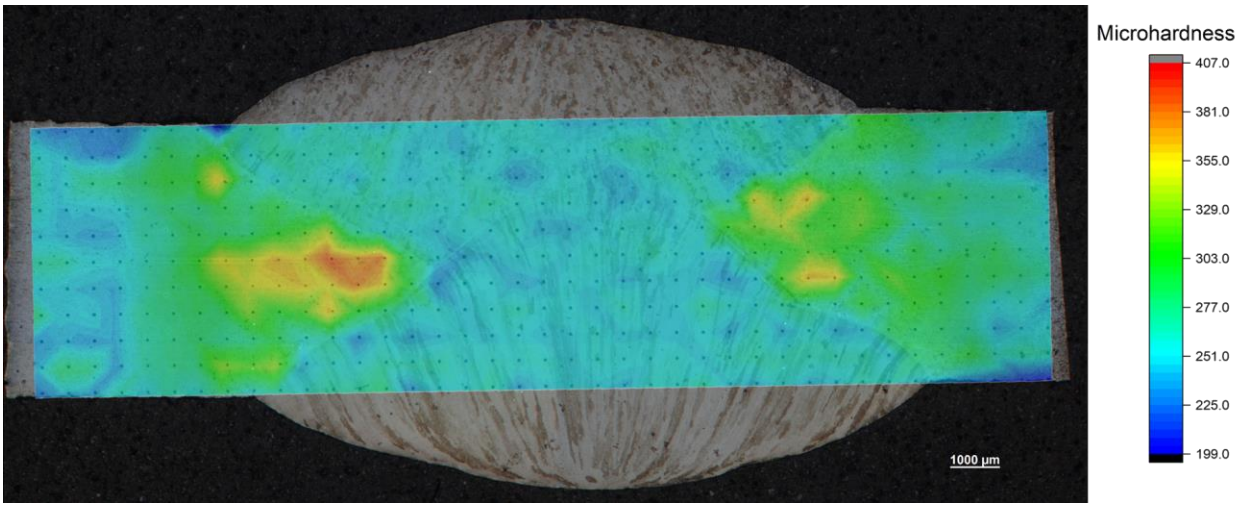

Figure 19. Composite image of light optical micrographs of the HY-80 butt joint overlaid with contour map of microhardness values in units of HV_{200}. Color scale is the same as that shown in **Figure 21** for a direct comparison of the two joint configurations.

Representative HAZ microstructures for the second pass of the HY-80 tee joint are presented in **Figure 20**. A microhardness map with full-range color scale is provided in **Figure 21**, showing a map of indents spaced at intervals of 500 µm in both the horizontal and vertical directions. Numerical values are provided in **Table 17** in **Appendix D**. Tee joint HAZ microhardness was in general slightly higher than those in the butt joint, likely due to thermal cycle differences driven by the two welding processes. The heat input associated with butt joint was higher (0.92-0.99 kJ/mm compared to 0.68-0.70 kJ/mm) and the process is associated with a blanket of granular flux on the joint. Thus not only was more heat put into the butt joint, but the flux likely acted as an insulator, reducing cooling rate. This is reflected in the bainitic CGHAZ of the butt joint, whereas the tee joint CGHAZ was composed of martensite.

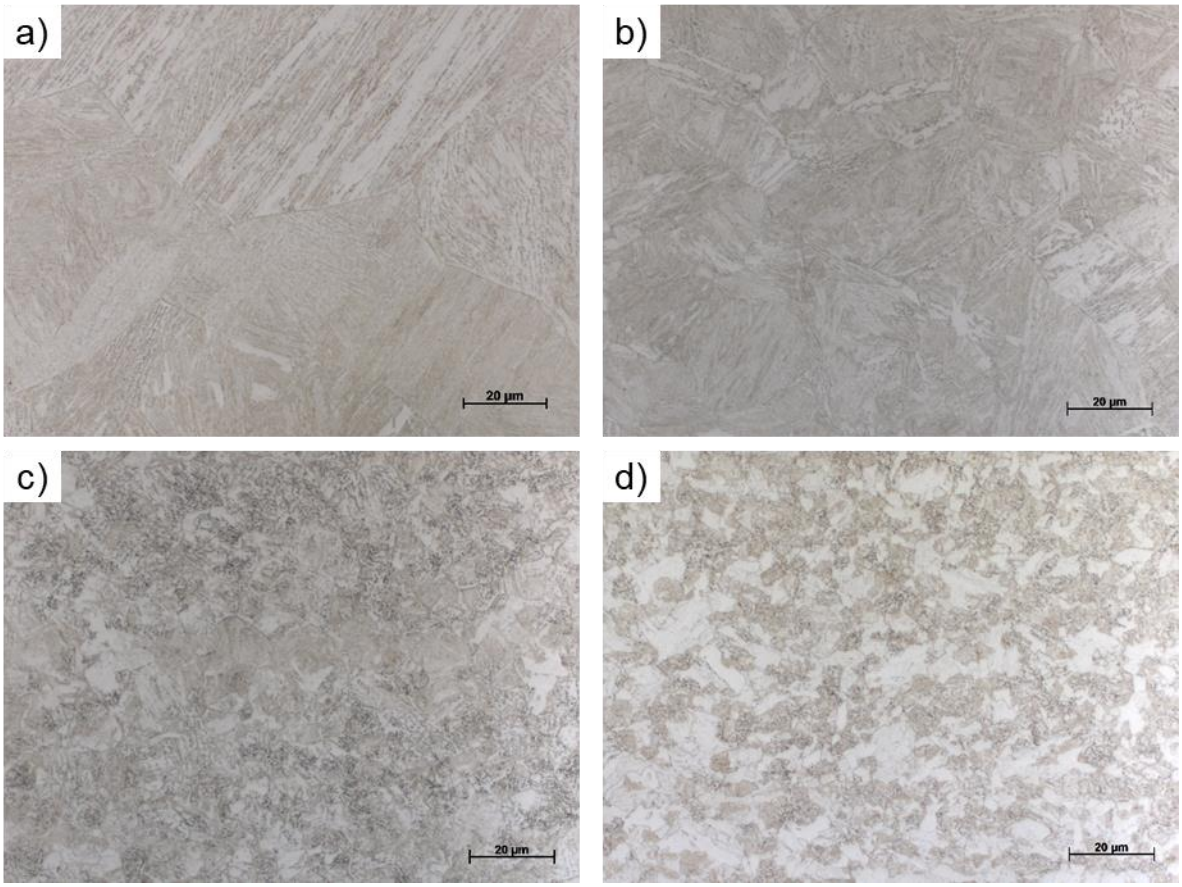

Figure 20. Representative light optical micrographs of the second pass of the HY-80 tee joint **a)** CGHAZ, **b)** FGHAZ close to the CGHAZ, **c)** FGHAZ close to the ICHAZ, and **d)** ICHAZ.

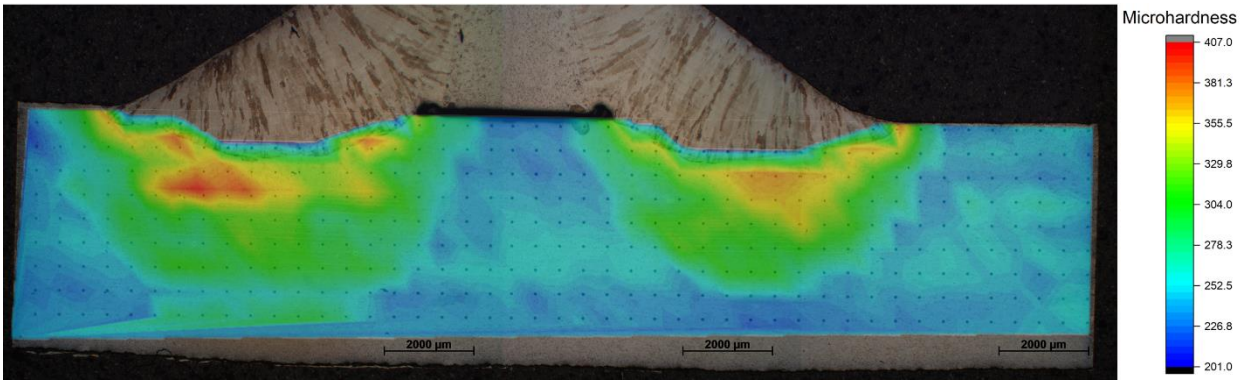

Figure 21. Composite image of light optical micrographs of the HY-80 tee joint overlaid with contour map of microhardness values in units of HV_{200}. Color scale is the same as that shown in **Figure 19** for a direct comparison of the two joint configurations.

Microhardness values measured in the butt joint matched well with those in the tee joint despite the reheated nature of HAZ regions in the butt joint. Gleeble sample microstructures generally matched well with experimental weldments, though generally the Gleeble samples that matched with the tee joint

were associated with higher cooling rates than those matching the butt joint. This is consistent with expected cooling rate

Thermo-Physical Property Analysis

The average CTE values measured from the dilation curves (n=5) were 1.53 x 10^{-5} ± 6.23 x 10^{-7} °C^{-1} (8.5 x 10^{-6} ± 3.5 x 10^{-7} °F^{-1}) for the untransformed base metal below 700 °C (1292 °F) and 2.19 x 10^{-5} ± 5.63 x 10^{-7} °C^{-1} (1.2 x 10^{-5} ± 3.1 x 10^{-7} °F^{-1}) for austenite above 880 °C (1616 °F). A representative graph showing the CTE measurement is given in **Figure 22**.

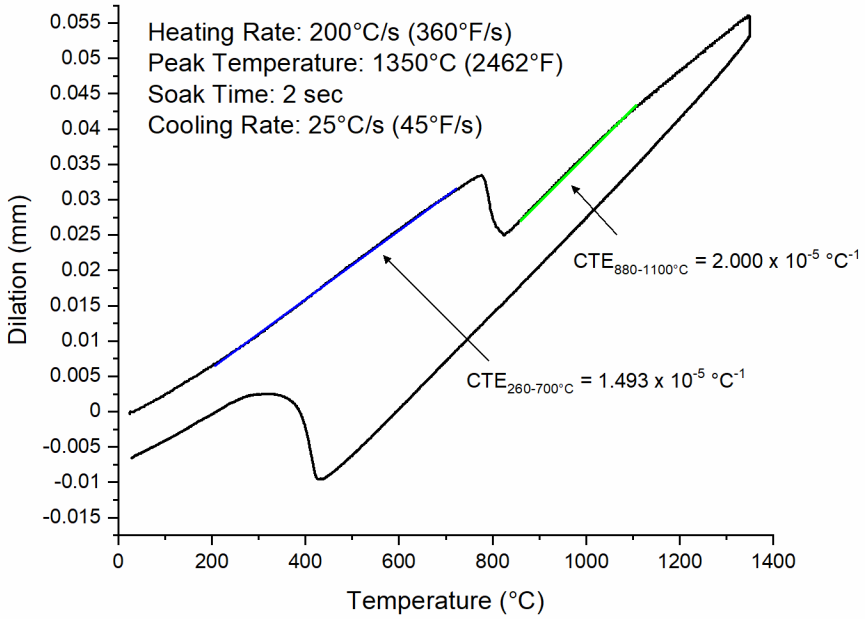

Figure 22. Representative on-heating dilatometry curve for HY-80, showing typical CTE analysis and results.

Temperature-dependent density values are shown in **Figure 23**. Two room temperature density values from literature are shown for comparison. As those data points are over 30 years old (Honeywell report [19]) or 50 years old (Alloy Digest [32]), differences are attributed to either improved measurement techniques since those data were collected or modifications in mill practices relative to HY-80 composition.

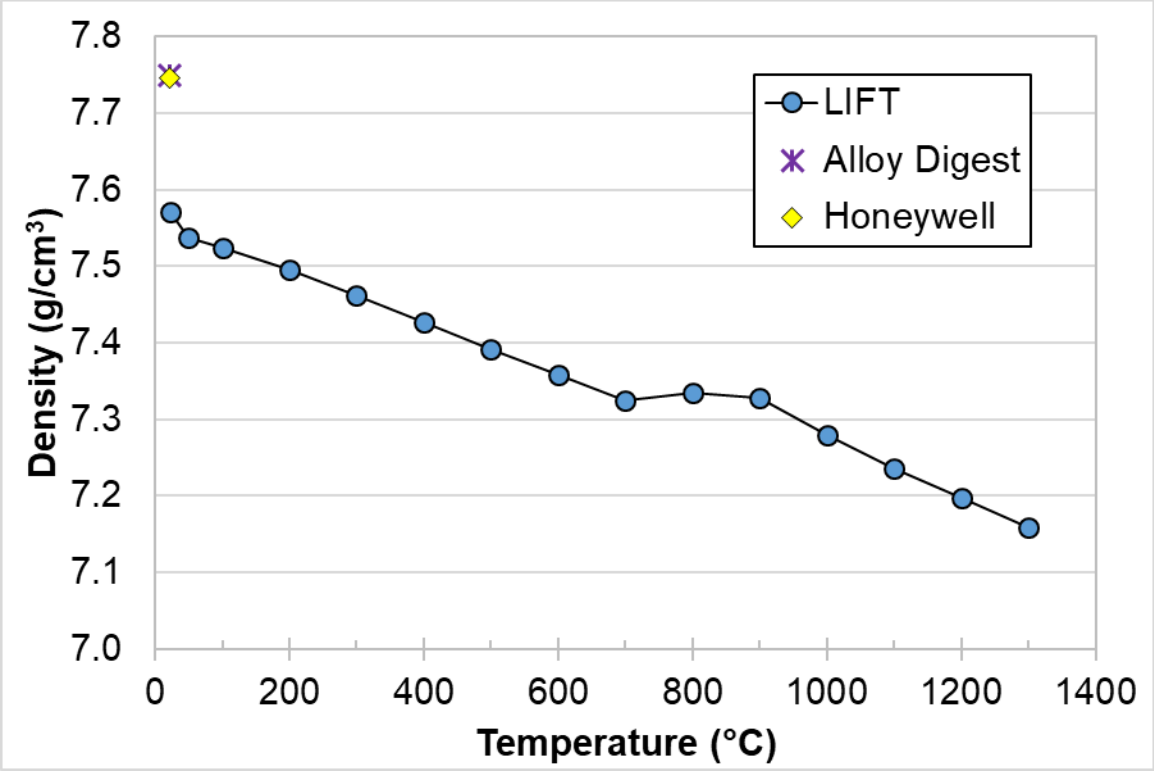

Figure 23. Density of HY-80 steel as a function of temperature. LIFT data measured using analysis of Gleeble-based dilation curves in accordance with **Equations 2** and **3**. Room temperature comparison values were converted from reference [19] [32].

The measured specific heat and thermal diffusivity data for HY-80 can be found in **Figures 24-25**. The peaks or cusps in the data correspond to the effects of thermal energy absorption during phase transformations, particularly during the austenitic transformation between approximately 700 to 900 °C (1292 to 1652 °F). As shown, the data from this program compare well with room temperature values from a Honeywell report [19] and temperature-dependent values from a U.S. Steel report [17].

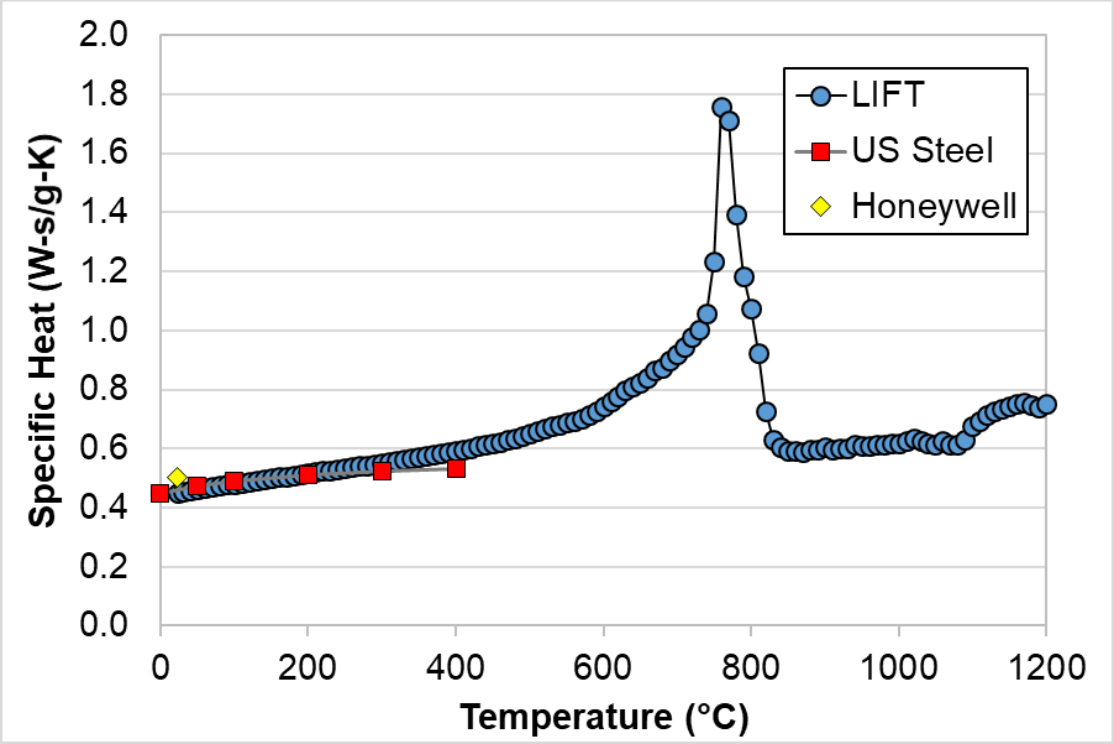

Figure 24. Measured specific heat for HY-80 steel at various temperatures. U.S. Steel data adapted from reference [17] and Honeywell data from reference [19].

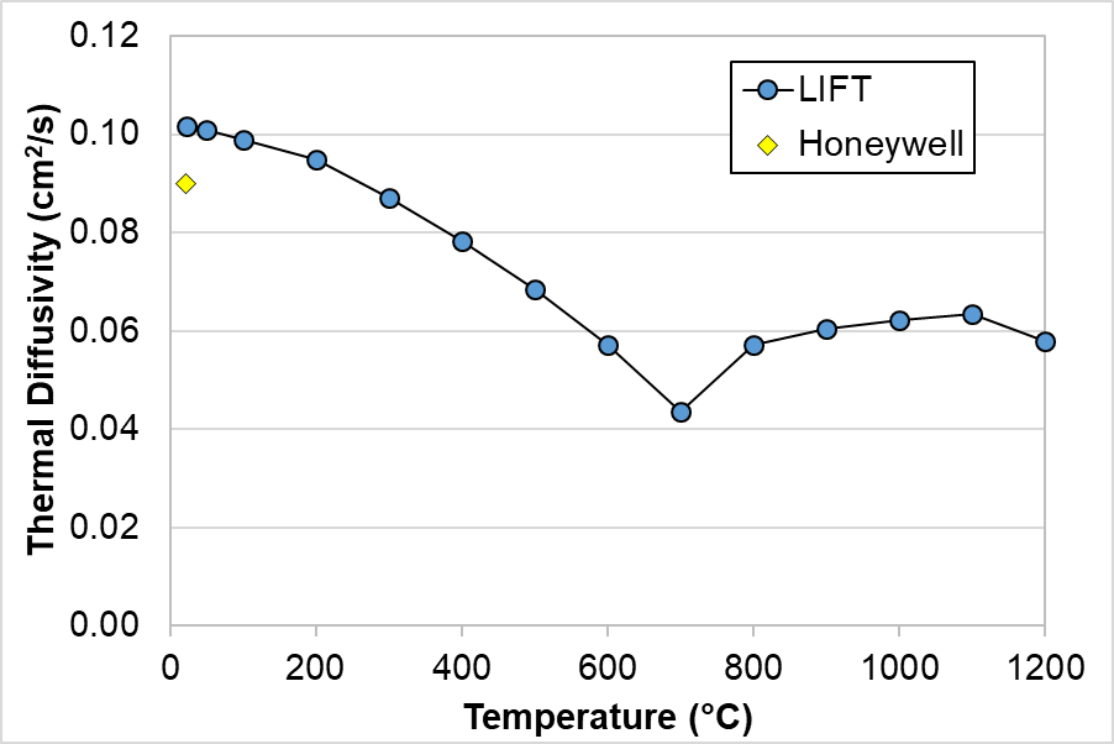

Figure 25. Measured thermal diffusivity for HY-80 steel at various temperatures. Honeywell data adapted from reference [19].

Finally, the data from **Figures 23-25** were used in conjunction with **Equation 4** to calculate the temperature-dependent thermal conductivity as shown in **Figure 26**. Once again, the data coincides fairly well with the previous reporting from U.S. Steel and Honeywell. The raw data points for all of the thermo-physical property graphs can be found in **Appendix E**.

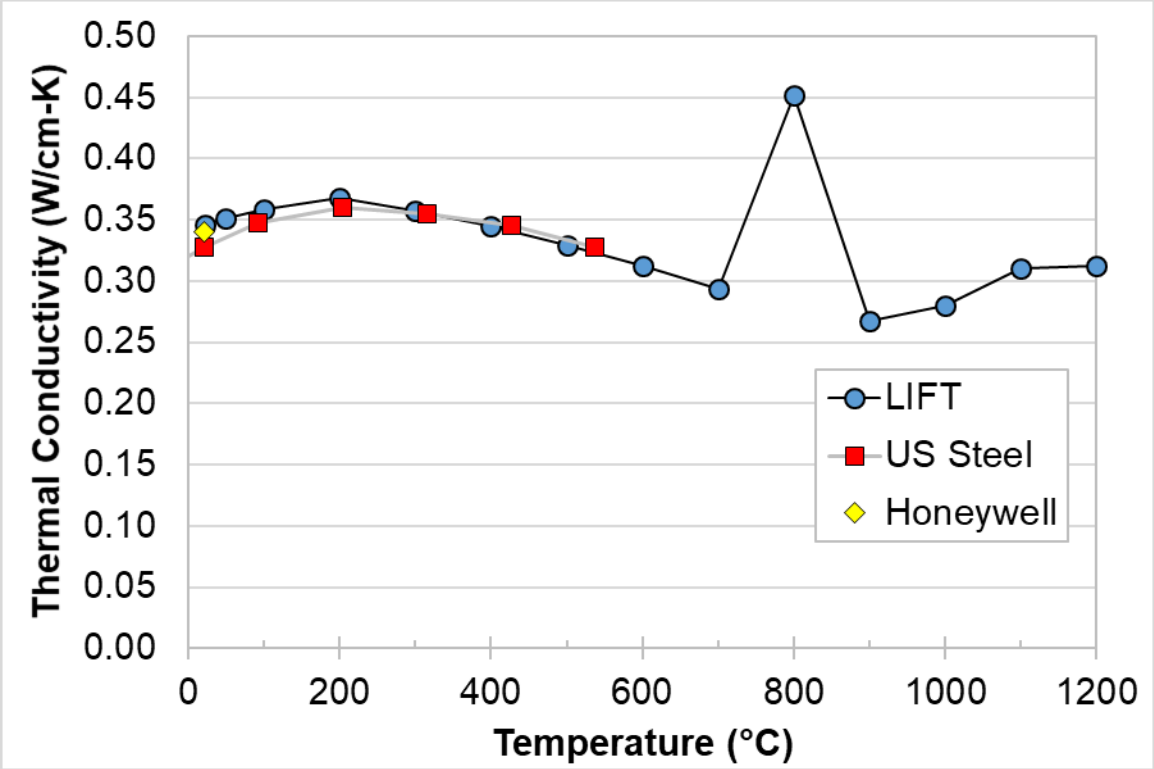

Figure 26. Calculated thermal conductivity for HY-80 steel at various temperatures. U.S. Steel data adapted from reference [17] and Honeywell data from reference [19].

Thermo-Mechanical Property Analysis

Figure 27 shows the values for elastic modulus as a function of temperature that were assumed in this work. The elevated temperature mechanical testing described above was performed in accordance with ASTM E21 [14] rather than the more appropriate ASTM E111 [33], which is prescribed when elastic modulus measurements are to be made. As such, it was determined that the experimentally measured elevated temperature elastic moduli were likely inaccurate. In order to provide elevated temperature modulus values for a HY-80 property database, the data in **Figure 27** were adapted from the European standard for fire design of steel structures [34] [35]. Of the potential sources for this information, the European standard contained the most complete data covering temperatures relevant to this study. A room temperature elastic modulus of 210 GPa (30.5 Msi) was assumed [34], as it had been previously for DH36 [5], HSLA-65 [6], HSLA-80 [7], and HSLA-100 [8] steel. It was also assumed that rigorously measured elastic moduli for HY-80 steel would be very similar to data presented in **Figure 27** because elastic properties tend to be consistent within a given material system (*e.g.*, steel). For comparison, room temperature values for elastic modulus from a Honeywell report [19] and a range of values reported from the Alloy Digest [32] are plotted as well.

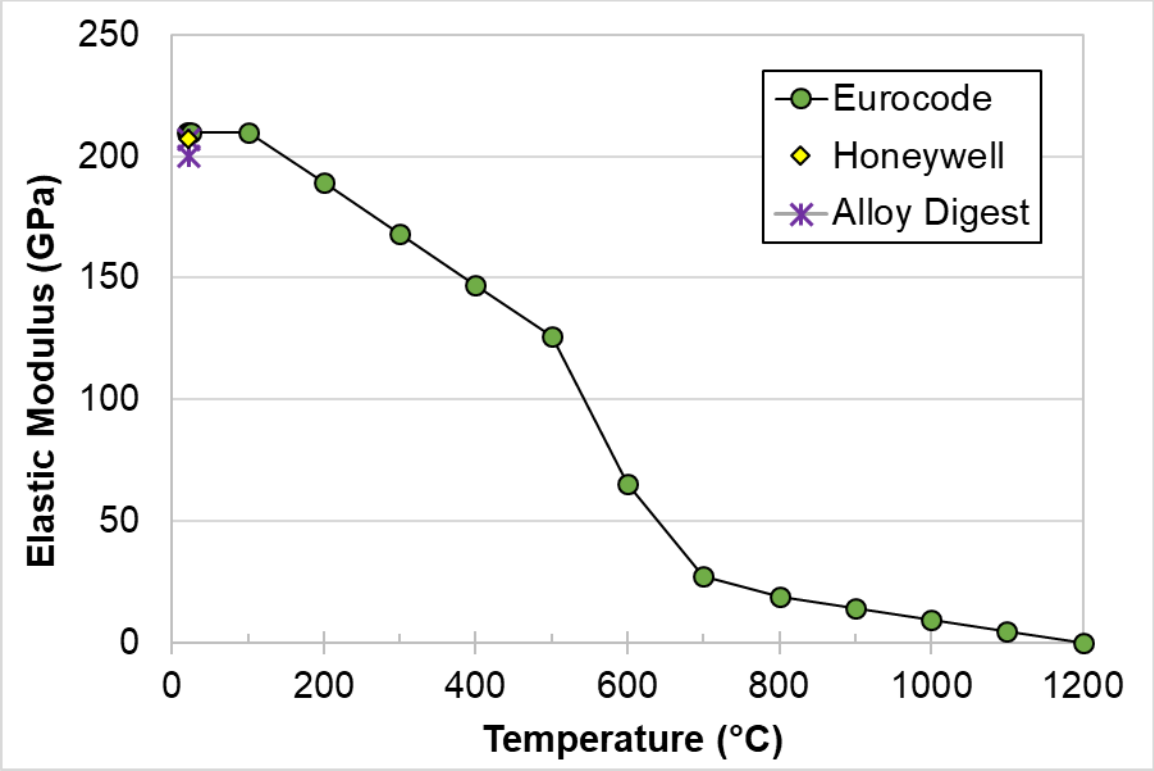

Figure 27. Assumed elevated temperature elastic modulus for HY-80 steel as adapted from references [34] [35]. Room temperature values from Honeywell adapted from reference [19] and the range of values from the Alloy Digest were adapted from reference [32].

Figure 28 shows the experimentally measured temperature-dependent 0.2% offset yield strength for HY-80 base material, and **Figure 29** shows the measured temperature-dependent ultimate tensile strength (UTS) of the base material as compared to data from U.S. Steel [16]. As expected, increased temperatures result in significant strength loss. At temperatures above 800 °C (1472 °F), the base metal microstructure is completely transformed to the weaker austenite phase, resulting in relatively minor differences in strength with increasing temperature. As shown, the base material and slow cooled data from this program compare well temperature-dependent values from a U.S. Steel report [16].

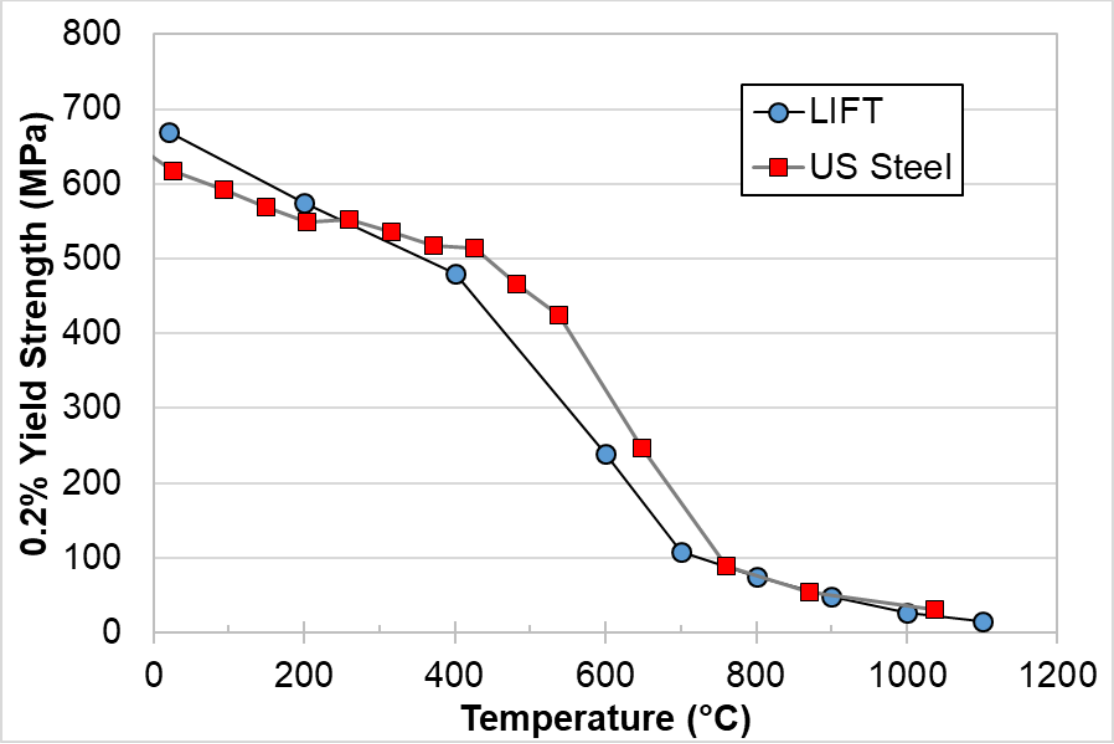

Figure 28. Measured elevated temperature 0.2% offset yield strength for HY-80 steel. U.S. Steel data adapted from reference [16].

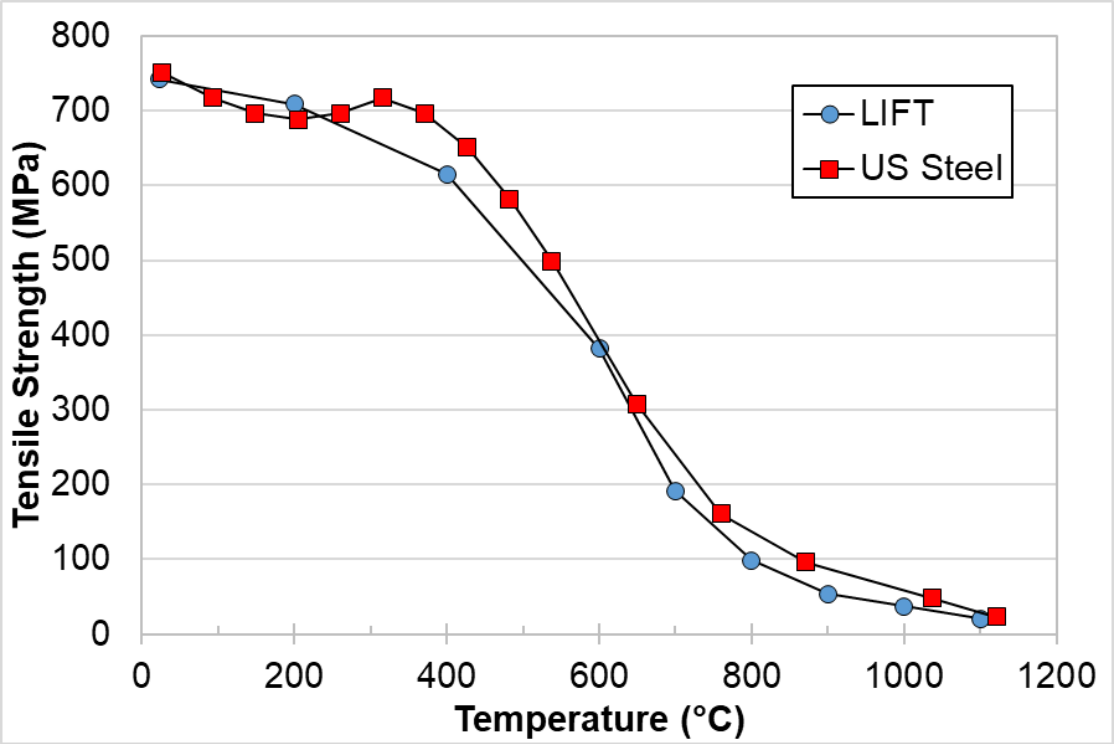

Figure 29. Measured elevated temperature ultimate tensile strength (UTS) for HY-80 steel. U.S. Steel data adapted from reference [16].

Figure 30 shows the measured 0.2% offset yield strengths and **Figure 31** shows the ultimate tensile strengths of specimens cycled to a peak temperature of 1350 °C (2462 °F), along with those of the base metal on-heating for comparison. The stress-strain curves associated with the data are given in **Figure 68**-**Figure 71** of **Appendix F**. All samples reached the required minimum yield strength of 552 MPa (80 ksi) at room temperature. The sample cooled at 1 °C/s (1.8 °F/s) was the only specimen that did not exceed the yield strength of the base material, reaching a room temperature yield strength of 580 MPa (84 ksi) compared to the base material's 670 MPa (97 ksi). Samples cooled between 10-100 °C/s (18-180 °F/s) each achieved nearly double the yield strength of the sample cooled at 1 °C/s (1.8 °F/s), with an average room temperature yield strength of 1066 MPa (155 ksi). All conditions exceeded the ultimate tensile strength of the base material below 600 °C (1112 °F). These results are consistent with microstructural characteristics of the samples: the three rapidly cooled samples all achieved similar, entirely martensitic microstructures, while the sample cooled at 1 °C/s (1.8 °F/s) consisted of a coarse bainite. The strength also follows microhardness trends, with the low strength, slowly cooled bainitic sample measuring 251 HV_{200} and the rapidly cooled samples measuring 385, 405, and 412 HV_{200}.

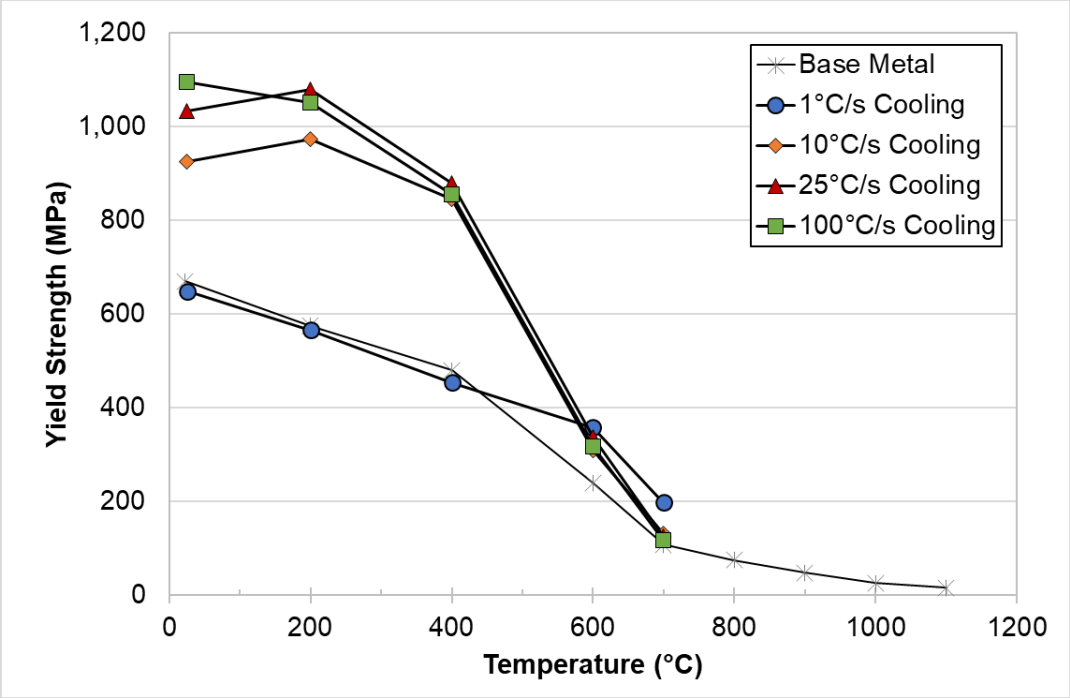

Figure 30. Yield strength of simulated HY-80 CGHAZ after heating to 1350 °C (2462 °F) and cooling at different rates as compared with base material yield strength.

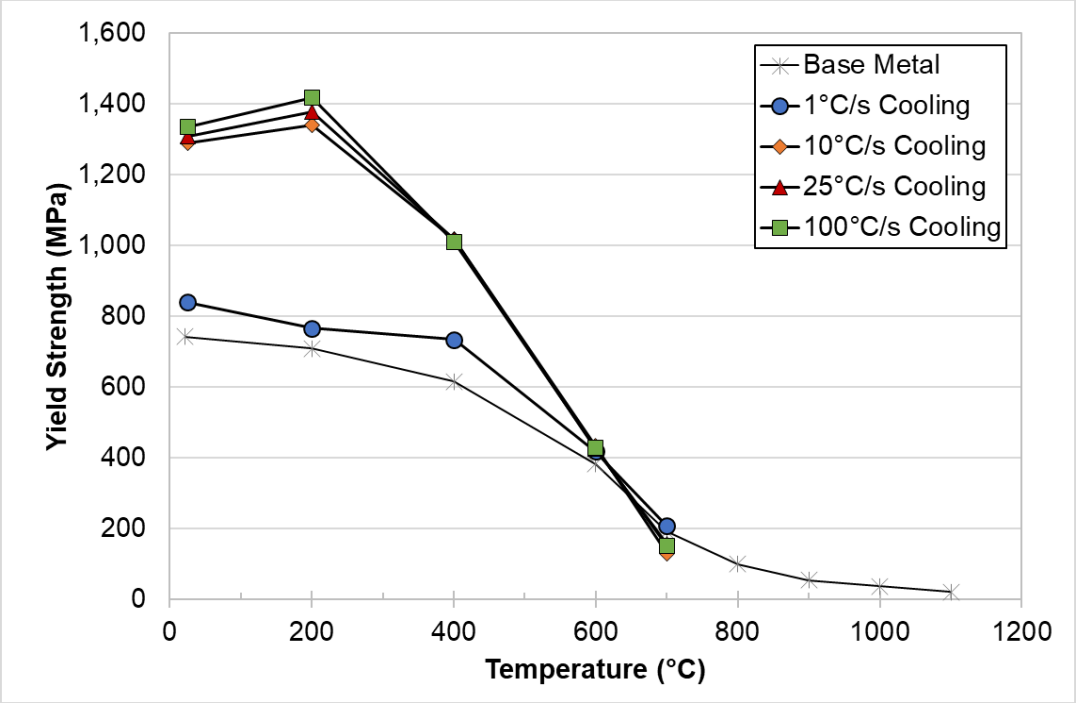

Figure 31. Ultimate Tensile strength of simulated HY-80 CGHAZ after heating to 1350 °C (2462 °F) and cooling at different rates as compared to base material UTS.

On-heating flow stress measurements for the HY-80 base material are shown in **Figure 32** for all temperatures, and **Figure 33** highlights the flow behavior for tests at temperatures of 800 °C (1472 °F) and above. The raw data points for these graphs can be found in **Appendix F**. The data are true stresses and strains calculated by applying the traditional conversion equations to engineering stress-strain data provided by the test lab. In several cases, the data seemed to show indefinite work hardening (*i.e.*, there was no plateau of stress values as strain increased). The experimental mechanism behind this behavior was unclear, but it was judged to be an artifact of the test method rather than a reflection of actual material behavior. In these cases, the UTS values were unclear, and as a result, further testing was performed in order to provide estimates in **Appendix F**. As expected, increasing the test temperature tends to flatten the flow stress curves, since work hardening is made more difficult by dynamic recovery and/or recrystallization effects.

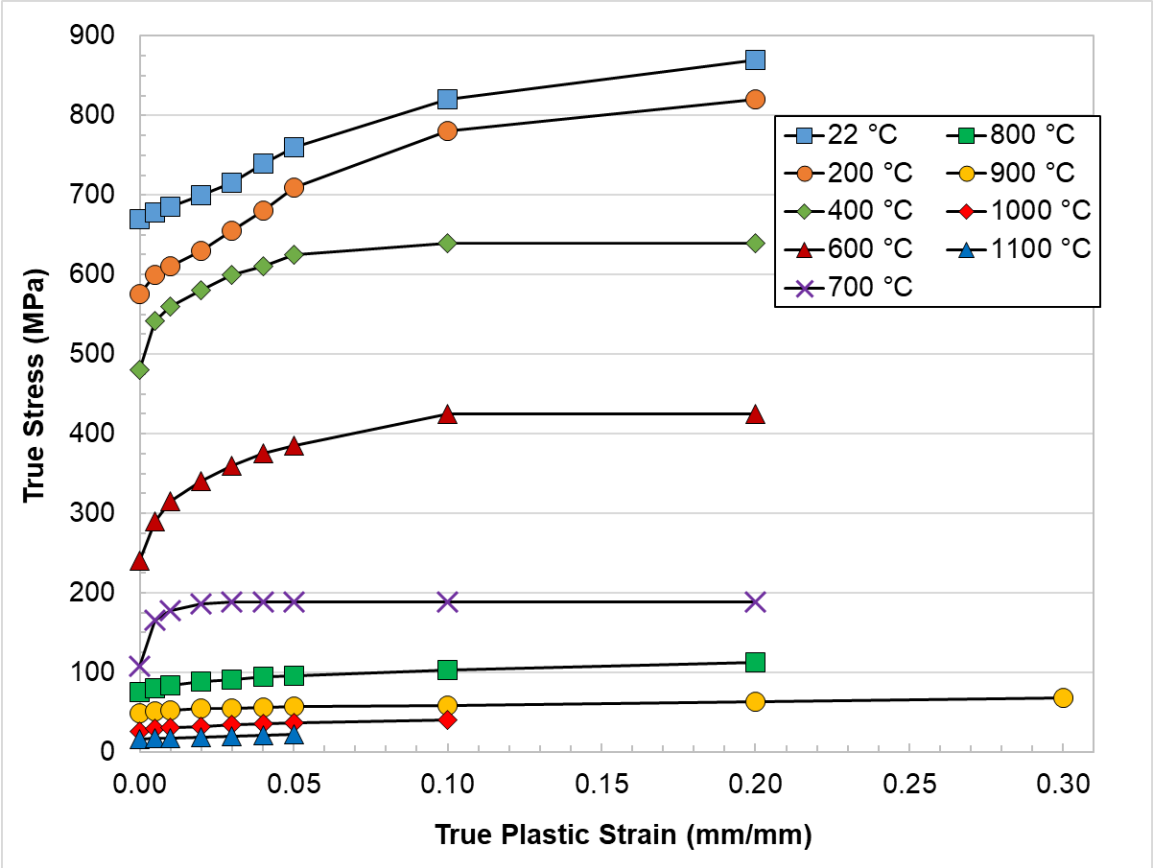

Figure 32. On-heating flow stress behavior for HY-80 steel at various temperatures.

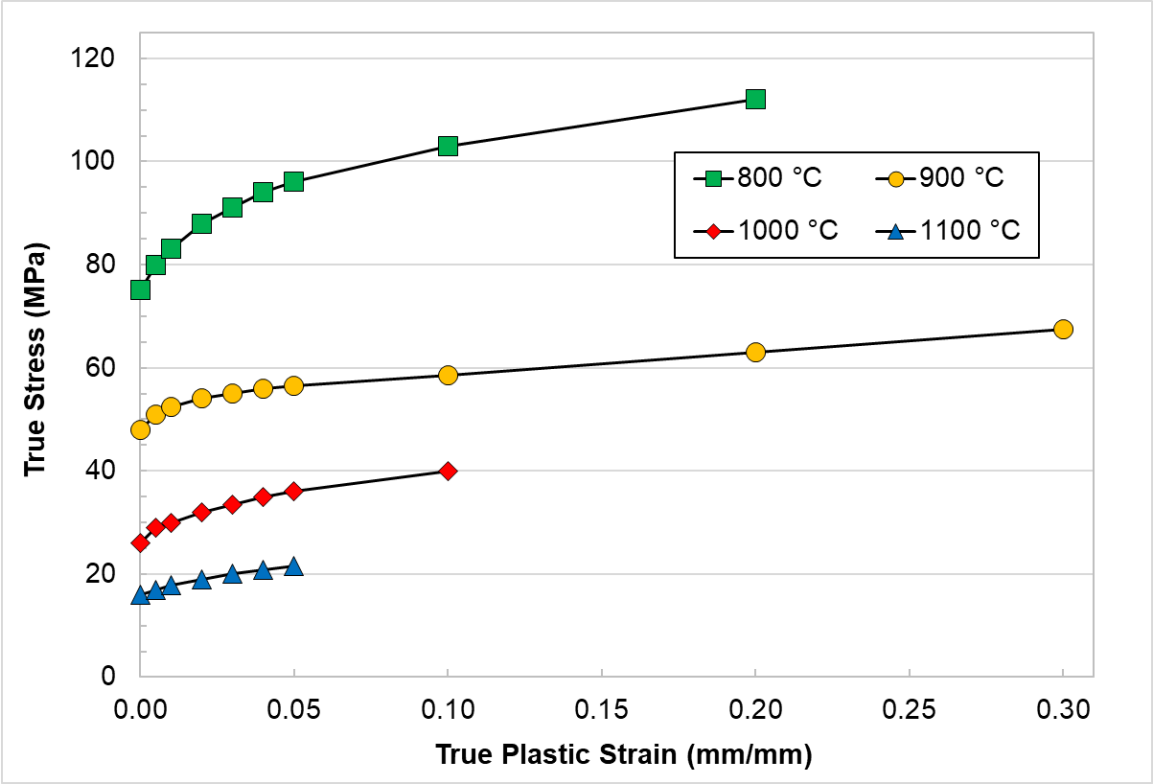

Figure 33. On-heating flow stress behavior for HY-80 steel at testing temperatures above the austenitic phase transformation.

Flow stress curves for the thermally cycled HY-80 are given in **Figures 34-37**. Once again, the data are true stresses and strains calculated by conversion from engineering stress-strain data. Such conversions are invalid past the onset of necking, so the terminal data points in **Figures 34-37** are at the UTS. All raw data points for these figures, along with the engineering fracture strains for the specimens, are found in **Appendix F**.

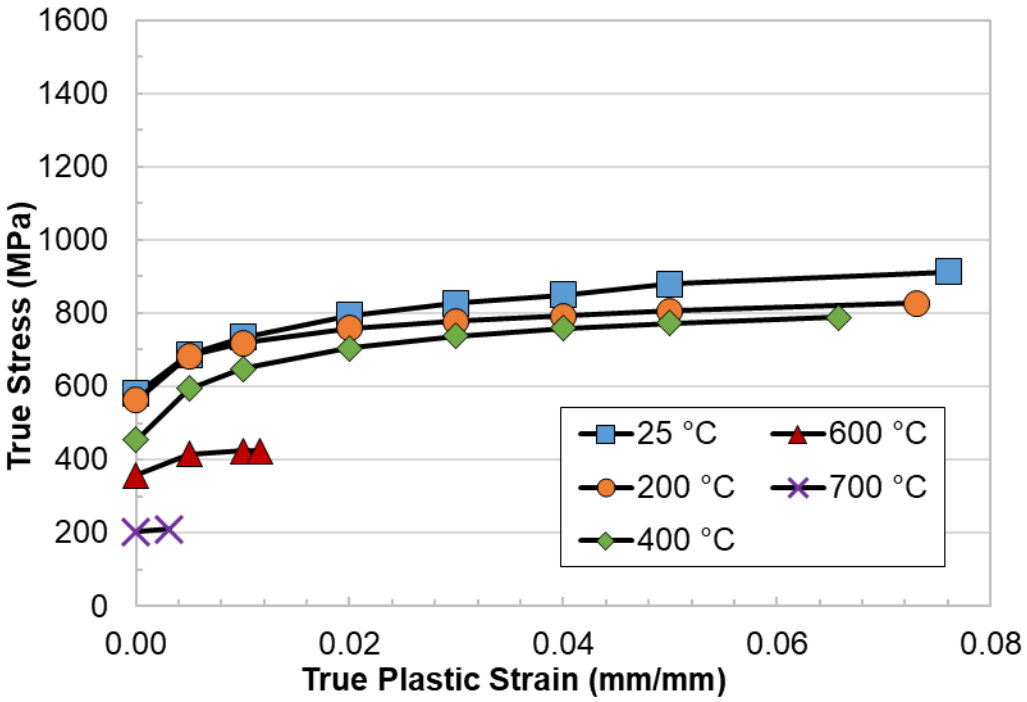

Figure 34. Flow stress behavior at various temperatures for HY-80 steel after cooling at 1 °C/s (1.8 °F/s) from a peak temperature of 1350 °C (2462 °F). Terminal data points are at the UTS.

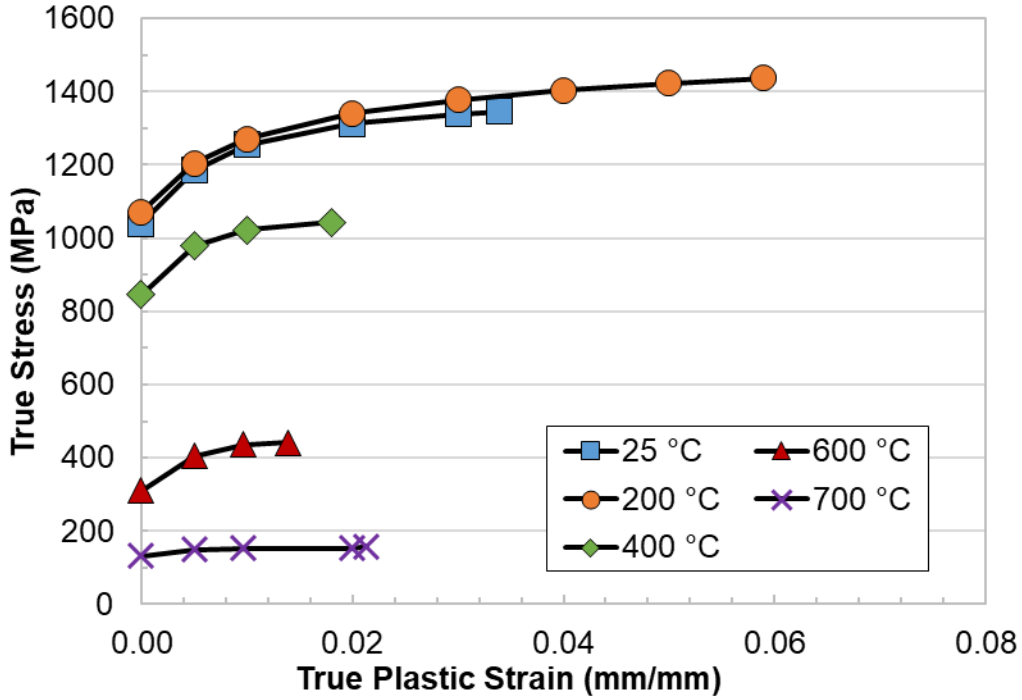

Figure 35. Flow stress behavior at various temperatures for HY-80 steel after cooling at 10 °C/s (18 °F/s) from a peak temperature of 1350 °C (2462 °F). Terminal data points are at the UTS.

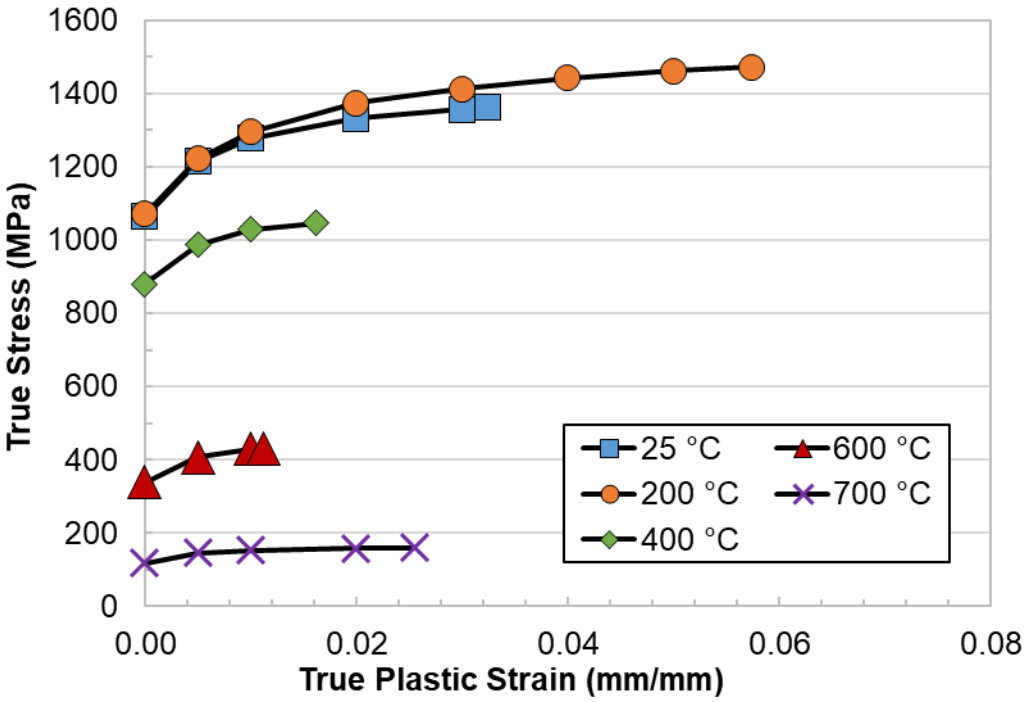

Figure 36. Flow stress behavior at various temperatures for HY-80 steel after cooling at 25 °C/s (45 °F/s) from a peak temperature of 1350 °C (2462 °F). Terminal data points are at the UTS.

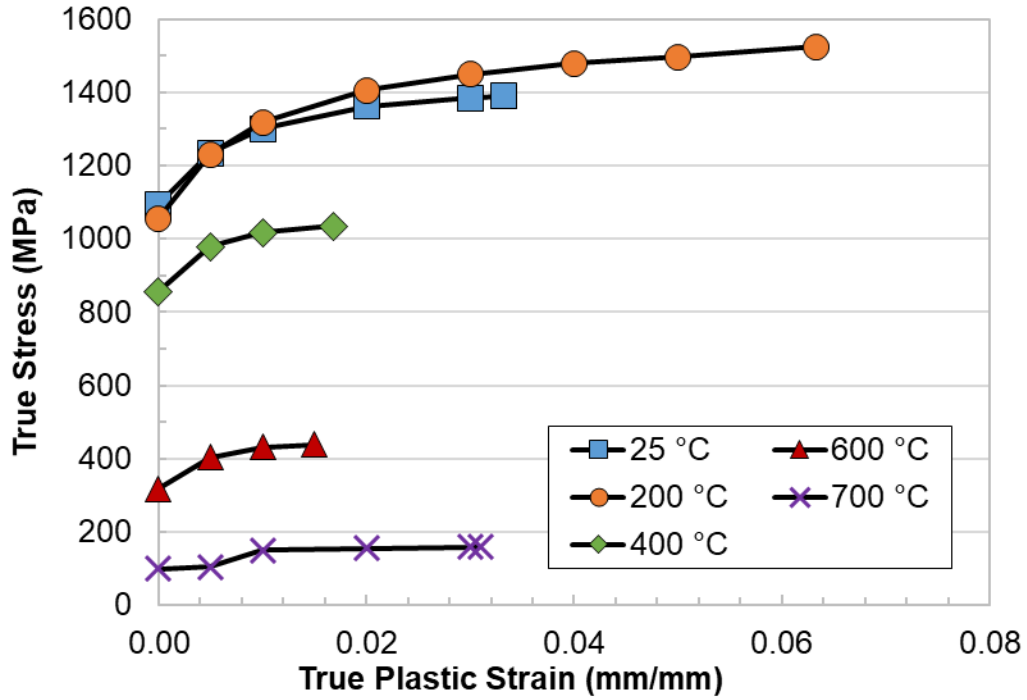

Figure 37. Flow stress behavior at various temperatures for HY-80 steel after cooling at 100 °C/s (180 °F/s) from a peak temperature of 1350 °C (2462 °F). Terminal data points are at the UTS.

CONCLUSIONS

Temperature-dependent material property data of a pedigreed plate of HY-80 steel from room temperature up to nearly the steel's melting point were determined. The thermo-physical properties investigated include specific heat, thermal diffusivity, thermal conductivity, CTE, and density. Thermo-mechanical properties including yield strength, UTS, and flow stress were also measured. The temperatures associated with on-heating and on-cooling phase transformations and their variation with heating rate, cooling rate, and peak temperature were determined and used to develop welding-focused CCT diagrams. Investigation of HAZ microstructures from the CCT specimens and arc welds concluded the analysis. This effort is essential for increasing the fidelity of finite element models used to predict welding-induced distortion and residual stress in marine structures. The data generated in this program have been provided to ESI for immediate incorporation into their *SYSWELD* software. A machine-readable version of the collected data will be uploaded to the University of Michigan's *Materials Commons* data repository <https://materialscommons.org> at a later date.

APPENDIX

Appendix A: Plate Conformance Certificate and Chemical Composition for HY-80

ArcelorMittal

TEST CERTIFICATE

ARCELORMITTAL PLATE LLC

PAGE NO: 01 OF 03
FILE NO: 2822-01-02
MILL ORDER NO: 83502-001
MELT NO: D2504
SLAB NO: 2FH
DATE: 02/19/18

SHIP TO:
RONSON TECHNICAL PRODUCTS
C/O HUDSON METAL PROCESSING
1500 NATIONAL CEMETERY ROAD
FLORENCE SC 29506

SOLD TO:
ENERGY & PROCESS CORPORATION
A FERGUSON ENTERPRISE
P.O. BOX 125
TUCKER GA 30085-0125

SEND TO:

01-C

STEEL PLATE DIMENSIONS / DESCRIPTION

TOTAL QTY	GAUGE	WIDTH	LENGTH	DESCRIPTION	PIECE WEIGHT
1	3/16"	96"	240"	RECTANGLE	1225#

CUSTOMER INFORMATION

CUSTOMER PO: R257-210 ADD# 1

PART NO. HY80316N

SPECIFICATION(S)

THIS MATERIAL HAS BEEN MANUFACTURED AND TESTED IN ACCORDANCE WITH PURCHASE ORDER REQUIREMENTS AND SPECIFICATION(S).

NAVSE TECH-PUB-T9074 REV 2 YR 12 HY80-TY.I
T9074-BD-GIB-010/0300 REV O WITH ACN #1 DTD
12/11/02 GR.HY80 TYPE I AND MIL-S-16216K(SH) 87
GR.HY80 TYPE I
NAVSEA TECHNICAL PUBLICATION T9074-BD-GIB-010/0300
REVISION 2 DATED 12/18/12 HY80
THE MANAGEMENT SYSTEMS FOR MANUFACTURE OF THIS PRODUCT ARE CERTIFIED TO ISO 9001:2008 (CERTIFICATE NO. 30130) AND ISO 14001:2004 (CERTIFICATE NO. 49009).

CHEMICAL COMPOSITION (WT%) FOR ALL ELEMENTS EXCEPT H (PPM)

	C	MN	P	S	CU	SI	NI	CR	MO
MELT:D2504	.13	.26	.005	.002	.15	.32	2.15	1.17	.23
PROD ANALYSIS	.12	.27	.005	.002	.14	.33	2.05	1.17	.22

	V	TI	AL	CB	SB	AS	SN	LOC
MELT:D2504	.004	.003	.021	.001	.0010	.0030	.009	
PROD ANALYSIS	.002	.001	.019	.001	.0010	.0030	.010	BOT

MANUFACTURE

ELECTRIC FURNACE QUALITY - FINELINE - VACUUM DEGASSED - FINE GRAIN PRACTICE

WE HEREBY CERTIFY THE ABOVE INFORMATION IS CORRECT:

ARCELORMITTAL PLATE LLC
QUALITY ASSURANCE LABORATORY
139 MODENA ROAD
COATESVILLE, PA 19320

SUPERVISOR – TEST REPORTING
LOC TRAN

TEST CERTIFICATE

PAGE NO: 02 OF 03
FILE NO: 2822-01-02
MILL ORDER NO: 83502-001
MELT NO: D2504
SLAB NO: 2FH
DATE: 02/19/18

HEAT TREAT CONDITION

MATL OR TEST	HEAT TREAT DESCRIPTION	NOM TEMP	HOLD MINS	COOL MTHD
PL/TEST	HARDEN	1660F	14	W.QUENCH
PL/TEST	TEMPER	1280F	26	AIR COOL

TENSILE PROPERTIES

SLAB NO.	LOC	DIR	YIELD STRENGTH PSI X 1000	TENSILE STRENGTH PSI X 1000	ELONGATION AFTER FRACTURE GAGE LGTH	%
2FH	BOT.	TRANS.	97	106	2.00"	21.0
2FH	TOP	TRANS.	96	105	2.00"	25.0

WE HEREBY CERTIFY THE ABOVE INFORMATION IS CORRECT:

ARCELORMITTAL PLATE LLC
QUALITY ASSURANCE LABORATORY
139 MODENA ROAD
COATESVILLE, PA 19320

SUPERVISOR – TEST REPORTING
LOC TRAN

T E S T C E R T I F I C A T E
PAGE NO: 03 OF 03
FILE NO: 2822-01-02
MILL ORDER NO: 83502-001
MELT NO: D2504
SLAB NO: 2FH
DATE: 02/19/18

G E N E R A L I N F O R M A T I O N

ALL STEEL HAS BEEN MELTED AND MANUFACTURED IN THE U.S.A.
PRODUCED IN ACCORDANCE WITH INSPECTION SYSTEM
REQUIREMENTS OF MIL-I-45208A AMEND #1.
A.B.S. CERTIFICATE QA 2799196-A
A.B.S. CERTIFICATE QA 2799196-B
MATERIAL HAS BEEN VACUUM DEGASSED AND CALCIUM TREATED
FOR SULFIDE SHAPE CONTROL. FINELINE MOD FOR SULPHUR
THE TEST RESULTS SHOWN IN THIS REPORT ARE THE
RESULTS OF TESTING PERFORMED BY OUR ORGANIZATION.
ALL STEEL HAS BEEN MANUFACTURED IN THE U.S.A.
NO WELD REPAIR PERFORMED BY ARCELORMITTAL PLATE LLC.
MERCURY OR MERCURY COMPOUNDS ARE NOT USED IN THE MANUFACTURE
OF ARCELORMITTAL PLATE LLC PRODUCTS.
ACID SOLUBLE ALUMINUM
FOR MORE INFORMATION AND PROCESSING GUIDELINES, REFER TO
WWW.USA.ARCELORMITTAL.COM/PLATE

NDT, VISUAL AND DIMENSIONAL INSPECTION AS REQUIRED BY THE SPECIFICATION WAS SATISFACTORILY PERFORMED.

MATERIAL HAS BEEN SAMPLED, TESTED, AND INSPECTED IN ACCORDANCE WITH THE SPECIFICATION REQUIREMENTS. THE MANUFACTURER HAS MAINTAINED MANUFACTURING PROCEDURES AND PRACTICES WHICH PRODUCE PLATES WHICH MEET THE MINIMUM PROPERTY REQUIREMENTS THROUGHOUT THE PLATE. THE MATERIAL MEETS ALL SPECIFICATION REQUIREMENTS.

RECORDS ARE AVAILABLE COVERING HEAT NUMBER OF THE MATERIAL USED, PROCESSING OF PLATE, DIMENSIONAL CONTROL EMPLOYED AND HEAT TREATMENT.

LOW MELTING ALLOYS/LOW MELTING COMPOUNDS ARE NOT USED IN THE MFG. OF ARCELORMITTAL PLATE LLC PRODUCTS OTHER THAN AS DEOXIDIZING AGENTS.

KNOWINGLY AND WILLFULLY FALSIFYING OR CONCEALING A MATERIAL FACT ON THIS FORM, OR MAKING FALSE, FICTITIOUS OR FRAUDULENT ENTRIES OR REPRESENTATIONS HEREIN, COULD CONSTITUTE A FELONY PUNISHABLE UNDER FEDERAL STATUTES.

CERTIFICATE OF CONFORMANCE - ALL ITEMS FURNISHED IN THE SHIPMENT ARE IN FULL CONFORMANCE WITH ALL P.O. AND SPEC. REQ.; AND THAT THE T.R.'S REPRESENT THE ACTUAL ATTRIBUTES OF THE ITEMS FURNISHED ON THE ORDER, AND THAT THE TEST RESULTS ARE IN FULL CONFORMANCE WITH ALL P.O. & SPEC. REQ. RECORDS TO SUBSTANTIATE THE ABOVE ARE ON FILE IN

OUR PLANT AND WILL BE MAINTAINED FOR A PERIOD OF 7 YRS. FROM THE DATE OF THE SHIPMENT UNLESS FURNISHED TO THE PURCHASER IN ADVANCE OF OR AT TIME OF SHIPMENT. WHEN RECORDS ARE RETAINED BY US, WE AGREE TO FURNISH SAME TO THE PURCHASER AT ANY TIME DURING THE ABOVE PERIOD UPON REQUEST.

HEAT TREAT PROC. NO. MIL-STD-1684D

B/L #28642 CUSTOMER'S TRUCK

WE HEREBY CERTIFY THE ABOVE
INFORMATION IS CORRECT:

ARCELORMITTAL PLATE LLC
QUALITY ASSURANCE LABORATORY
139 MODENA ROAD
COATESVILLE, PA 19320

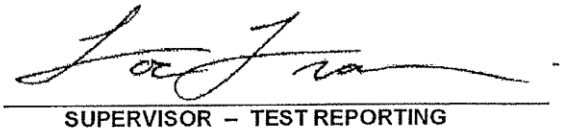

SUPERVISOR – TEST REPORTING
LOC TRAN

Table 8. Chemical Composition of HY-80 Base Plate as Measured by OSU

Element	Wt	Test 1	Test 2	Test 3	Average
C	%	0.13	0.099	0.080	0.103
Si	%	0.33	0.33	0.33	0.33
Mn	%	0.26	0.26	0.26	0.26
P	%	0.003	0.003	0.003	0.003
S	%	<0.0005	<0.0005	0.0006	<0.0005
Cr	%	1.19	1.19	1.19	1.19
Mo	%	0.23	0.23	0.23	0.23
Ni	%	2.56	2.56	2.55	2.56
Al	%	0.023	0.024	0.023	0.023
Co	%	0.002	0.003	0.003	0.003
Cu	%	0.14	0.15	0.15	0.15
Nb	%	0.001	0.001	0.001	0.001
Ti	%	0.002	0.002	0.002	0.002
V	%	0.004	0.004	0.004	0.004
W	%	<0.005	<0.005	<0.005	<0.005
Pb	%	<0.0010	<0.0010	<0.0010	<0.0010
Sn	%	0.011	0.012	0.012	0.012
As	%	0.006	0.008	0.006	0.007
Zr	%	<0.0010	<0.0010	<0.0010	<0.0010
Ca	%	0.002	0.003	0.002	0.002
Ce	%	<0.0010	<0.0010	<0.0010	<0.0010
Sb	%	0.007	0.009	0.008	0.008
Se	%	0.003	0.003	0.003	0.003
Te	%	0.014	0.014	0.014	0.014
Ta	%	<0.007	<0.007	<0.007	<0.007
B	%	0.001	0.001	0.001	0.001
Zn	%	0.001	0.003	0.001	0.002
La	%	<0.0003	<0.0003	<0.0003	<0.0003

Table 9. Chemical Composition of HY-80 Base Plate as Measured by NSWCCD. Reported carbon and sulfur values were measured separately via combustion analysis.

Element	Wt	Test 1	Test 2	Test 3	Test 4	Average
C	%	0.135	0.139	0.136	0.138	0.1374
Si	%	0.329	0.322	0.328	0.315	0.3235
Mn	%	0.245	0.245	0.254	0.246	0.2478
P	%	0.004	0.004	0.004	0.003	0.004
S	%	0.00387	0.00373	0.00365	0.00372	0.00375
Cr	%	1.19	1.20	1.21	1.20	1.20
Mo	%	0.193	0.194	0.201	0.194	0.196
Ni	%	2.05	2.05	2.12	2.05	2.07
Al	%	0.025	0.025	0.025	0.025	0.025
Co	%	0.0089	0.0078	0.0064	0.0056	0.0071
Cu	%	0.134	0.134	0.139	0.133	0.135
Nb	%	<0.003	<0.003	<0.003	<0.003	<0.003
Ti	%	<0.001	<0.001	<0.001	<0.001	<0.001
V	%	0.0064	<0.003	<0.003	<0.003	<0.003
Sn	%	<0.005	<0.005	<0.005	<0.005	<0.005
Zr	%	<0.01	<0.01	<0.01	<0.01	<0.01
Ca	%	0.0032	0.0025	0.0028	0.0030	0.0029
Ta	%	0.178	0.130	0.110	0.113	0.133
B	%	<0.0004	<0.0004	<0.0004	<0.0004	<0.0004

Appendix B: Continuous Cooling Transformation Curves

Table 10. Austenite Transformation Temperatures as Illustrated in **Figure 8**

Heating Rate (°C/s)	A_{c1} (°C)	A_{c3} (°C)
10	767	892
100	767	832
200	762	827
500	786	872
1000	767	827
2000	755	812

Table 11. Experimentally Measured On-Cooling Transformation Temperatures for HY-80 Dilatometry Specimens Cooled from 785 °C (1445 °F). Note: Colors correspond to the transformation products discussed in **Figures 9-15**.

Cooling Rate (°C/s) [°F/s]	1 [1.8]	5 [9]	10 [18]	25 [45]	100 [180]	200 [360]
Transformation Temperature (°C) [°F]	724 [1335]	666 [1231]	713 [1315]	561 [1042]	544 [1011]	425 [797]
	626 [1159]	580 [1076]	656 [1213]	395 [743]	422 [792]	274 [525]
		415 [779]		319 [606]	296 [565]	

Table 12. Experimentally Measured On-Cooling Transformation Temperatures for HY-80 Dilatometry Specimens Cooled from 1000 °C (1832 °F). Note: Colors correspond to the transformation products discussed in **Figures 9-15**.

Cooling Rate (°C/s) [°F/s]	1 [1.8]	5 [9]	10 [18]	25 [45]	100 [180]	200 [360]
Transformation Temperature (°C) [°F]	570 [1058]	571 [1060]	518 [964]	540 [1004]	423 [793]	420 [788]
	395 [743]	384 [723]	389 [732]	413 [775]	273 [523]	272 [522]
		317 [603]	283 [541]	285 [545]		

Table 13. Experimentally Measured On-Cooling Transformation Temperatures for HY-80 Dilatometry Specimens Cooled from 1150 °C (2102 °F). Note: Colors correspond to the transformation products discussed in **Figures 9-15**.

Cooling Rate (°C/s) [°F/s]	1 [1.8]	5 [9]	10 [18]	25 [45]	100 [180]	200 [360]
Transformation Temperature (°C) [°F]	570 [1058]	544 [1011]	490 [914]	430 [806]	440 [824]	429 [804]
	406 [763]	450 [842]	420 [788]	270 [518]	280 [536]	277 [531]
		340 [644]	290 [554]			

Table 14. Experimentally Measured On-Cooling Transformation Temperatures for HY-80 Dilatometry Specimens Cooled from 1350 °C (2462 °F). Note: Colors correspond to the transformation products discussed in **Figures 9-15**.

Cooling Rate (°C/s) [°F/s]	1 [1.8]	5 [9]	10 [18]	25 [45]	100 [180]	200 [360]
Transformation Temperature (°C) [°F]	593 [1099]	549 [1020]	570 [1058]	450 [842]	455 [851]	458 [856]
	406 [763]	400 [752]	359 [678]	283 [541]	275 [527]	276 [529]
		328 [622]	306 [583]			

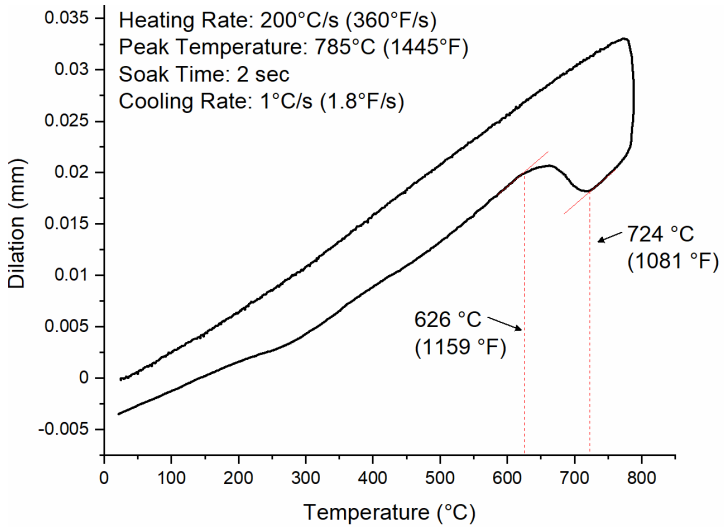

Figure 38. Dilation curve from a HY-80 Gleeble sample heated to a peak temperature of 785 °C and cooled at 1 °C/s.

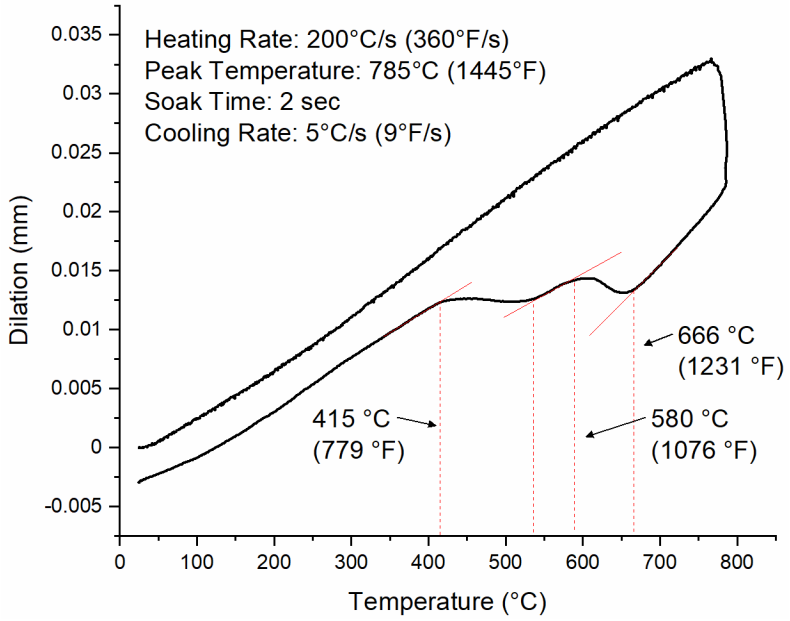

Figure 39. Dilation curve from a HY-80 Gleeble sample heated to a peak temperature of 785 °C and cooled at 5 °C/s.

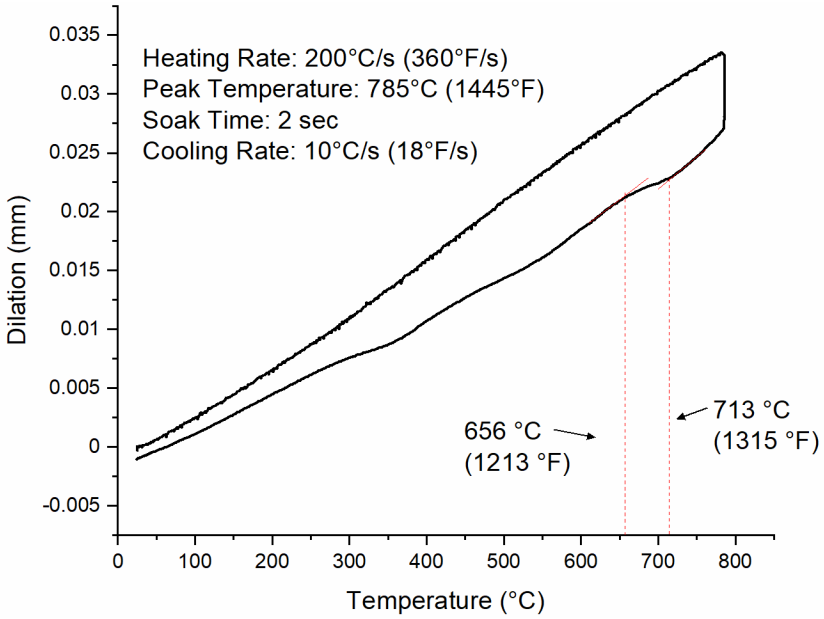

Figure 40. Dilation curve from a HY-80 Gleeble sample heated to a peak temperature of 785 °C and cooled at 10 °C/s.

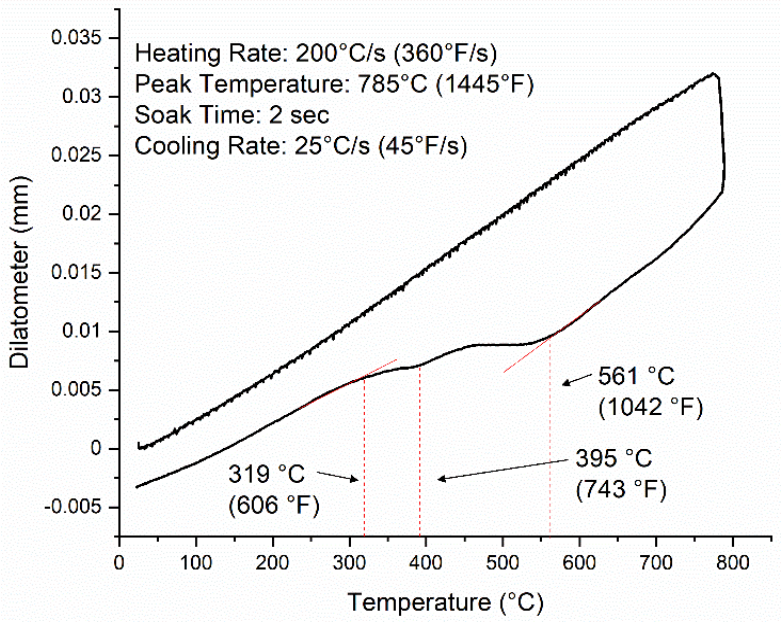

Figure 41. Dilation curve from a HY-80 Gleeble sample heated to a peak temperature of 785 °C and cooled at 25 °C/s.

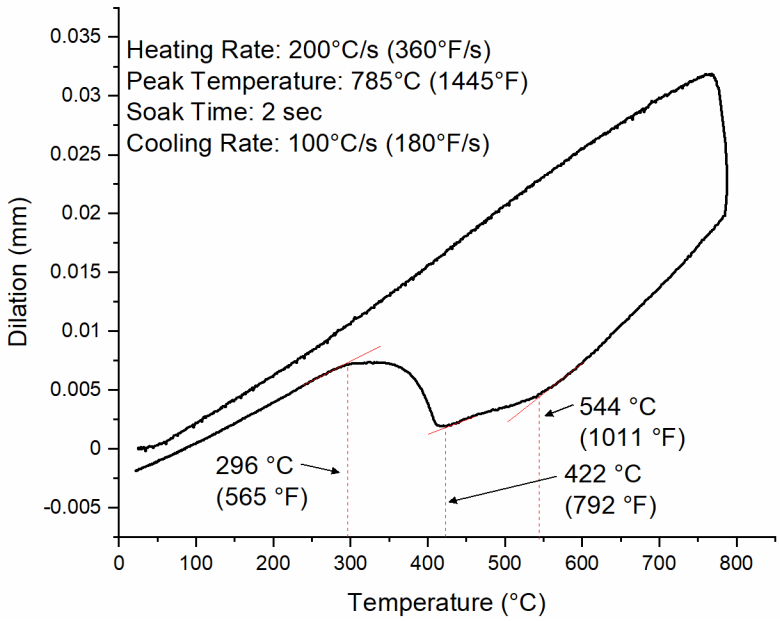

Figure 42. Dilation curve from a HY-80 Gleeble sample heated to a peak temperature of 785 °C and cooled at 100 °C/s.

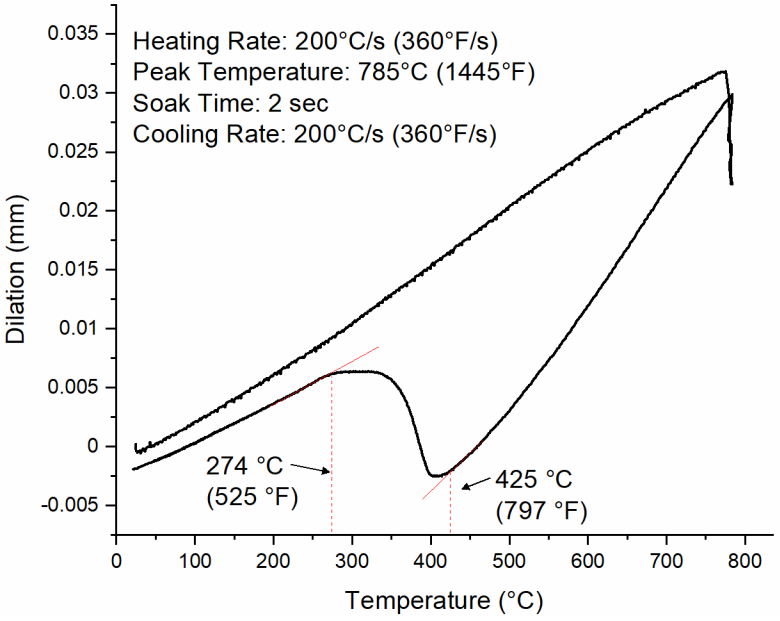

Figure 43. Dilation curve from a HY-80 Gleeble sample heated to a peak temperature of 785 °C and cooled at 200 °C/s.

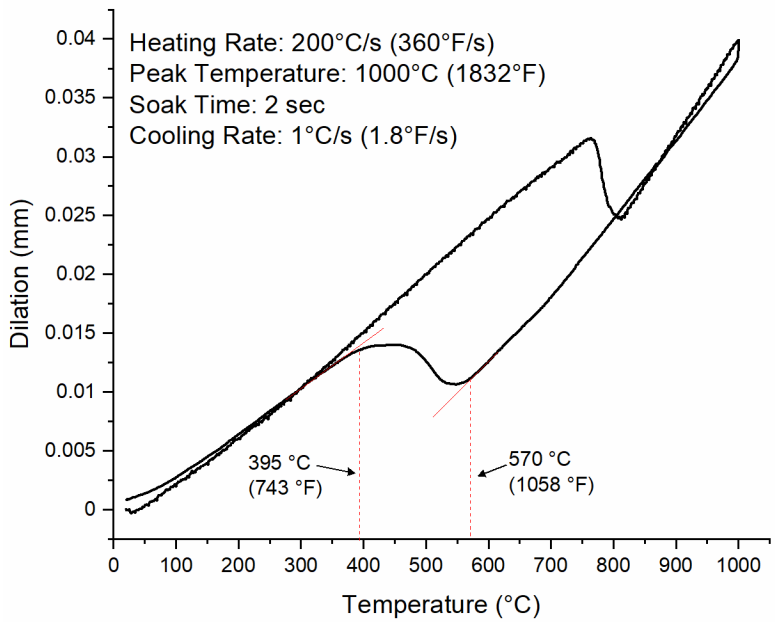

Figure 44. Dilation curve from a HY-80 Gleeble sample heated to a peak temperature of 1000 °C and cooled at 1 °C/s.

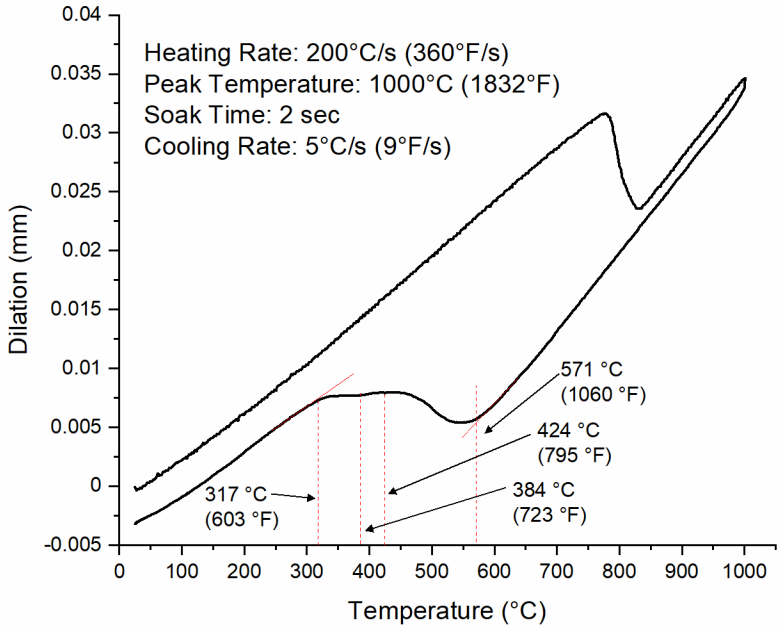

Figure 45. Dilation curve from a HY-80 Gleeble sample heated to a peak temperature of 1000 °C and cooled at 5 °C/s.

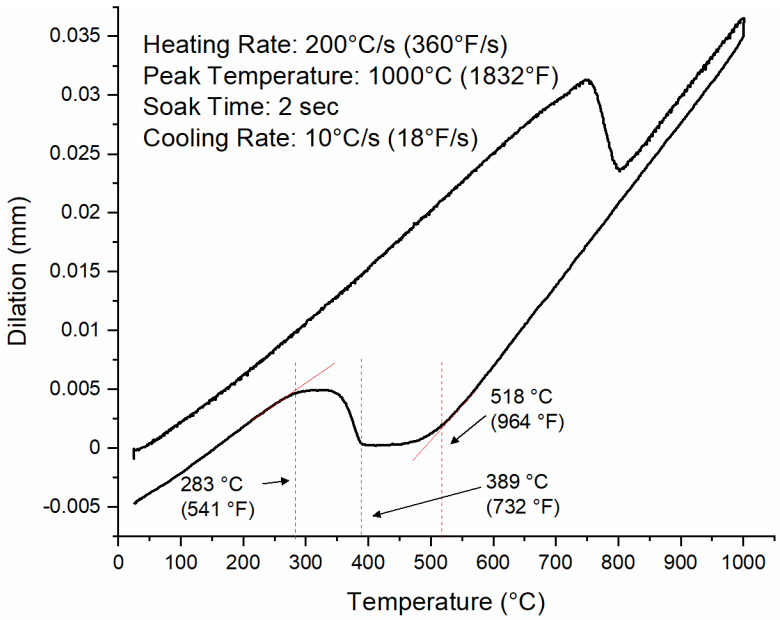

Figure 46. Dilation curve from HY-80 Gleeble sample heated to a peak temperature of 1000 °C and cooled at 10 °C/s.

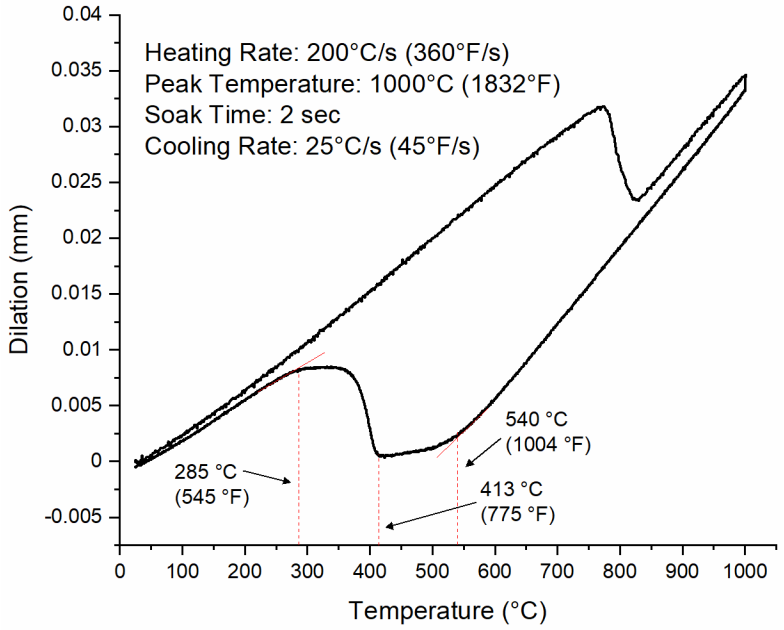

Figure 47. Dilation curve from a HY-80 Gleeble sample heated to a peak temperature of 1000 °C and cooled at 25 °C/s.

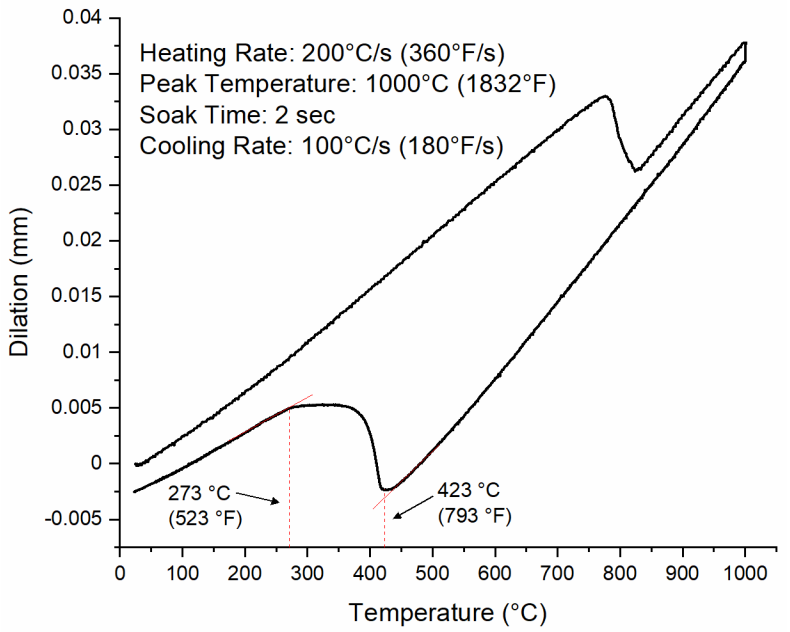

Figure 48. Dilation curve from a HY-80 Gleeble sample heated to a peak temperature of 1000 °C and cooled at 100 °C/s.

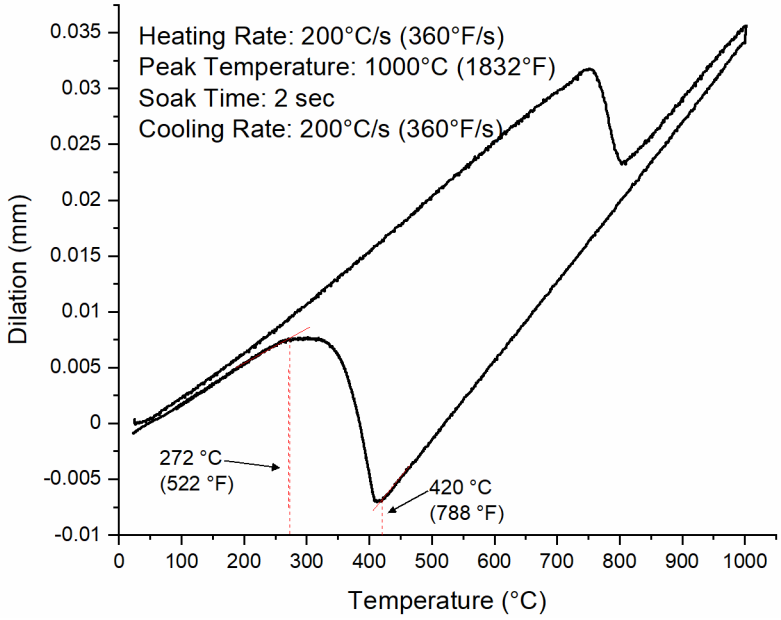

Figure 49. Dilation curve from a HY-80 Gleeble sample heated to a peak temperature of 1000 °C and cooled at 200 °C/s.

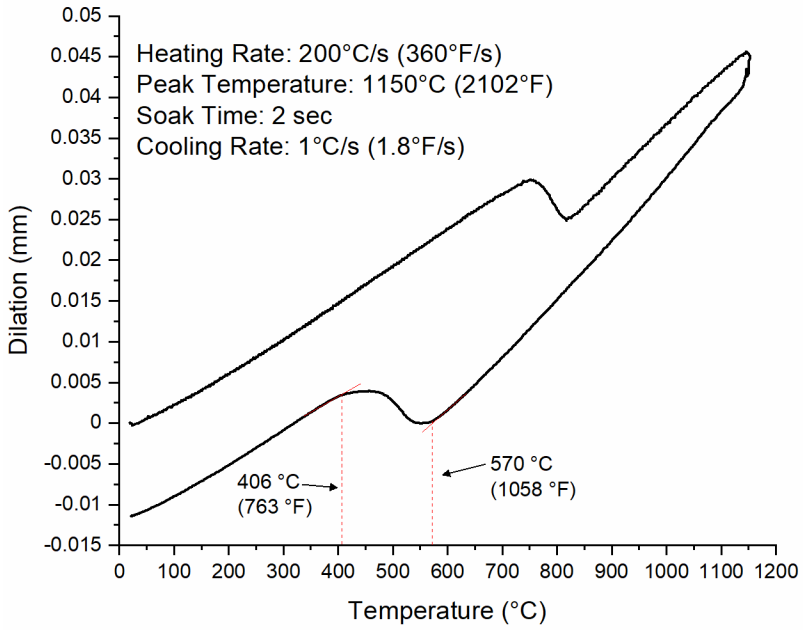

Figure 50. Dilation curve from a HY-80 Gleeble sample heated to a peak temperature of 1150 °C and cooled at 1 °C/s.

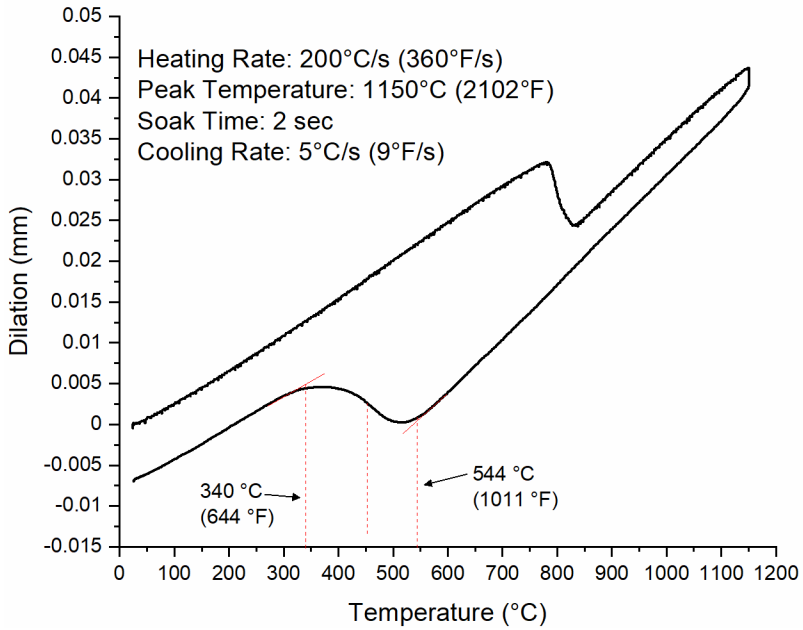

Figure 51. Dilation curve from a HY-80 Gleeble sample heated to a peak temperature of 1150 °C and cooled at 5 °C/s.

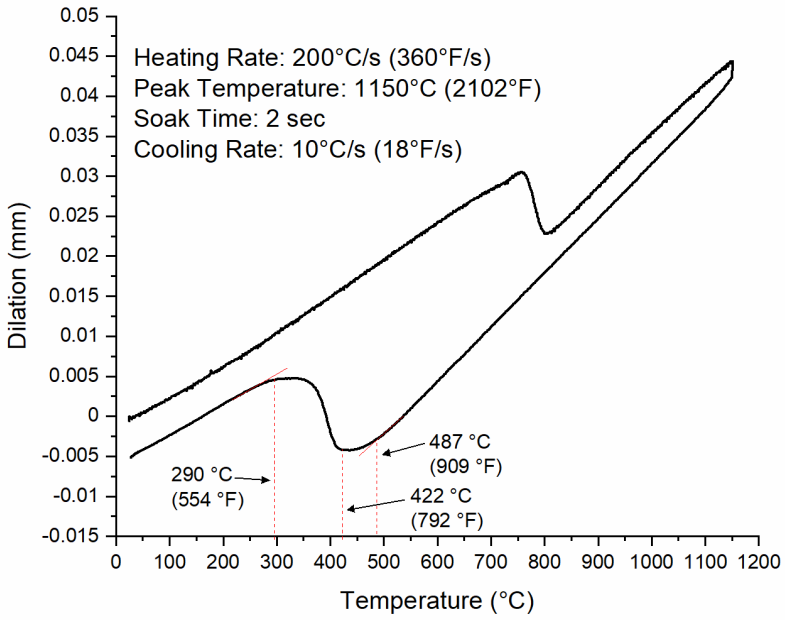

Figure 52. Dilation curve from a HY-80 Gleeble sample heated to a peak temperature of 1150 °C and cooled at 10 °C/s.

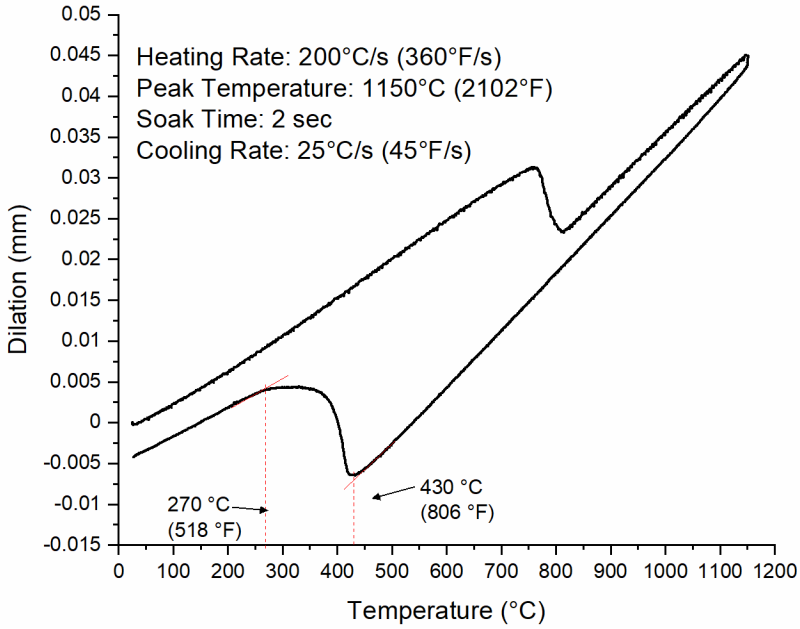

Figure 53. Dilation curve from a HY-80 Gleeble sample heated to a peak temperature of 1150 °C and cooled at 25 °C/s.

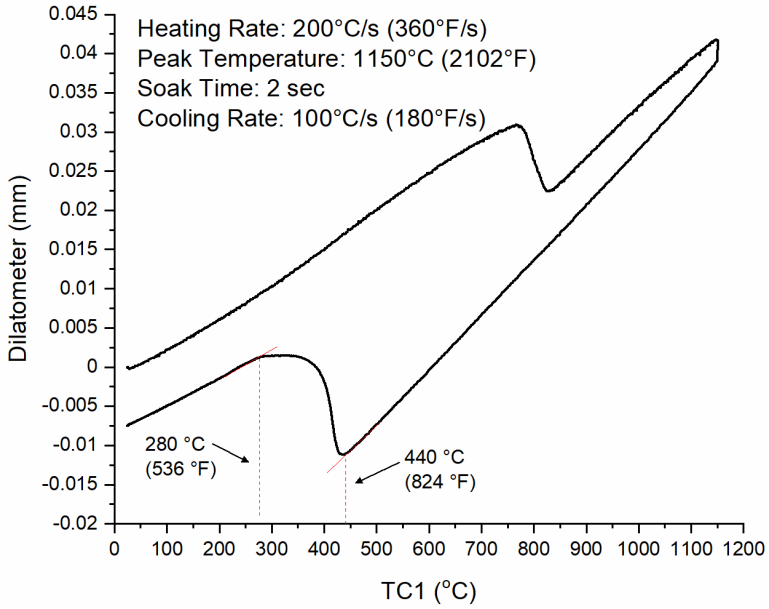

Figure 54. Dilation curve from a HY-80 Gleeble sample heated to a peak temperature of 1150 °C and cooled at 100 °C/s.

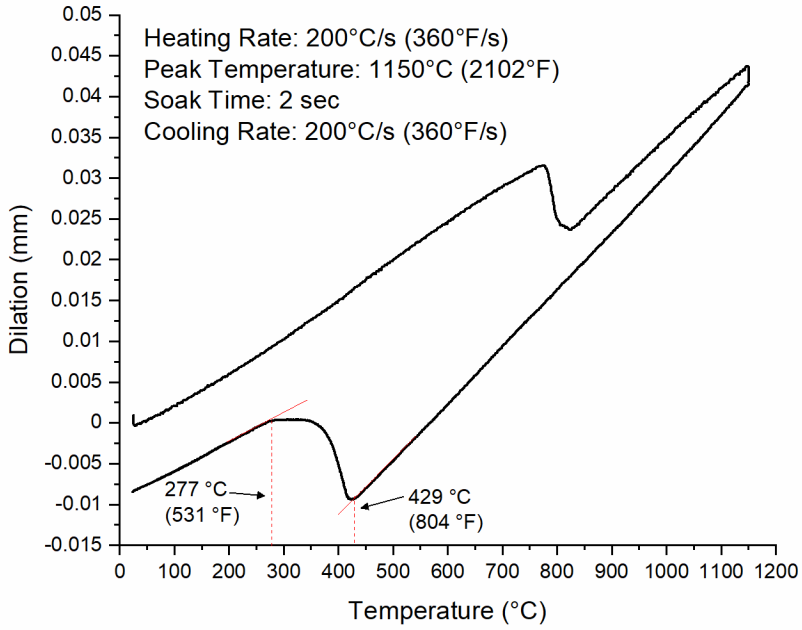

Figure 55. Dilation curve from a HY-80 Gleeble sample heated to a peak temperature of 1150 °C and cooled at 200 °C/s.

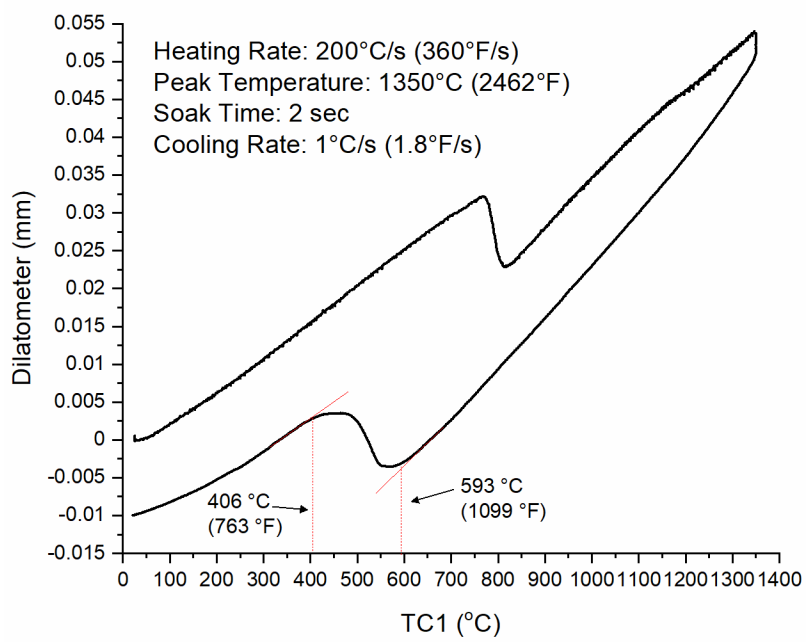

Figure 56. Dilation curve from a HY-80 Gleeble sample heated to a peak temperature of 1350 °C and cooled at 1 °C/s.

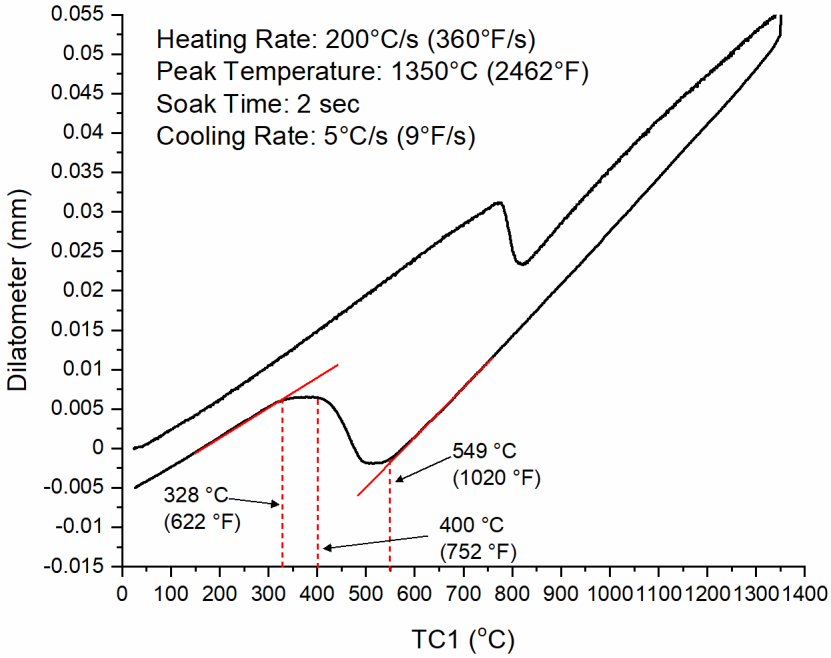

Figure 57. Dilation curve from a HY-80 Gleeble sample heated to a peak temperature of 1350 °C and cooled at 5 °C/s.

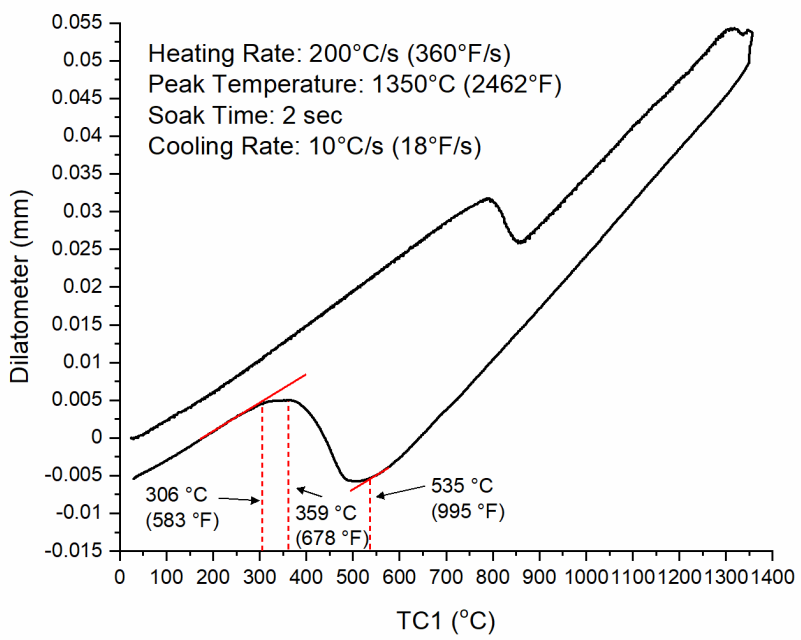

Figure 58. Dilation curve from a HY-80 Gleeble sample heated to a peak temperature of 1350 °C and cooled at 10 °C/s.

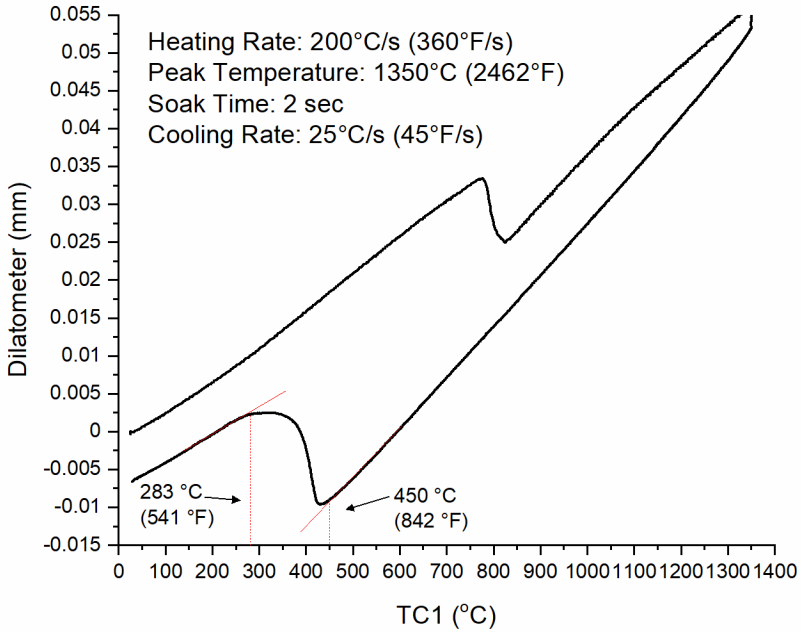

Figure 59. Dilation curve from a HY-80 Gleeble sample heated to a peak temperature of 1350 °C and cooled at 25 °C/s.

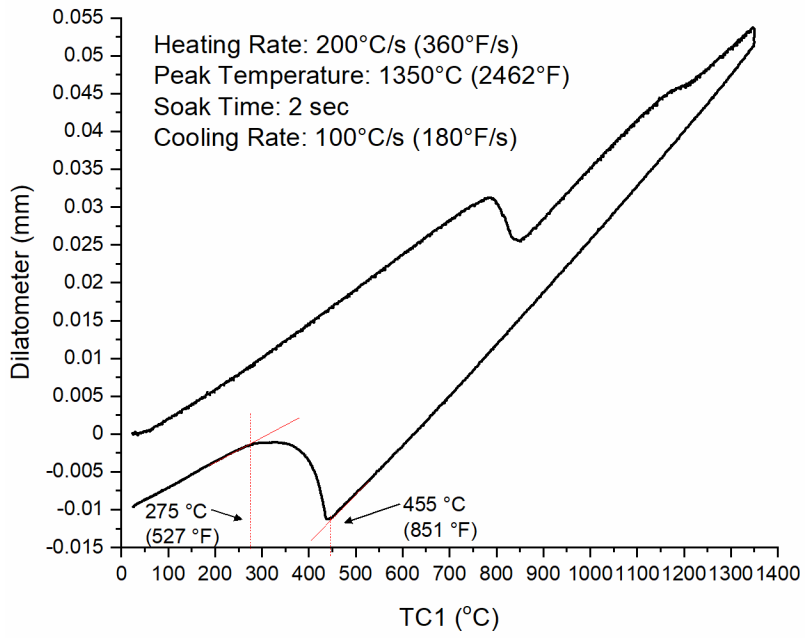

Figure 60. Dilation curve from a HY-80 Gleeble sample heated to a peak temperature of 1350 °C and cooled at 100 °C/s.

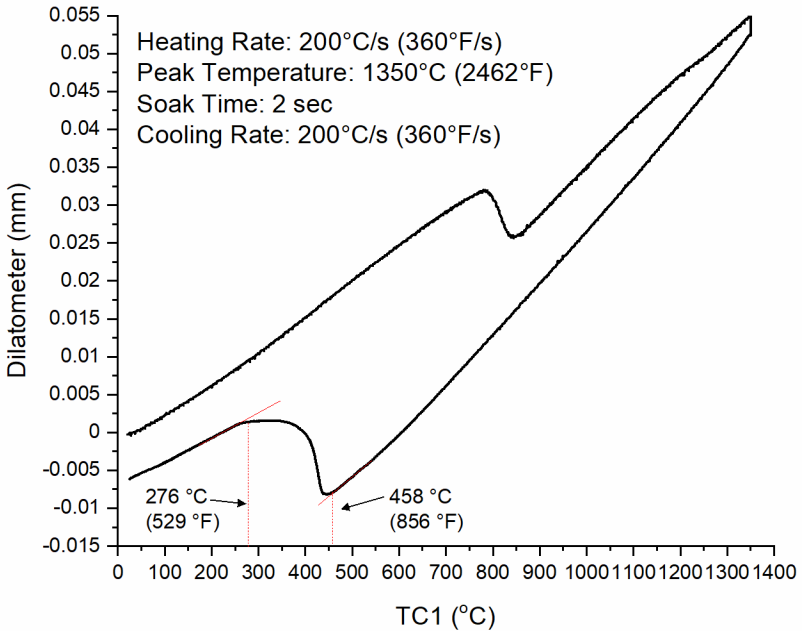

Figure 61. Dilation curve from a HY-80 Gleeble sample heated to a peak temperature of 1350 °C and cooled at 200 °C/s.

Appendix C: Representative Microstructures of HY-80 CCT Specimens

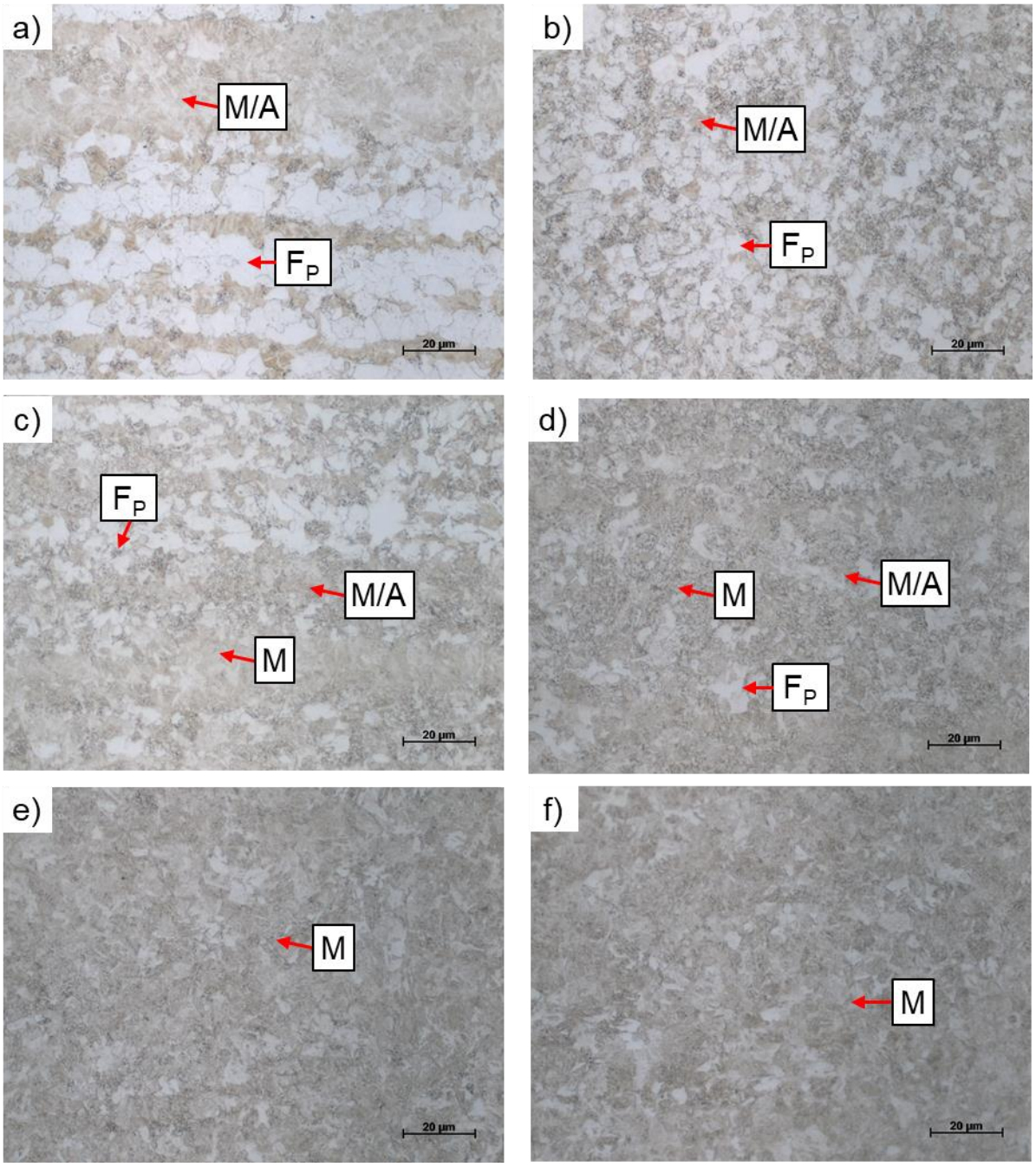

Figure 62. Representative microstructures from HY-80 dilatometry specimens heated to a peak temperature of 785 °C (1445 °F) and continuously cooled at various rates. **(a-f)**: 1, 5, 10, 25, 100, and 200 °C/s (1.8, 9, 18, 45, 180, and 360 °F/s).

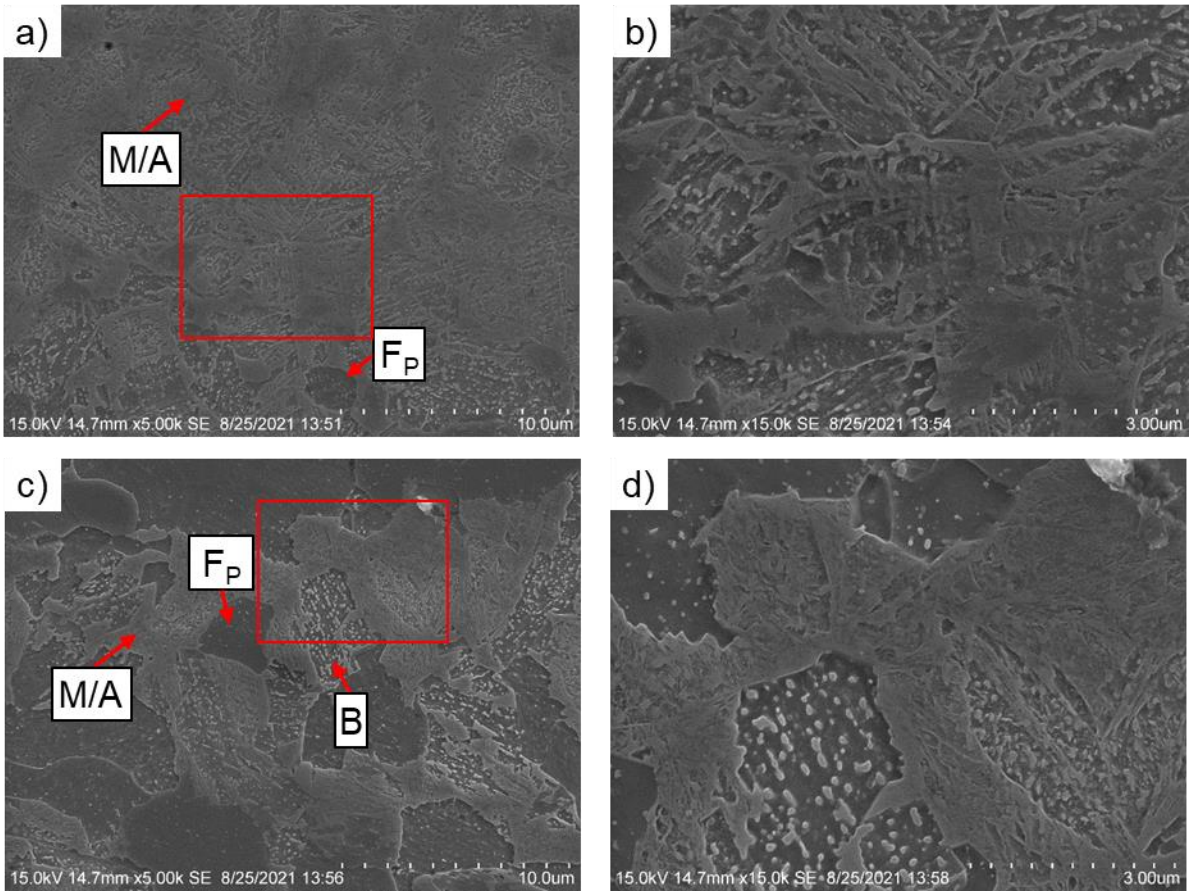

Figure 63. SEM images showing representative microstructures of HY-80 dilatometry specimens heated to a peak temperature of 785 °C (1445 °F) and continuously cooled at 1 °C/s (1.8 °F/s). Images are shown **a-b)** in the thick tan-etched band along the sample centerline, and **c-d)** in a thin tan-etched band located approximately a quarter into the sample thickness. Red boxes identify the location of the corresponding higher magnification images (**b** and **d).**

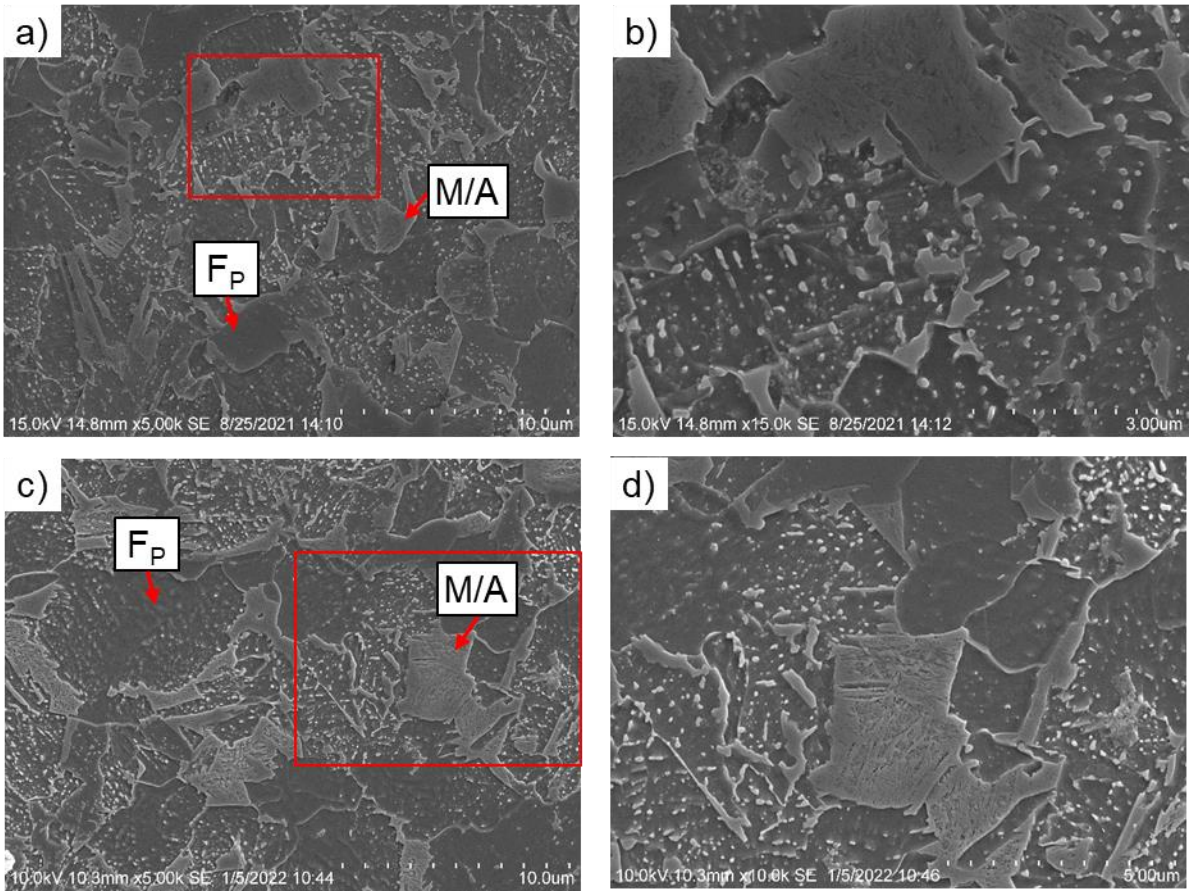

Figure 64. SEM images showing representative microstructures of HY-80 dilatometry specimens heated to a peak temperature of 785 °C (1445 °F) and continuously cooled at **a-b)** 5 °C/s (9 °F/s) and **c-d)** 10 °C/s (18 °C/s). Note that magnification for images **b)** and **d)** are not the same. Red boxes identify the location of the corresponding higher magnification images (**b** and **d).**

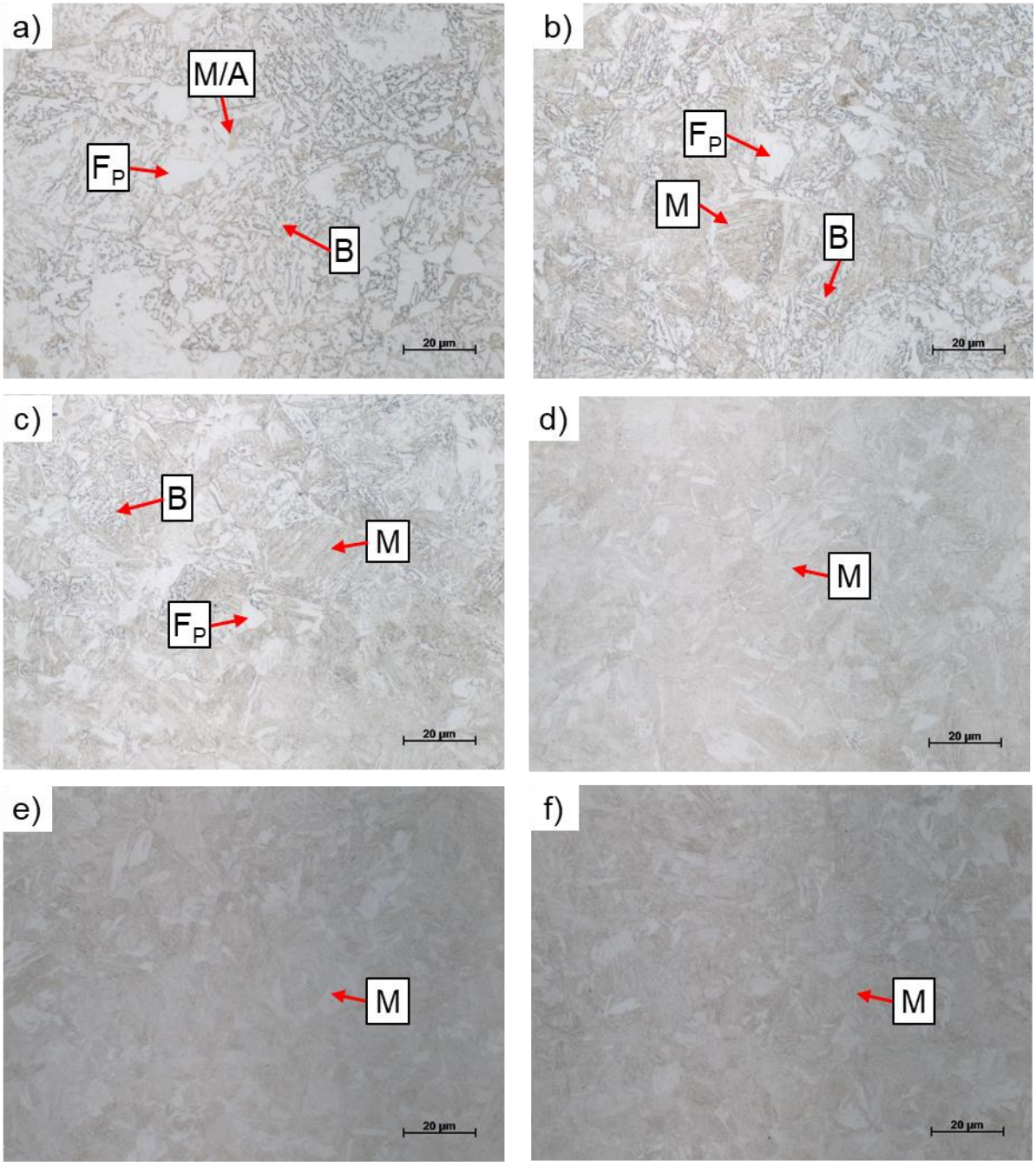

Figure 65. Representative microstructures from HY-80 dilatometry specimen heated to a peak temperature of 1000 °C (1832 °F) and continuously cooled at various rates. **(a-f)**: 1, 5, 10, 25, 100, and 200 °C/s (1.8, 9, 18, 45, 180, and 360 °F/s).

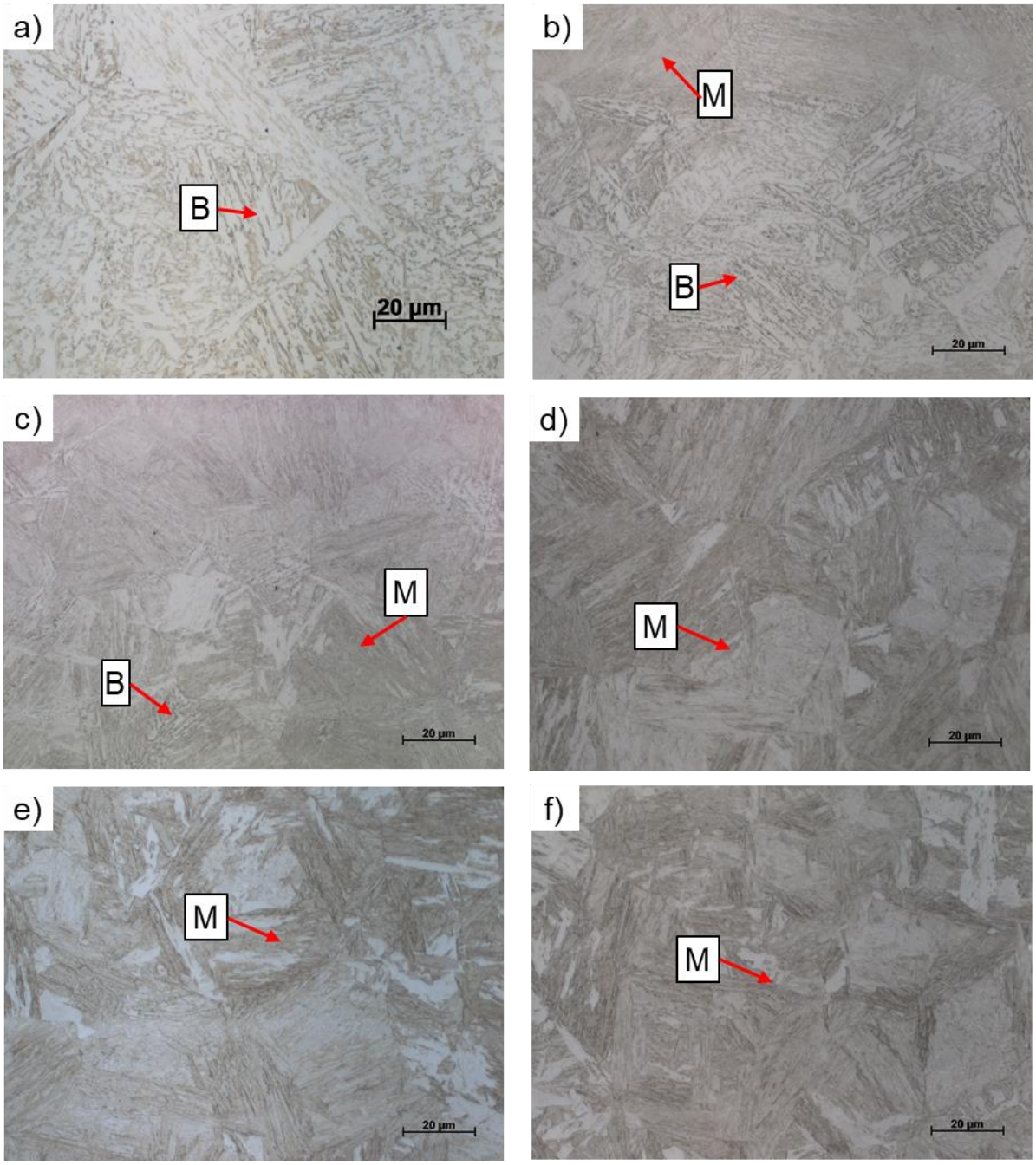

Figure 66. Representative microstructures from HY-80 dilatometry specimens heated to a peak temperature of 1150 °C (2102 °F) and continuously cooled at various rates. **(a-f)**: 1, 5, 10, 25, 100, and 200 °C/s (1.8, 9, 18, 45, 180, and 360 °F/s).

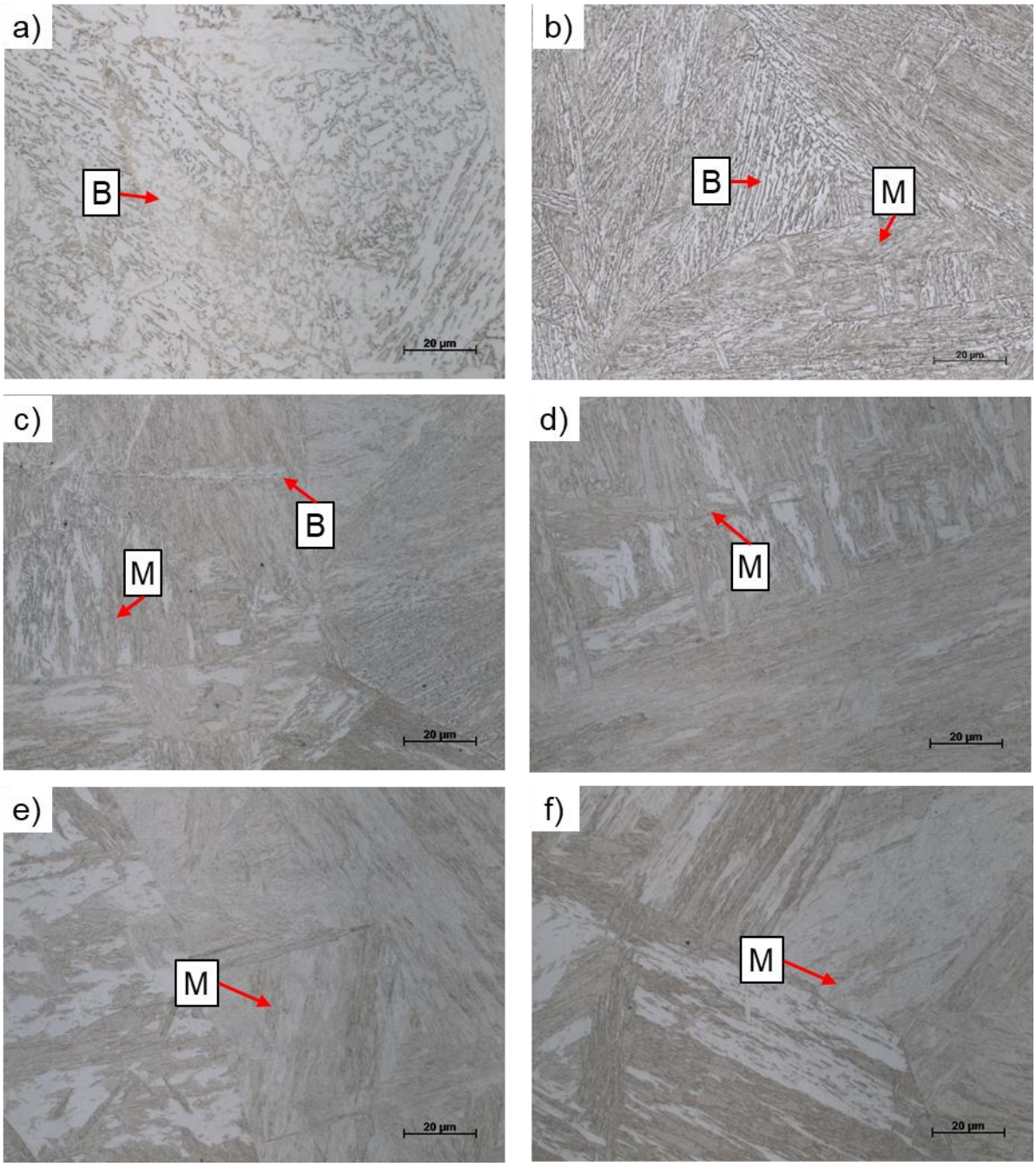

Figure 67. Representative microstructures from HY-80 dilatometry specimens heated to a peak temperature of 1350 °C (2462 °F) and continuously cooled at various rates. **(a-f)**: 1, 5, 10, 25, 100, and 200 °C/s (1.8, 9, 18, 45, 180, and 360 °F/s).

Appendix D: Microhardness Measurements

Table 15. Vickers Microhardness of HY-80 as a Function of Peak Temperature and Cooling Rate. Note: Errors are one standard deviation and values in parenthesis are the number of indents measured.

Cooling Rate		Peak Temperature				
		°C	785	1000	1150	1350
°C/s	°F/s	°F	1445	1832	2102	2462
1	1.8	242 ± 22 (42)		263 ± 18 (42)	267 ± 15 (42)	251 ± 15 (42)
5	9	272 ± 15 (42)		303 ± 34 (42)	329 ± 29 (42)	325 ± 30 (42)
10	18	281 ± 15 (42)		357 ± 32 (42)	378 ± 28 (42)	385 ± 22 (42)
25	45	305 ± 13 (11)		398 ± 23 (10)	409 ± 12 (40)	405 ± 9 (38)
100	180	399 ± 17 (12)		426 ± 10 (24)	415 ± 12 (36)	412 ± 14 (52)
200	360	416 ± 17 (16)		423 ± 11 (28)	419 ± 11 (48)	410 ± 11 (50)

Table 16. Vickers Microhardness Measurements across the Experimental Butt Joint Weldment Illustrated in **Figure 19** (Coordinate Frame Origin at Top Left)

Hardness (HV_{200})	X Coord. (μm)	Y Coord. (μm)	Hardness (HV_{200})	X Coord. (μm)	Y Coord. (μm)	Hardness (HV_{200})	X Coord. (μm)	Y Coord. (μm)
248	0	0	254	6048	-1275	284	12614	-3027
252	500	16	350	5548	-1292	256	12114	-3044
270	1000	34	318	5049	-1310	259	11614	-3062
261	1500	52	364	4550	-1328	248	11114	-3079
280	1999	69	310	4050	-1344	256	10615	-3096
269	2498	86	318	3550	-1362	263	10115	-3114
303	2998	104	284	3050	-1380	254	9616	-3132
308	3498	122	284	2550	-1397	255	9116	-3149
252	3998	139	288	2051	-1414	246	8616	-3166
262	4498	156	273	1551	-1432	263	8116	-3184
246	4997	174	270	1052	-1450	248	7616	-3202
259	5497	191	270	552	-1467	249	7117	-3219
260	5996	208	251	52	-1484	270	6617	-3236
255	6496	226	256	70	-1979	258	6118	-3254
265	6996	244	263	569	-1962	255	5618	-3271
243	7496	261	262	1068	-1944	271	5118	-3288
246	7996	278	259	1568	-1926	274	4618	-3306
244	8495	296	277	2068	-1909	268	4118	-3324
243	8995	314	260	2568	-1892	302	3619	-3341
254	9494	331	301	3068	-1874	282	3120	-3358

259	9994	348	323	3567	-1857	308	2620	-3376
258	10494	366	309	4067	-1840	293	2120	-3394
247	10994	383	309	4566	-1822	272	1620	-3411
251	11493	400	343	5066	-1804	255	1120	-3428
257	11993	418	326	5566	-1787	260	621	-3446
245	12492	436	313	6066	-1770	243	121	-3463
253	12992	453	256	6566	-1752	256	138	-3958
265	13492	470	250	7065	-1734	249	638	-3940
246	13992	488	258	7565	-1718	240	1138	-3923
272	14492	506	257	8064	-1700	268	1638	-3906
263	14991	522	249	8564	-1682	282	2137	-3888
199	15491	540	243	9064	-1665	285	2637	-3870
257	15990	558	243	9564	-1648	289	3136	-3853
263	16490	575	260	10064	-1630	247	3636	-3836
236	16990	592	251	10563	-1612	242	4136	-3818
231	17490	610	256	11062	-1595	258	4636	-3801
229	17990	628	246	11562	-1578	242	5136	-3784
224	18489	645	255	12062	-1560	263	5635	-3766
238	18988	662	255	12562	-1543	241	6135	-3748
260	19006	168	273	13062	-1526	255	6634	-3731
247	18506	150	340	13561	-1508	247	7134	-3714
234	18006	132	314	14061	-1490	250	7634	-3696
227	17507	116	301	14560	-1473	249	8134	-3678
253	17007	98	279	15060	-1456	257	8634	-3661
290	16508	80	282	15560	-1438	249	9133	-3644
280	16008	63	291	16060	-1420	248	9632	-3626
295	15508	46	268	16560	-1403	254	10132	-3609
256	15008	28	265	17059	-1386	249	10632	-3592
272	14508	10	241	17558	-1368	252	11132	-3574
263	14009	-6	240	18058	-1351	246	11632	-3556
261	13510	-24	245	18558	-1334	241	12131	-3539
261	13010	-42	248	19058	-1316	254	12631	-3522
269	12510	-58	268	19075	-1810	234	13130	-3504
249	12010	-76	271	18576	-1828	268	13630	-3486
253	11510	-94	255	18076	-1846	260	14130	-3469
243	11011	-111	252	17576	-1863	294	14630	-3452
252	10511	-128	260	17076	-1880	275	15130	-3434

255	10012	-146	273	16576	-1898	274	15629	-3417
256	9512	-164	302	16077	-1916	284	16128	-3400
253	9012	-181	352	15577	-1933	274	16628	-3382
254	8512	-198	341	15078	-1950	265	17128	-3364
265	8012	-216	365	14578	-1968	241	17628	-3347
271	7513	-233	356	14078	-1985	238	18128	-3330
260	7014	-250	389	13578	-2002	244	18627	-3312
252	6514	-268	368	13078	-2020	236	19127	-3294
254	6014	-286	379	12579	-2038	243	19144	-3790
268	5514	-303	290	12080	-2055	283	18644	-3807
255	5014	-320	254	11580	-2072	276	18145	-3824
255	4515	-338	241	11080	-2090	237	17645	-3842
290	4015	-356	246	10580	-2108	264	17146	-3859
299	3516	-373	252	10080	-2124	273	16646	-3876
289	3016	-390	257	9581	-2142	274	16146	-3894
285	2516	-408	250	9081	-2160	329	15646	-3912
261	2016	-425	260	8582	-2177	317	15146	-3929
264	1516	-442	255	8082	-2194	333	14647	-3946
265	1017	-460	264	7582	-2212	243	14147	-3964
249	517	-478	256	7082	-2230	260	13648	-3982
235	18	-495	251	6582	-2247	253	13148	-3999
234	35	-990	252	6083	-2264	266	12648	-4016
238	534	-972	298	5584	-2282	261	12148	-4034
240	1034	-954	300	5084	-2299	264	11648	-4051
249	1534	-938	318	4584	-2316	255	11149	-4068
247	2034	-920	305	4084	-2334	259	10650	-4086
266	2534	-902	296	3584	-2352	255	10150	-4104
258	3033	-885	268	3085	-2369	258	9650	-4121
278	3532	-868	294	2585	-2386	248	9150	-4138
275	4032	-850	268	2086	-2404	256	8650	-4156
283	4532	-832	281	1586	-2422	255	8151	-4174
253	5032	-815	286	1086	-2439	253	7651	-4191
249	5532	-798	264	586	-2456	258	7152	-4208
240	6031	-780	257	86	-2474	248	6652	-4226
258	6531	-763	271	104	-2968	260	6152	-4243
267	7030	-746	278	604	-2951	265	5652	-4260
258	7530	-728	290	1104	-2934	261	5152	-4278

243	8030	-710	282	1603	-2916	262	4653	-4296
248	8530	-693	305	2102	-2898	263	4154	-4313
255	9030	-676	299	2602	-2881	263	3654	-4330
246	9529	-658	321	3102	-2864	249	3154	-4348
237	10028	-640	282	3602	-2846	279	2654	-4366
255	10528	-623	359	4102	-2829	281	2154	-4382
258	11028	-606	366	4601	-2812	293	1655	-4400
252	11528	-588	317	5101	-2794	259	1155	-4418
246	12028	-571	249	5600	-2776	268	656	-4435
263	12527	-554	238	6100	-2759	262	156	-4452
244	13027	-536	246	6600	-2742	203	173	-4947
256	13526	-518	249	7100	-2724	207	672	-4930
263	14026	-501	247	7600	-2706	-	1172	-4912
253	14526	-484	245	8099	-2689	-	1672	-4895
274	15026	-466	252	8598	-2672	-	2172	-4878
360	15526	-448	254	9098	-2654	247	2672	-4860
299	16025	-432	246	9598	-2637	259	3171	-4842
300	16524	-414	243	10098	-2620	262	3671	-4825
283	17024	-396	254	10598	-2602	249	4170	-4808
279	17524	-379	254	11097	-2584	241	4670	-4790
274	18024	-362	233	11597	-2567	255	5170	-4772
247	18524	-344	300	12096	-2550	243	5670	-4756
266	19023	-326	359	12596	-2532	249	6170	-4738
262	19040	-822	380	13096	-2514	268	6669	-4720
246	18541	-838	352	13596	-2498	258	7168	-4703
248	18041	-856	360	14096	-2480	257	7668	-4686
251	17542	-874	353	14595	-2462	243	8168	-4668
263	17042	-891	346	15095	-2445	249	8668	-4650
281	16542	-908	320	15594	-2428	248	9168	-4633
273	16042	-926	287	16094	-2410	249	9667	-4616
293	15542	-944	281	16594	-2392	238	10167	-4598
280	15043	-961	260	17094	-2375	263	10666	-4581
298	14543	-978	241	17593	-2358	253	11166	-4564
274	14044	-996	245	18093	-2340	250	11666	-4546
267	13544	-1013	248	18592	-2323	234	12166	-4528
267	13044	-1030	251	19092	-2306	281	12666	-4511
262	12544	-1048	283	19110	-2800	267	13165	-4494

267	12045	-1066	249	18610	-2818	268	13665	-4476
260	11545	-1083	252	18110	-2835	258	14164	-4458
255	11046	-1100	242	17610	-2852	267	14664	-4441
266	10546	-1118	271	17111	-2870	250	15164	-4424
259	10046	-1136	277	16611	-2888	280	15664	-4406
255	9546	-1153	286	16112	-2904	252	16164	-4389
258	9046	-1170	285	15612	-2922	266	16663	-4372
250	8547	-1188	326	15112	-2940	246	17162	-4354
244	8047	-1205	303	14612	-2957	263	17662	-4336
248	7548	-1222	313	14112	-2974	236	18162	-4319
251	7048	-1240	361	13613	-2992	239	18662	-4302
265	6548	-1258	306	13114	-3010	224	19162	-4284

Table 17. Vickers Microhardness Measurements across the Experimental Tee Joint Weldment Illustrated in **Figure 21** (Coordinate Origin in Top Left Corner)

Hardness (HV_{200})	**X Coord. (µm)**	**Y Coord. (µm)**	**Hardness (HV_{200})**	**X Coord. (µm)**	**Y Coord. (µm)**	**Hardness (HV_{200})**	**X Coord. (µm)**	**Y Coord. (µm)**
249	0	0	356	16500	-1500	252	3000	-3000
252	500	0	326	16000	-1500	254	3500	-3000
249	1000	0	336	15500	-1500	247	4000	-3000
249	1500	0	353	15000	-1500	249	4500	-3000
237	2000	0	320	14500	-1500	239	5000	-3000
236	2500	0	288	14000	-1500	247	5500	-3000
229	3000	0	256	13500	-1500	269	6000	-3000
281	3500	0	240	13000	-1500	300	6500	-3000
380	4000	0	246	12500	-1500	302	7000	-3000
226	4500	0	245	12000	-1500	302	7500	-3000
202	9000	0	243	11500	-1500	267	8000	-3000
216	9500	0	243	11000	-1500	241	8500	-3000
321	10000	0	241	10500	-1500	254	9000	-3000
267	10500	0	246	10000	-1500	257	9500	-3000
231	11000	0	275	9500	-1500	249	10000	-3000
231	11500	0	271	9000	-1500	249	10500	-3000
229	12000	0	288	8500	-1500	256	11000	-3000
232	12500	0	305	8000	-1500	255	11500	-3000
273	13000	0	334	7500	-1500	255	12000	-3000

278	13500	0
342	14000	0
201	14500	0
203	19000	0
202	19500	0
207	20000	0
368	20500	0
295	21000	0
269	21500	0
237	22000	0
214	22000	-500
239	21500	-500
268	21000	-500
328	20500	-500
359	20000	-500
350	19500	-500
387	19000	-500
329	18500	-500
214	18000	-500
209	17500	-500
223	17000	-500
204	16500	-500
219	16000	-500
333	15500	-500
386	15000	-500
353	14500	-500
301	14000	-500
272	13500	-500
259	13000	-500
236	12500	-500
236	12000	-500
241	11500	-500
235	11000	-500
265	10500	-500
280	10000	-500
340	9500	-500
347	9000	-500

361	7000	-1500
362	6500	-1500
355	6000	-1500
345	5500	-1500
306	5000	-1500
283	4500	-1500
274	4000	-1500
239	3500	-1500
237	3000	-1500
265	2500	-1500
249	2000	-1500
259	1500	-1500
265	1000	-1500
255	500	-1500
246	0	-1500
236	0	-2000
241	500	-2000
242	1000	-2000
249	1500	-2000
247	2000	-2000
253	2500	-2000
245	3000	-2000
243	3500	-2000
236	4000	-2000
277	4500	-2000
313	5000	-2000
320	5500	-2000
355	6000	-2000
328	6500	-2000
313	7000	-2000
319	7500	-2000
321	8000	-2000
310	8500	-2000
311	9000	-2000
282	9500	-2000
245	10000	-2000
248	10500	-2000

254	12500	-3000
255	13000	-3000
251	13500	-3000
249	14000	-3000
284	14500	-3000
298	15000	-3000
294	15500	-3000
298	16000	-3000
300	16500	-3000
305	17000	-3000
289	17500	-3000
299	18000	-3000
307	18500	-3000
307	19000	-3000
278	19500	-3000
246	20000	-3000
246	20500	-3000
243	21000	-3000
238	21500	-3000
236	22000	-3000
232	22000	-3500
235	21500	-3500
229	21000	-3500
236	20500	-3500
242	20000	-3500
239	19500	-3500
247	19000	-3500
248	18500	-3500
255	18000	-3500
261	17500	-3500
253	17000	-3500
263	16500	-3500
263	16000	-3500
259	15500	-3500
251	15000	-3500
232	14500	-3500
231	14000	-3500

236	8500	-500
220	8000	-500
212	7500	-500
220	7000	-500
211	6500	-500
236	6000	-500
319	5500	-500
364	5000	-500
366	4500	-500
341	4000	-500
271	3500	-500
245	3000	-500
246	2500	-500
250	2000	-500
246	1500	-500
243	1000	-500
246	500	-500
231	0	-500
242	0	-1000
236	500	-1000
232	1000	-1000
239	1500	-1000
238	2000	-1000
238	2500	-1000
238	3000	-1000
236	3500	-1000
274	4000	-1000
306	4500	-1000
346	5000	-1000
361	5500	-1000
365	6000	-1000
376	6500	-1000
372	7000	-1000
362	7500	-1000
346	8000	-1000
336	8500	-1000
294	9000	-1000

245	11000	-2000
250	11500	-2000
250	12000	-2000
240	12500	-2000
241	13000	-2000
248	13500	-2000
291	14000	-2000
286	14500	-2000
294	15000	-2000
281	15500	-2000
277	16000	-2000
317	16500	-2000
319	17000	-2000
318	17500	-2000
314	18000	-2000
288	18500	-2000
311	19000	-2000
287	19500	-2000
300	20000	-2000
262	20500	-2000
241	21000	-2000
244	21500	-2000
237	22000	-2000
248	22000	-2500
246	21500	-2500
254	21000	-2500
251	20500	-2500
281	20000	-2500
287	19500	-2500
278	19000	-2500
274	18500	-2500
293	18000	-2500
324	17500	-2500
311	17000	-2500
313	16500	-2500
292	16000	-2500
294	15500	-2500

238	13500	-3500
234	13000	-3500
241	12500	-3500
246	12000	-3500
229	11500	-3500
241	11000	-3500
236	10500	-3500
241	10000	-3500
235	9500	-3500
236	9000	-3500
238	8500	-3500
231	8000	-3500
233	7500	-3500
233	7000	-3500
228	6500	-3500
234	6000	-3500
234	5500	-3500
238	5000	-3500
244	4500	-3500
235	4000	-3500
240	3500	-3500
236	3000	-3500
236	2500	-3500
239	2000	-3500
241	1500	-3500
245	1000	-3500
259	500	-3500
254	0	-3500
251	0	-4000
244	500	-4000
250	1000	-4000
244	1500	-4000
242	2000	-4000
243	2500	-4000
236	3000	-4000
234	3500	-4000
235	4000	-4000

274	9500	-1000
270	10000	-1000
234	10500	-1000
236	11000	-1000
227	11500	-1000
240	12000	-1000
236	12500	-1000
233	13000	-1000
268	13500	-1000
284	14000	-1000
284	14500	-1000
323	15000	-1000
341	15500	-1000
326	16000	-1000
327	16500	-1000
342	17000	-1000
342	17500	-1000
368	18000	-1000
359	18500	-1000
336	19000	-1000
326	19500	-1000
288	20000	-1000
265	20500	-1000
255	21000	-1000
233	21500	-1000
241	22000	-1000
236	22000	-1500
246	21500	-1500
276	21000	-1500
263	20500	-1500
278	20000	-1500
348	19500	-1500
387	19000	-1500
407	18500	-1500
383	18000	-1500
392	17500	-1500
361	17000	-1500

274	15000	-2500
275	14500	-2500
266	14000	-2500
233	13500	-2500
247	13000	-2500
241	12500	-2500
254	12000	-2500
253	11500	-2500
256	11000	-2500
256	10500	-2500
253	10000	-2500
255	9500	-2500
262	9000	-2500
316	8500	-2500
311	8000	-2500
293	7500	-2500
302	7000	-2500
295	6500	-2500
303	6000	-2500
289	5500	-2500
282	5000	-2500
249	4500	-2500
246	4000	-2500
248	3500	-2500
255	3000	-2500
247	2500	-2500
254	2000	-2500
246	1500	-2500
257	1000	-2500
249	500	-2500
250	0	-2500
247	0	-3000
248	500	-3000
235	1000	-3000
245	1500	-3000
247	2000	-3000
250	2500	-3000

234	4500	-4000
230	5000	-4000
233	5500	-4000
226	6000	-4000
226	6500	-4000
220	7000	-4000
236	7500	-4000
233	8000	-4000
234	8500	-4000
236	9000	-4000
242	9500	-4000
233	10000	-4000
246	10500	-4000
239	11000	-4000
240	11500	-4000
241	12000	-4000
244	12500	-4000
240	13000	-4000
243	13500	-4000
240	14000	-4000
237	14500	-4000
249	15000	-4000
278	15500	-4000
293	16000	-4000
290	16500	-4000
283	17000	-4000
263	17500	-4000
283	18000	-4000
272	18500	-4000
281	19000	-4000
231	19500	-4000
236	20000	-4000
242	20500	-4000
243	21000	-4000
236	21500	-4000
240	22000	-4000
241	22302	-4466

Appendix E: Thermo-Physical Property Datasets for HY-80

Table 18. Experimentally Measured Specific Heat of HY-80

Temperature (°C)	c_p (J/g-°C)	(°C)	c_p (J/g-°C)	(°C)	c_p (J/g-°C)	(°C)	c_p (J/g-°C)
23.0	0.45	320.0	0.5585	620.0	0.779	920.0	0.6006
30.0	0.4531	330.0	0.5624	630.0	0.7998	930.0	0.5993
40.0	0.4575	340.0	0.5663	640.0	0.8126	940.0	0.6118
50.0	0.4617	350.0	0.5703	650.0	0.8249	950.0	0.6103
60.0	0.4658	360.0	0.5744	660.0	0.8411	960.0	0.6093
70.0	0.4699	370.0	0.5786	670.0	0.8639	970.0	0.6127
80.0	0.4738	380.0	0.5832	680.0	0.8754	980.0	0.6135
90.0	0.4778	390.0	0.5879	690.0	0.8969	990.0	0.6192
100.0	0.4817	400.0	0.5929	700.0	0.9205	1000.0	0.6178
110.0	0.4854	410.0	0.5981	710.0	0.9446	1010.0	0.6253
120.0	0.4889	420.0	0.6029	720.0	0.9767	1020.0	0.6354
130.0	0.4924	430.0	0.608	730.0	1.0016	1030.0	0.6271
140.0	0.496	440.0	0.6132	740.0	1.0565	1040.0	0.6176
150.0	0.4995	450.0	0.6185	750.0	1.2342	1050.0	0.6153
160.0	0.5029	460.0	0.6237	760.0	1.7596	1060.0	0.6261
170.0	0.5065	470.0	0.6298	770.0	1.7113	1070.0	0.6137
180.0	0.51	480.0	0.6366	780.0	1.394	1080.0	0.6122
190.0	0.5136	490.0	0.6442	790.0	1.1841	1090.0	0.6289
200.0	0.5172	500.0	0.6502	800.0	1.075	1100.0	0.6759
210.0	0.5207	510.0	0.6586	810.0	0.9241	1110.0	0.6931
220.0	0.5242	520.0	0.6671	820.0	0.7284	1120.0	0.7163
230.0	0.5277	530.0	0.6764	830.0	0.6291	1130.0	0.7268
240.0	0.5311	540.0	0.6825	840.0	0.6057	1140.0	0.7359
250.0	0.5345	550.0	0.6884	850.0	0.5926	1150.0	0.7429
260.0	0.5379	560.0	0.6942	860.0	0.5913	1160.0	0.7523
270.0	0.5412	570.0	0.7015	870.0	0.5902	1170.0	0.7568
280.0	0.5445	580.0	0.714	880.0	0.5953	1180.0	0.7492
290.0	0.5479	590.0	0.7262	890.0	0.5952	1190.0	0.7404
300.0	0.5514	600.0	0.7416	900.0	0.6035	1200.0	0.7508
310.0	0.5549	610.0	0.7583	910.0	0.597		

Table 19. Experimentally Measured Thermal Properties of HY-80

Temperature (°C)	Thermal Diffusivity (cm^2/sec)	Density (g/cm^3)	Thermal Conductivity (W/cm-°C)
23	0.10165	7.5717	0.34635
50	0.10085	7.5375	0.35097
100	0.09895	7.5242	0.35863
200	0.09491	7.4948	0.36790
300	0.08697	7.4623	0.35786
400	0.07821	7.4274	0.34442
500	0.06851	7.3919	0.32927
600	0.05719	7.3573	0.31204
700	0.04346	7.3244	0.29301
800	0.05724	7.3352	0.45136
900	0.06034	7.3283	0.26686
1000	0.06221	7.2798	0.27979
1100	0.0635	7.2350	0.31052
1200	0.05785	7.1966	0.31258
1300	---	7.1596	---

Appendix F: Thermo-Mechanical Properties

Table 20. Assumed Elevated Temperature Elastic Modulus for HY-80 Base Material. Note: Data are based on an assumed room temperature modulus of 210 GPa (30.5 Msi) as shown in **Figure 27**.

Temperature (°C [°F])	Fraction of Room Temperature Modulus	Elastic Modulus (GPa [Msi])
23 (73)	1.0000	210 (30.5)
100 (212)	1.0000	210 (30.5)
200 (392)	0.9000	189 (27.4)
300 (572)	0.8000	168 (24.4)
400 (752)	0.7000	147 (21.3)
500 (932)	0.6000	126 (18.3)
600 (1112)	0.3100	65 (9.4)
700 (1292)	0.1300	27 (4.0)
800 (1472)	0.0900	19 (2.7)
900 (1652)	0.0675	14 (2.1)
1000 (1832)	0.0450	9 (1.4)
1100 (2012)	0.0225	5 (0.7)
1200 (2192)	0.0000	0 (0)

Table 21. Elevated Temperature Mechanical Properties of HY-80 Base Material. Data as shown in **Figures 28-29**.

Test Temperature (°C [°F])	Yield Strength (MPa [ksi])	Tensile Strength (MPa [ksi])
22 (72)	670 (97.2)	742 (107.6)
200 (392)	575 (83.4)	709 (102.8)
400 (752)	480 (69.6)	615 (89.2)
600 (1112)	240 (34.8)	382 (55.4)
700 (1292)	108 (15.7)	192 (27.8)
800 (1472)	75 (10.9)	99 (14.4)
900 (1652)	48 (7.0)	54 (7.8)
1000 (1832)	26 (3.8)	37 (5.4)
1100 (2012)	16 (2.3)	21 (3.0)

Table 22. Yield Strength of Simulated HY-80 CGHAZs after Heating to 1350 °C (2462 °F) and Cooling at Different Rates. Note: Data as illustrated in **Figure 30**.

Temperature (°C) [°F]	Yield Strength (MPa)			
	1 °C/s Cooling	10 °C/s Cooling	25 °C/s Cooling	100 °C/s Cooling
25 [77]	649	926	1034	1096
200 [392]	566	973	1079	1052
400 [752]	454	846	879	856
600 [1112]	358	309	337	318
700 [1292]	198	132	126	118

Table 23. On-Heating Flow Behavior of HY-80 Base Material. Note: Data as shown in **Figures 32-33**.

22 °C (72 °F)		200 °C (392 °F)		400 °C (752 °F)		600 °C (1112 °F)		700 °C (1292 °F)	
$\varepsilon_{p,\,true}$	σ (MPa)	$\varepsilon_{p,\,true}$	σ (MPa)	$\varepsilon_{p,\,true}$	σ (MPa)	$\varepsilon_{p,\,true}$	σ (MPa)	$\varepsilon_{p,\,true}$	σ (MPa)
0.0000	670	**0.0000**	575	**0.0000**	480	**0.0000**	240	**0.0000**	108
0.0050	678	**0.0050**	600	**0.0050**	542	**0.0050**	290	**0.0050**	165
0.0100	685	**0.0100**	610	**0.0100**	560	**0.0100**	315	**0.0100**	178
0.0200	700	**0.0200**	630	**0.0200**	580	**0.0200**	340	**0.0200**	186
0.0300	715	**0.0300**	655	**0.0300**	600	**0.0300**	360	**0.0300**	188
0.0400	740	**0.0400**	680	**0.0400**	610	**0.0400**	375	**0.0400**	188
0.0500	760	**0.0500**	710	**0.0500**	625	**0.0500**	385	**0.0500**	188
0.1000	820	**0.1000**	780	**0.1000**	640	**0.1000**	425	**0.1000**	188
0.2000	870	**0.2000**	820	**0.2000**	640	**0.2000**	425	**0.2000**	188

800 °C (1472 °F)		900 °C (1652 °F)		1000 °C (1832 °F)		1100 °C (2012 °F)	
$\varepsilon_{p,\,true}$	σ (MPa)	$\varepsilon_{p,\,true}$	σ (MPa)	$\varepsilon_{p,\,true}$	σ (MPa)	$\varepsilon_{p,\,true}$	σ (MPa)
0.0000	75	**0.000**	48	**0.000**	26	**0.000**	16
0.0050	80	**0.005**	51	**0.005**	29	**0.005**	17
0.0100	83	**0.010**	52.5	**0.010**	30	**0.010**	17.8
0.0200	88	**0.020**	54	**0.020**	32	**0.020**	19
0.0300	91	**0.030**	55	**0.030**	33.5	**0.030**	20
0.0400	94	**0.040**	56	**0.040**	35	**0.040**	20.8
0.0500	96	**0.050**	56.5	**0.050**	36	**0.050**	21.5
0.1000	103	**0.100**	58.5	**0.100**	40	**0.100**	21.5
0.2000	112	**0.200**	63	**0.200**	40	**0.200**	21.5
		0.300	67.5	**0.300**	40	**0.300**	21.5
		0.400	67.5	**0.400**	40	**0.400**	21.5

Table 24. Flow Stress of Simulated HY-80 CGHAZs after Heating to 1350 °C (2462 °F) and Cooling at 1 °C/s (1.8 °F/s). Note: Data as illustrated in **Figure 34** and terminal values are true stress and strain at rupture.

25 °C (77 °F)		200 °C (392 °F)		400 °C (752 °F)		600 °C (1112 °F)		700 °C (1292 °F)	
$\varepsilon_{p,\,true}$	σ (MPa)	$\varepsilon_{p,\,true}$	σ (MPa)	$\varepsilon_{p,\,true}$	σ (MPa)	$\varepsilon_{p,\,true}$	σ (MPa)	$\varepsilon_{p,\,true}$	σ (MPa)
0.000	580	**0.000**	562	**0.000**	454	**0.000**	357	**0.000**	203
0.005	686	**0.005**	684	**0.005**	594	**0.005**	414	**0.005**	210
0.010	734	**0.010**	718	**0.010**	648	**0.010**	423		
0.020	794	**0.020**	758	**0.020**	705	**0.014**	425		
0.030	826	**0.030**	778	**0.030**	737				
0.040	849	**0.040**	792	**0.040**	758				
0.050	880	**0.050**	806	**0.050**	772				
0.100	932	**0.100**	849	**0.100**	803				
0.178	959	**0.170**	883	**0.118**	807				

Table 25. Flow Stress of Simulated HY-80 CGHAZs after Heating to 1350 °C (2462 °F) and Cooling at 10 °C/s (18 °F/s). Note: Data as illustrated in **Figure 35** and terminal values are true stress and strain at rupture.

25 °C (77 °F)		200 °C (392 °F)		400 °C (752 °F)		600 °C (1112 °F)		700 °C (1292 °F)	
$\varepsilon_{p,\,true}$	σ (MPa)	$\varepsilon_{p,\,true}$	σ (MPa)	$\varepsilon_{p,\,true}$	σ (MPa)	$\varepsilon_{p,\,true}$	σ (MPa)	$\varepsilon_{p,\,true}$	σ (MPa)
0.000	1039	**0.000**	1072	**0.000**	845	**0.000**	310	**0.000**	132
0.005	1185	**0.005**	1204	**0.005**	979	**0.005**	404	**0.005**	149
0.010	1254	**0.010**	1271	**0.010**	1022	**0.010**	436	**0.010**	152
0.020	1312	**0.020**	1341	**0.020**	1043	**0.015**	443	**0.016**	153
0.030	1339	**0.030**	1378	**0.022**	1046				
0.040	1352	**0.040**	1404						
0.050	1359	**0.050**	1423						
0.054	1367	**0.100**	1475						
		0.114	1477						

Table 26. Flow Stress of Simulated HY-80 CGHAZs after Heating to 1350 °C (2462 °F) and Cooling at 25 °C/s (45 °F/s). Data as illustrated in **Figure 36** and terminal values are true stress and strain at rupture.

25 °C (77 °F)		200 °C (392 °F)		400 °C (752 °F)		600 °C (1112 °F)		700 °C (1292 °F)	
$\varepsilon_{p,\,true}$	σ (MPa)	$\varepsilon_{p,\,true}$	σ (MPa)	$\varepsilon_{p,\,true}$	σ (MPa)	$\varepsilon_{p,\,true}$	σ (MPa)	$\varepsilon_{p,\,true}$	σ (MPa)
0.000	1064	**0.000**	1071	**0.000**	879	**0.000**	338	**0.000**	118
0.005	1214	**0.005**	1221	**0.005**	987	**0.005**	407	**0.005**	145
0.010	1277	**0.010**	1295	**0.010**	1029	**0.010**	430	**0.010**	153
0.020	1332	**0.020**	1373	**0.020**	1047	**0.013**	432	**0.020**	157
0.030	1357	**0.030**	1413					**0.030**	159
0.040	1369	**0.040**	1441					**0.034**	159
0.050	1375	**0.050**	1462						
0.067	1379	**0.100**	1511						
		0.116	1519						

Table 27. Flow Stress of Simulated HY-80 CGHAZs after Heating to 1350 °C (2462 °F) and Cooling at 100 °C/s (180 °F/s). Data as illustrated in **Figure 37** and terminal values are true stress and strain at rupture.

25 °C (77 °F)		200 °C (392 °F)		400 °C (752 °F)		600 °C (1112 °F)		700 °C (1292 °F)	
$\varepsilon_{p,\,true}$	σ (MPa)	$\varepsilon_{p,\,true}$	σ (MPa)	$\varepsilon_{p,\,true}$	σ (MPa)	$\varepsilon_{p,\,true}$	σ (MPa)	$\varepsilon_{p,\,true}$	σ (MPa)
0.000	1095	**0.000**	1055	**0.000**	856	**0.000**	318	**0.000**	99
0.005	1235	**0.005**	1230	**0.005**	979	**0.005**	402	**0.005**	104
0.010	1300	**0.010**	1318	**0.010**	1017	**0.010**	432	**0.010**	150
0.020	1362	**0.020**	1405	**0.020**	1035	**0.015**	438	**0.020**	154
0.030	1384	**0.030**	1448	**0.021**	1036			**0.030**	158
0.040	1395	**0.040**	1478					**0.031**	159
0.050	1401	**0.050**	1497						
0.055	1403	**0.100**	1551						
		0.124	1561						

Table 28. Engineering Fracture Strain for the Specimens Shown in **Figures 34-37**.

Temperature (°C) [°F]	Fracture Strain, $\varepsilon_{f,\,eng}$ (mm/mm)			
	1 °C/s Cooling	10 °C/s Cooling	25 °C/s Cooling	100 °C/s Cooling
25 [77]	0.287	0.198	0.238	0.214
200 [392]	0.242	0.139	0.168	0.185
400 [752]	0.305	0.224	0.210	0.226
600 [1112]	0.105	0.049	0.041	0.035
700 [1292]	0.192	0.160	0.180	0.185

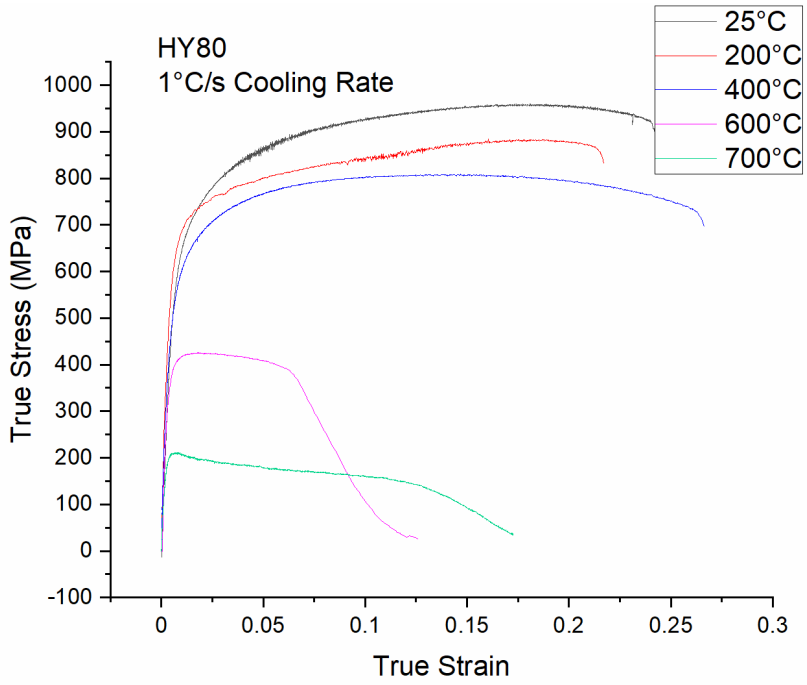

Figure 68. Uniaxial tension stress-strain curves from Gleeble tensile samples thermally cycled to a peak temperature of 1350 °C (2462 °F), cooled at 1 °C/s (1.8 °F/s), then reheated to the test temperature.

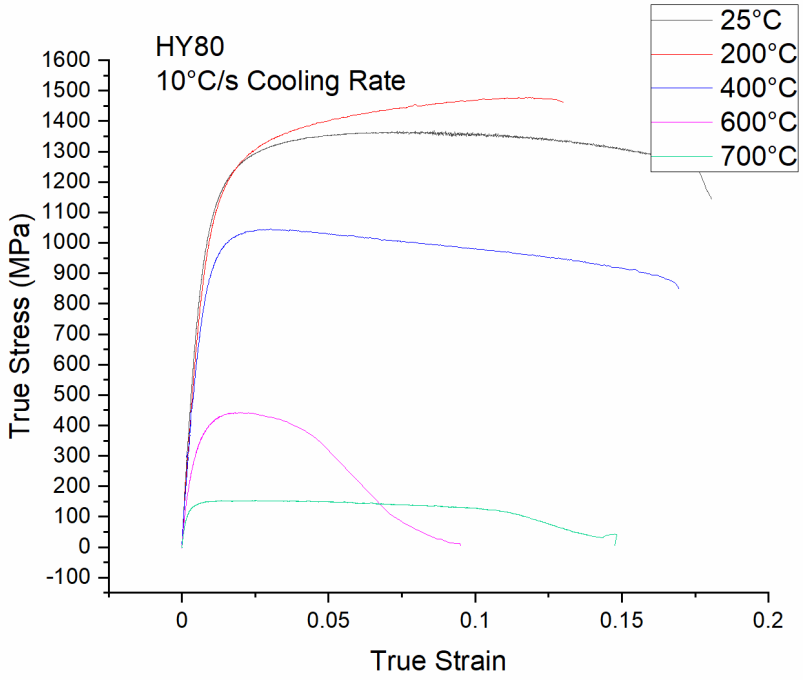

Figure 69. Uniaxial tension stress-strain curves from Gleeble tensile samples thermally cycled to a peak temperature of 1350 °C (2462 °F), cooled at 10 °C/s (18 °F/s), then reheated to the test temperature.

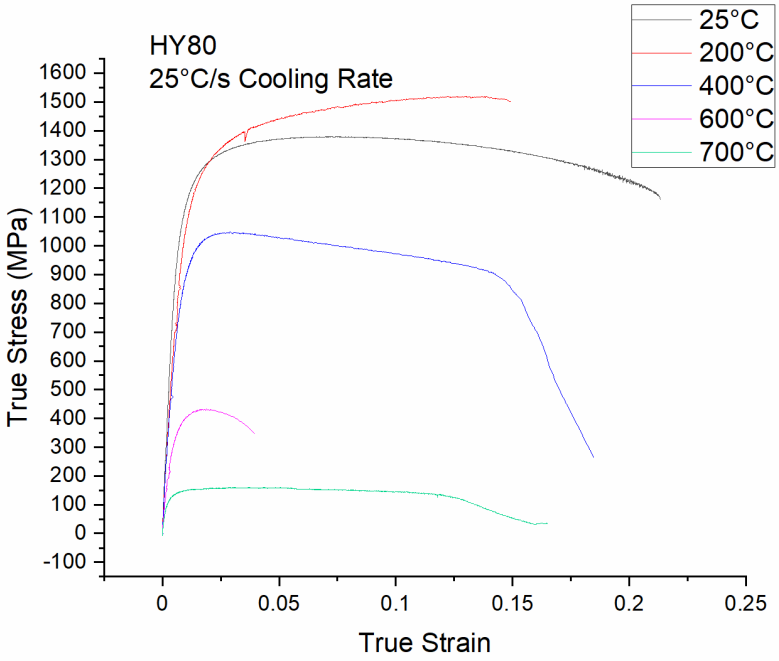

Figure 70. Uniaxial tension stress-strain curves from Gleeble tensile samples thermally cycled to a peak temperature of 1350 °C (2462 °F), cooled at 25 °C/s (45 °F/s), then reheated to the test temperature.

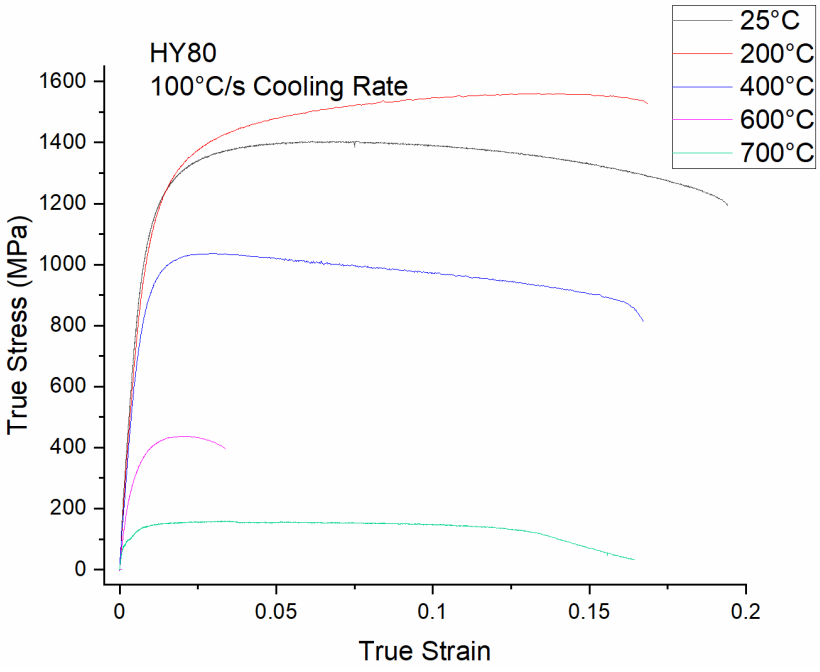

Figure 71. Uniaxial tension stress-strain curves from Gleeble tensile samples thermally cycled to a peak temperature of 1350 °C (2462 °F), cooled at 100 °C/s (180 °F/s), then reheated to the test temperature.

REFERENCES

[1] L. F. Andersen, "Residual Stresses and Deformations in Steel Structures," Doctoral Thesis, Department of Naval Architecture and Offshore Engineering, University of Denmark, 2000.

[2] MIL-S-22698C, "Military Specification: Steel Plate, Shapes, and Bars, Weldable Ordinary Strength and Higher Strength: Structural," 29 June 1988.

[3] ASTM A945/M-16, "Standard Specification for High-Strength Low-Alloy Structural Steel Plate with Low Carbon and Restricted Sulfur for Improved Weldability, Formability, and Toughness," ASTM International, West Conshohocken, PA, 2016.

[4] NAVSEA Technical Publication T9074-BD-GIB-010/0300 Rev. 2, "Base Materials for Critical Applications: Requirements for Low Alloy Steel Plate, Forgings, Castings, Shapes, Bars, and Heats of HY-80/100/130 and HSLA-80/100," 18 December 2012.

[5] D. H. Bechetti, J. K. Semple, C. R. Fisher and W. Zhang, "Temperature-Dependent Material Property Databases for Marine Steels - Part 1: DH36," NSWCCD-61-TR-2019/03, 2019.

[6] J. K. Semple, D. H. Bechetti, W. Zhang and C. R. Fisher, "Temperature-Dependent Material Property Databases for Marine Steels - Part 2: HSLA-65," NSWCCD-61-TR-2020/03, 2020.

[7] J. K. Semple, D. H. Bechetti, W. Zhang and C. R. Fisher, "Temperature-Dependent Material Property Databases for Marine Steels - Part 3: HSLA-80," NSWCCD-61-TR-2020/24, 2020.

[8] J. K. Semple, D. H. Bechetti, W. Zhang and C. R. Fisher, "Temperature-Dependent Material Property Databases for Marine Steels – Part 4: HSLA-100," NSWCCD-61-TR-2021/10, 2021.

[9] ASTM E417-17, "Standard Test Method for Analysis of Carbon and Low-Alloy Steel by Spark Atomic Emission Spectrometry," ASTM International, West Conshohocken, PA, 2017.

[10] ASTM E1019-18, "Standard Test Methods for Determination of Carbon, Sulfur, Nitrogen, and Oxygen in Steel, Iron, Nickel, and Cobalt Alloys by Various Combustion and Inert Gas Fusion Techniques," ASTM International, West Conshohocken, PA, 2018.

[11] G. R. Eisler and P. W. Fuerschbach, "SOAR: An Extensible Suite of Codes for Weld Analysis and Optimal Weld Schedules," in *Seveth International Conference on Computer Technology in Welding*, San Francisco, CA, 1997.

[12] ASTM E1461-13, "Standard Test Method for Thermal Diffusivity by the Flash Method," ASTM International, West Conshohocken, PA, 2013.

[13] ASTM E1269-11 (2018), "Standard Test Method for Determining Specific Heat Capacity by Differential Scanning Calorimetry," ASTM International, West Conshohocken, PA, 2018.

[14] ASTM A370-18, "Standard Test Methods and Definitions for Mechanical Testing of Steel Products," ASTM International, West Conshohocken, PA, 2018.

[15] ASTM E21-17, "Standard Test Methods for Elevated Temperature Tension Tests of Metallic Materials," ASTM International, West Conshohocken, PA, 2017.

[16] T. D. Huang, M. Harbison, S. Scholler, H. Rucker, J. Hu, P. Dong, M. Collette, H. Chung, M. Groden, W. Zhang, J. Semple, R. Kirchain, R. Roth, M. Bustamante, Y. Yang, R. Dull, Y. Gooroochurn, M. Doroudian, C. F. Fisher, M. Sinfield, D. Kihl and A. Gonzalez, "Robust Distortion Control Methods and Implementation for Construction of Lightweight Metallic Structures," *SNAME Transactions*, 2016.

[17] S. R. Novak, J. A. Kozub and S. T. Rolfe, "Short-Time Cryogenic and Elevated-Temperature Tensile Properties of HY-80, 5Ni-Cr-Mo-V, and 2-1/4Cr-1Mo Steels," Applied Research Laboratory - United States Steel, Monroeville, PA, 1965.

[18] E. G. Hamburg, "Physical Properties of Ultraservice Steels," Applied Research Laboratory - United States Steel, Monroeville, PA, 1971.

[19] N. Yurioka, S. Oshita and H. Tamehiro, "Determination of Necessary Preheating Temperature in Steel Welding," *Welding Journal,* vol. 52, no. 6, pp. 147-s to 153-s, 1983.

[20] T. J. Holmquist, "Strength and Fracture Characteristics of HY-80, HY-100, and HY-130 Steels Subjected to Various Strains, Strain Rates, Temperatures, and Pressures," NSWC TR 88-252, 1987.

[21] Bainite Committee of The Iron & Steel Institute of Japan, "Atlas for Bainitic Microstructures, Vol. 1: Continuous-Cooled Microstructures of Low Carbon HSLA Steels," The Iron & Steel Institute of Japan, 1992.

[22] H. K. D. H. Bhadeshia and R. W. K. Honeycombe, Steels: Microstructure and Properties, 3 ed., Oxford, UK: Butterwoth-Heinemann, 2006.

[23] A. K. Sinha, Ferrous Physical Metallurgy, Stoneham, MA: Butterworth Publishers, 1989.

[24] G. Thewlis, "Classification and Quantification of Microstructures in Steels," *Materials Science and Technology,* vol. 20, pp. 143-160, 2004.

[25] International Institute of Welding, Compendium of Weld Metal Microstructures and Properties: Submerged-arc Welds in Ferritic Steel, Cambridge, UK: Woodhead Publishing, 1985.

[26] B. L. Bramfitt and J. Speer, "A Perspective on the Morphology of Bainite," *Metallurgical Transactions A,* vol. 21A, pp. 817-829, 1990.

[27] N. Huda, Y. Ding and A. P. Gerlich, "Temper-treatment development to decompose detrimental martensite-austenite and its effect on linepipe welds," *Materials Science and Technology,* vol. 33, no. 16, pp. 1978-1992, 2017.

[28] M. Peet, "Prediction of Martensite Start Temperature," *Materials Science and Technology,* vol. 31, no. 11, pp. 1370-1375, 2014.

[29] S. Kang, S. Yoon and S.-J. Lee, "Prediction of Bainite Start Temperature in Alloy Steels with Difference Grain Sizes," *ISIJ International,* vol. 54, no. 4, pp. 997-999, 2014.

[30] C. Capdevilla, F. G. Caballero and C. Garcia de Andres, "Determination of Ms Temperature in Steels: A Bayesian Neural Network Model," *ISIJ International,* vol. 42, pp. 894-902, 2002.

[31] J. S. Kirkaldy and D. Venugopalan, "Phase Transformations in Ferrous Alloys," in *Phase Transformations in Ferrous Alloys: Proceedings of an International Conference,* Philadelphia, PA, 1984.

[32] Filing Code: SA-197, "HY-80 (Armor Plate Steel)," in *Alloy Digest*, Upper Montclair, NJ, Engineering Alloys Digest, Inc., 1966.

[33] ASTM E111-17, "Standard Test Method for Young's Modulus, Tangent Modulus, and Chord Modulus," ASTM International, West Conshohocken, PA, 2017.

[34] E. 1993-1-1, "Eurocode 3: Design of steel structures - Part 1-1: General rules and rules for buildings," 2005.

[35] E. 1993-1-2, "Eurocode 3: Design of steel structures - Part 1-2: General rules - Structural fire design," 2005.

[36] ASTM A541/M-05 (2015), "Standard Specification for Quenched and Tempered Carbon and Alloy Steel Forgings for Pressure Vessel Components," ASTM International, West Conshohocken, PA, 2015.

[37] ASTM A131/M-14, "Standard Specification for Structural Steel for Ships," ASTM International, West Conshohocken, PA, 2014.

[38] J. O. Andersson, T. Herlander, L. Hoglund, P. F. Shi and B. Sundman, "Thermo-Calc & DICTRA, Computational Tools for Materials Science," *Calphad,* vol. 26, pp. 92-101, 2002.

[39] W. S. Rasband, "ImageJ," U. S. National Institutes of Health, Bethesda, MD, USA, 1997-2018. [Online]. Available: https://imagej.nih.gov/ij/.

[40] ASTM E1382-97 (2015), "Standard Test Methods for Determining Average Grain Size Using Semiautomatic And Automatic Image Analysis," ASTM International, West Conshohocken, PA, 2015.

[41] C. Heinze, A. Pittner, M. Rethmeiri and S. S. Babu, "Dependency of Martensite Start Temperature on Prior Austenite Grain Size and Its Influence on Welding-Induced Residual Stress," *Computational Materials Science,* vol. 69, pp. 251-260, 2013.

[42] M. Shome and O. N. Mohanty, "Continuous cooling Transformation Diagrams Applicable to the Heat-Affected Zone of HSLA-80 and HSLA-100 Steels," *Metallurgical and Materials Transactions A,* vol. 37A, pp. 2159-2169, 2006.

[43] B. Taljat, B. Radhakrishnan and T. Zacharia, "Numerical Analysis of GTA Welding Process with Emphasis on Post-Solidification Phase Transformation Effects on Residual Stress," *Materials Science and Engineering A,* vol. A246, pp. 45-54, 1998.

[44] X. Yue, J. C. Lippold, B. T. Alexandrox and S. S. Babu, "Continuous Cooling Transformatoin Behavior in the CGHAZ of Naval Steels," *Welding Journal,* vol. 91, no. 3, pp. 67-s to 75-s, 2012.

[45] S.-J. Lee, J.-S. Park and Y.-K. Lee, "Effect of Austenite Grain Size on the Transformation inetics of Upper and Lower Bainite in a Low-Alloy Steel," *Scripta Materialia,* vol. 59, no. 1, pp. 87-90, 2008.

[46] P. Holsberg, "An Overview of Some Current Research on Welding Residual Stresses and Distortion in the U.S. Navy," Naval Surface Warfare Center, Carderock Division, West Bethesda, MD, 1997.

[47] R. R. Mohanty, N. Fonstein and O. Girina, "Effect of Heating Rate on the Austenite Formation in Low-Carbon High-Strength Steels Annealed in the Intercricial Region," *Metallurgical and Materials Transactiona A,* vol. 42A, no. 12, pp. 3680-3690, 2011.

[48] F. L. G. Oliveira, M. S. Andrade and A. B. Cota, "Kinetics of Austenite Formation during Continuous Heating in a Low Carbon Steel," *Materials Characterization,* vol. 58, pp. 256-261, 2007.

[49] C. A. Apple and G. Krauss, "The Effect of Heating Rate on the Martensite to Austenite Transformation in Fe-Ni-C Alloys," *Acta Materialia,* vol. 20, pp. 849-856, 1972.

[50] J. Valencia and C. Papesch, "Thermophysical Properties Characterization of HSLA-65 Rolled Plate," Concurrent Technologies Corporation, 2005.

[51] J. Valencia and C. Papesch, "Thermophysical Properties and High Temperature Tensile Properties of HSLA-65 Steel Plate," Concurrent Technologies Corporation, 2007.

[52] K. Sampath, "An Understanding of HSLA-65 Plate Steels," *Journal of Materials Engineering and Performance,* vol. 15, no. 1, pp. 32-40, 2006.

[53] A. Bhagat, S. Pabi, S. Ranganathan and O. Mohanty, "Aging Behaviour in Copper Bearing High Strength Low Alloy Steels," *ISIJ International,* vol. 44, no. 1, pp. 115-122, 2004.

[54] J. J. Valencia and C. Papesch, "Thermophysical Properties and High Temperature Tensile Properties of HSLA-100 Steel Plate," Naval Metalworking Center as operated by Concurrent Technologies Corporation, Johnstown, PA, 2007.

[55] G. Spanos, R. Fonda, R. Vandermeer and A. Matuszeski, "Microstructural Changes in HSLA-100 Steel Thermally Cycled to Simulate the Heat-Affected Zone during Welding," *Metallurgical and Materials Transactions A,* vol. 26A, pp. 3277-3293, 1995.

[56] M. Sun, Y. Xu and J. Wang, "Effect of Aging Time on Microstructure and Mechanical Properties in a Cu-Bearing Marine Engineering Steel," *Materials,* vol. 13, no. 16, pp. 1-12, 2020.

[57] S. Das, A. Ghosh, S. Chatterjee and P. Ramachandra Rao, "Evolution of microstructure in an ultra-low carbon Cu bearing HSLA forging," *Scandinavian Journal of Metallurgy,* vol. 31, pp. 272-280, 2002.

[58] J. Valencia and C. Papesch, "Apparent Specific Heat and Thermal Expansion During Heating of HSLA-80 and DH-36 Steel Plates," Concurrent Technologies Corporation, Johnstown PA, 2005.

This page intentionally left blank

DISTRIBUTION

EXTERNAL

	Copies
DEFENSE TECHNICAL INFORMATION CENTER 727 JOHN J KINGMAN ROAD SUITE 0944 FORT BELVOIR, VA 22060-6218	1
RESEARCH COMMONS NAVAL UNDERSEA WARFARE CENTER BUILDING 101 NEWPORT, RI 02841	1
COMMANDER ATTN: SEA 05P2 NAVAL SEA SYSTEMS COMMAND 1333 ISAAC HULL AVENUE S.E. WASHINGTON NAVY YARD WASHINGTON, DC 20376 ATTN: Archer, Bjornson, McGrorey, Melvin	4
ATTN: SEA 05P4 NAVAL SEA SYSTEMS COMMAND 1333 ISAAC HULL AVENUE S.E. WASHINGTON NAVY YARD WASHINGTON, DC 20376 ATTN: Rodgers	1
OFFICE OF NAVAL RESEARCH 875 N RANDOLPH ST ARLINGTON, VA 22217 ATTN: Farren, Mullins	2
LIGHTWEIGHT INNOVATIONS FOR TOMORROW (LIFT) 1400 ROSA PARKS BOULEVARD DETROIT, MI 48216 ATTN: Hawke	1
HUNTINGTON-INGALLS INDUSTRIES – INGALLS SHIPBUILDING 100 JERRY ST PE HIGHWAY PASCAGOULA, MS 39581 ATTN: Scholler, Yang	2
OHIO STATE UNIVERSITY WELDING ENGINEERING PROGRAM 1248 ARTHUR E ADAMS DR COLUMBUS, OH 43221 ATTN: Zhang	1

NSWCCD INTERNAL DISTRIBUTION

Code	Name	Copies
60		1
60	Mercier	1
60	Rivera	1
60	Hovanec	1
604	Waters	1
61	DeLoach	1
611	Davis	1
611	Bechetti	1
611	Fisher	2
611	Le	1
611	Norkett	1
611	Semple	1
611	Sinfield	1
612	Roe	1
612	Draper	1
651	Henes	1
651	Nelson	1
651	Rodriguez	1
664	Miraglia	1
664	Nahshon	1


NAVSEA
WARFARE CENTERS
Carderock